Leibniz Institute of Virology

γ-Herpesvirus Ribonucleotide Reductase R1 Proteins Form Filamentous Aggregates to Sequester Target Proteins

Dissertation

Submitted to the

Department of Chemistry

Faculty of Mathematics, Informatics and Natural Sciences

University of Hamburg

In fulfillment of the requirements for the degree of

Doctor of Philosophy (PhD)

by

Laura-Marie Luoto

born in Kotka, Finland

Hamburg, August 2025

First reviewer: Prof. Dr. Wolfram Brune
Second reviewer: Prof. Dr. Nicole Fischer

Oral defense committee
Chair: Prof. Dr. Wolfram Brune
Deputy chair: Prof. Dr. Meytal Landau
Member: Prof. Dr. Michael Kolbe

Date of oral defense: November 14, 2025

"All of old. Nothing else ever.
Ever tried. Ever failed. No matter.
Try again. Fail again. Fail better."

— Samuel Beckett, *Worstward Ho*

I. Publications and presentations

<u>Publication</u>

Parts of the study presented in this thesis were published in:

Kaposi's sarcoma-associated herpesvirus ORF61 protein sequesters APOBEC3B in filamentous aggregates

<u>Laura-Marie Luoto</u>, Enrico Caragliano, Carola Schneider, Rudolph Reimer, Wolfram Brune

Journal of Virology, June 2025

<u>Presentations</u>

The author presented parts of this study at the following meetings:

LIV Joint Scientific Retreat Hamburg, Germany May 2022	Oral presentation
15th Mini-Herpesvirus Workshop Essen, Germany September 2022	Poster presentation
The Leuven Protein Aggregation Meeting Leuven, Belgium September 2022	Poster presentation
32nd Annual Meeting of the Society for Virology (GfV) Ulm, Germany March 2023	Poster presentation
International DEEP-DV Summer School Hamburg, Germany July 2023	Oral presentation
47th Annual International Herpesvirus Workshop (IHW) Missoula, Montana, USA July 2023	Oral and poster presentation
16th Mini-Herpesvirus Workshop Hannover, Germany September 2023	Oral presentation
33rd Annual Meeting of the Society for Virology (GfV) Vienna, Austria March 2024	Oral presentation
48th Annual International Herpesvirus Workshop (IHW) Portland, Oregon, USA July 2024	Oral and poster presentation
LIV Scientific Retreat Hamburg, Germany September 2024	Poster presentation

II. Table of contents

III. List of abbreviations

3D-PCR	differential DNA denaturation PCR
3-MA	3-methyladenine
A3	APOBEC3
ACN	acetonitrile
AID	activation-induced deaminase
AIDS	acquired immunodeficiency syndrome
ALFY	autophagy-linked FYVE protein
AmpR	ampicillin resistance
APOBEC	apolipoprotein B mRNA-editing enzyme, catalytic polypeptide-like
APS	ammonium persulfate
ATG	autophagy-related
BAC	bacterial artificial chromosome
bp	base pair
BSA	bovine serum albumin
BST2	bone marrow stromal antigen 2
cDNA	complementary DNA
CLEM	correlative light and electron microscopy
cLSM	confocal laser scanning microscopy
CMA	chaperone-mediated autophagy
CPE	cytopathic effect
ctd	C-terminal domain
DDA	data-dependent acquisition
DL	detection limit
DMEM	Dulbecco's Modified Eagle Medium
DMSO	dimethyl sulfoxide
DNA	deoxyribonucleic acid
dNTP	deoxyribonucleoside triphosphate
doxy	doxycycline
dpi	days post-infection
dsDNA	double-stranded DNA
E	early
EBV	Epstein-Barr virus
ECL	enhanced chemiluminescence
eGFP	enhanced green fluorescent protein
EM	electron microscopy
ER	endoplasmic reticulum
FA	formic acid
FBS	fetal bovine serum
FDR	false discovery rate
F-MuLV	Friend murine leukemia virus
FRAP	fluorescence recovery after photobleaching
g	gravitational force
GAPDH	glyceraldehyde 3-phosphate dehydrogenase
HA	hemagglutinin
HCMV	human cytomegalovirus

HEK	human embryonic kidney (cells)
HFF	human foreskin fibroblast
HIV	human immunodeficiency virus
HLS	helical loop structure
hpi	hours post-infection
hpt	hours post-transfection
HRP	horseradish peroxidase
Hsc70	heat shock cognate protein 70
HSV-1	herpes simplex virus type 1
HVS	herpesvirus saimiri
HygroR	hygromycin resistance
ICP	infected cell protein
IE	immediate-early
IF	immunofluorescence
IFN-β	interferon-β
IP	immunoprecipitation
IPAM	Induced Protein Aggregation Motif
KanR	kanamycin resistance
kb	kilobase
kDa	kilodalton
KS	Kaposi's sarcoma
KSHV	Kaposi's sarcoma-associated herpesvirus
L	late
LAMP-2A	lysosome-associated membrane protein 2A
LANA	latency-associated nuclear antigen
LB	lysogeny broth
LC3	microtubule-associated protein 1 light chain 3
LC-MS/MS	liquid chromatography-tandem mass spectrometry
LUR	long unique region
mA3	murine APOBEC3
MAGOH	Protein mago nashi homolog
MCD	multicentric Castleman's disease
MCMV	murine cytomegalovirus
MEF	mouse embryonic fibroblast
MHV-68	murine gammaherpesvirus 68
MMTV	mouse mammary tumor virus
MOI	multiplicity of infection
NA	numerical aperture
NBR1	neighbor of BRCA1 gene 1
NEMO	NF-κB essential modulator
NF-κB	nuclear factor kappaB
NSs	non-structural small (protein)
nt	nucleotide
OD	optical density
ORF	open reading frame
PAGE	polyacrylamide gel electrophoresis
PAS	Protein A Sepharose

PBS	phosphate-buffered saline
PCR	polymerase chain reaction
PE	phosphatidylethanolamine
PEI	polyethylenimine
PEL	primary effusion lymphoma
PFA	paraformaldehyde
PGK	phosphoglycerate kinase
PRV	pseudorabies virus
PuroR	puromycin resistance
R1	ribonucleotide reductase large subunit
R2	ribonucleotide reductase small subunit
RBM8A	RNA-binding protein 8A
RC	replication compartment
RFI	relative fluorescence intensity
RFLP	restriction fragment length pattern
RHIM	RIP Homotypic Interaction Motif
RIPA	radio immunoprecipitation assay
RIPK1	receptor-interacting protein kinase 1
RNA	ribonucleic acid
RNF213	RING finger protein 213
RNR	ribonucleotide reductase
rpm	revolutions per minute
RT	room temperature
RTA	replication and transcription activator
RVFV	Rift Valley fever virus
SDS	sodium dodecyl sulfate
SEM	standard error of the mean
SHI	short helix insertion
SQSTM1	sequestosome 1
ssDNA	single-stranded DNA
TAE	Tris-acetate-EDTA
TAX1BP1	Tax1-binding protein 1
TBE	Tris-borate-EDTA
TBS-T	Tris-buffered saline with Tween 20
TCID	tissue culture infectious dose
TEM	transmission electron microscopy
Tet	tetracycline
TIME	telomerase-immortalized microvascular endothelial (cells)
T_m	melting temperature
TRE	tetracycline-responsive element
UPS	ubiquitin-proteasome system
Vif	virion infectivity factor
VZV	varicella zoster virus
WB	Western blot
ZC3H14	Zinc finger CCCH domain-containing protein 14
ZeoR	Zeocin resistance

1. Zusammenfassung

Die großen dsDNA-Genome der Herpesviren enthalten bis zu 200 offene Leserahmen (ORFs), die eine Vielzahl von Proteinen codieren, von denen viele homolog zu zellulären Enzymen sind. Die virale Ribonukleotidreduktase (RNR) ist normalerweise an der Synthese von Desoxyribonukleosidtriphosphaten (dNTPs) beteiligt, aber mehrere Herpesviren haben die katalytische große Untereinheit (R1) der RNR umfunktioniert, um der Immunantwort des Wirts entgegenzuwirken.

Das Maus-Cytomegalovirus (MCMV), ein murines β-Herpesvirus, verwendet sein R1-Protein M45, um Immunmediatoren des Wirts in zytoplasmatischen punktförmigen Aggregaten zu sequestrieren, die anschließend durch selektive Autophagie abgebaut werden. Dieser Mechanismus erfordert ein konserviertes C-terminales *Induced Protein Aggregation Motif* (IPAM), das in R1-Proteinen aller Herpesvirus-Unterfamilien vorkommt. Eine ähnliche Strategie wird vom humanen α-Herpesvirus Herpes-simplex-Virus Typ 1 (HSV-1) zur Umgehung der Immunabwehr eingesetzt. In der γ-Herpesvirus-Unterfamilie verwendet das Epstein-Barr-Virus (EBV) sein R1-Protein, um die zelluläre mutationserzeugende Cytosin-Desaminase APOBEC3B (A3B) zu binden und aus dem Zellkern ins Zytoplasma zu verlagern. Ob die R1-abhängige A3B-Umverteilung ein konserviertes Merkmal der γ-Herpesvirus-Infektion darstellt und eine IPAM-abhängige Aggregation beinhaltet, wurde bisher nicht erforscht.

Die vorliegende Studie hatte zum Ziel, das R1-Protein ORF61 des humanpathogenen γ-Herpesvirus Kaposi-Sarkom-assoziierten Herpesvirus (KSHV) und des verwandten murinen Gammaherpesvirus 68 (MHV-68) zu untersuchen. Beide Proteine bilden Aggregate, wie durch eine *fluorescence recovery after photobleaching* (FRAP) Analyse von fluoreszenzmarkierten R1-Fusionsproteinen nachgewiesen wurde. Anders als die äquivalenten Proteine bei α- und β-Herpesviren wurden ORF61-Aggregate nicht in nennenswertem Maße durch Autophagie abgebaut. Eine weiterführende strukturelle Charakterisierung mittels korrelativer Licht- und Elektronenmikroskopie (CLEM) zeigte, dass die ORF61-Aggregate in infizierten Zellen aus Filamentbündeln bestanden, im Gegensatz zu den eher globulären Aggregaten, die für ihr MCMV-Homolog charakteristisch sind. Während der lytischen KSHV-Infektion verlagerte das ORF61-Protein den nukleären A3B auf IPAM-abhängige Weise in zytoplasmatische Aggregate, um das replizierende virale Genom zu schützen. Eine KSHV IPAM-Mutante, die A3B nicht umverteilen konnte, zeigte eine erhöhte A3B-vermittelte Deaminierung des Genoms sowie verminderte Virustiter im Vergleich zum Ursprungsvirus. Im Gegensatz dazu sequestrierte MHV-68 ORF61 weder menschliche noch murine APOBEC3-Proteine, was darauf hindeutet, dass es auf andere Interaktionspartner abzielt. In ihrer Gesamtheit zeigen die Ergebnisse, dass die R1-Proteine von KSHV und MHV-68 filamentöse, IPAM-abhängige Aggregate in infizierten Zellen bilden, um zelluläre Zielproteine wie APOBEC3B zu binden und zu neutralisieren.

2. Abstract

The large dsDNA genomes of herpesviruses contain up to 200 open reading frames (ORFs) that encode a vast array of proteins, many of which are homologous to cellular enzymes. The viral ribonucleotide reductase (RNR) normally plays a role in deoxyribonucleoside triphosphate (dNTP) synthesis, but several herpesviruses have repurposed the RNR catalytic large subunit (R1) to counteract the host immune response.

Murine cytomegalovirus (MCMV), a mouse β-herpesvirus, uses its R1 protein M45 to sequester host immune mediators in cytoplasmic dot-like aggregates that are subsequently degraded via selective autophagy. This mechanism relies on a conserved C-terminal Induced Protein Aggregation Motif (IPAM) that is found in R1 proteins across all herpesvirus subfamilies. A similar strategy is employed by the human α-herpesvirus herpes simplex virus type 1 (HSV-1) to evade host immunity. In the γ-herpesvirus subfamily, Epstein-Barr virus (EBV) utilizes its R1 protein to bind and relocalize the cellular mutagenic cytosine deaminase APOBEC3B (A3B) from the nucleus to the cytoplasm. However, whether R1-dependent A3B targeting is a conserved feature in γ-herpesvirus infection, and whether it involves IPAM-dependent aggregation, remains unexplored.

The present study aimed to investigate the R1 protein ORF61 of the human γ-herpesvirus Kaposi's sarcoma-associated herpesvirus (KSHV) and the related murine gammaherpesvirus 68 (MHV-68). Both proteins form aggregates, as shown by fluorescence recovery after photobleaching (FRAP) of fluorescently labeled R1 fusion proteins. Unlike their α- and β-herpesvirus counterparts, ORF61 aggregates were not substantially degraded by autophagy. Further structural characterization by correlative light and electron microscopy (CLEM) revealed that the ORF61 aggregates in infected cells were composed of filament bundles, in contrast to the more globular aggregates characteristic of their MCMV homolog. During lytic KSHV infection, the ORF61 protein relocalized nuclear A3B to cytoplasmic aggregates in an IPAM-dependent manner to protect the replicating viral genome. An IPAM mutant KSHV, that failed to redistribute A3B, displayed increased A3B-mediated genome deamination and reduced viral titers compared to the parental virus. In contrast, MHV-68 ORF61 did not sequester human or mouse APOBEC3 proteins, suggesting that it engages different targets. Taken together, the results show that KSHV and MHV-68 R1 proteins form filamentous, IPAM-dependent aggregates in infected cells to sequester and neutralize cellular targets proteins, such as APOBEC3B.

3. Introduction

3.1 Common characteristics of herpesviruses

Herpesviruses (*Orthoherpesviridae*) are ubiquitous pathogens that infect diverse mammalian, avian and reptilian species, to which they are intricately adapted as a result of extensive host-pathogen co-evolution. Of the more than 100 herpesviruses described to date, nine are human pathogenic. While herpesvirus infections are typically mild or asymptomatic, they can lead to severe and life-threatening disease in immunocompromised individuals, such as newborns, the elderly, and organ transplant recipients.

The *Orthoherpesviridae* family is further divided into three subfamilies: *Alpha-*, *Beta-* and *Gammaherpesvirinae*, that differ from each other in terms of genome organization, host range and tissue tropism. The human pathogenic members of the subfamilies include the α-herpesviruses herpes simplex virus type 1 and 2 (HSV-1 and -2) and varicella zoster virus (VZV), the β-herpesviruses human cytomegalovirus (HCMV), human herpesviruses 6A, 6B and 7, as well as the γ-herpesviruses Epstein-Barr virus (EBV) and Kaposi's sarcoma-associated herpesvirus (KSHV) (1, 2).

3.1.1 Herpesvirus particle

The key features common to all herpesviruses are their virion structure and biphasic replication cycle. A single copy of their large, linear double-stranded DNA (dsDNA) genome is surrounded by a nucleocapsid of icosahedral symmetry. The capsid is covered by the tegument, an amorphous protein layer, which is in turn enclosed by a host membrane-derived lipid bilayer envelope with protruding virus-encoded membrane glycoproteins (1) (Fig. 1).
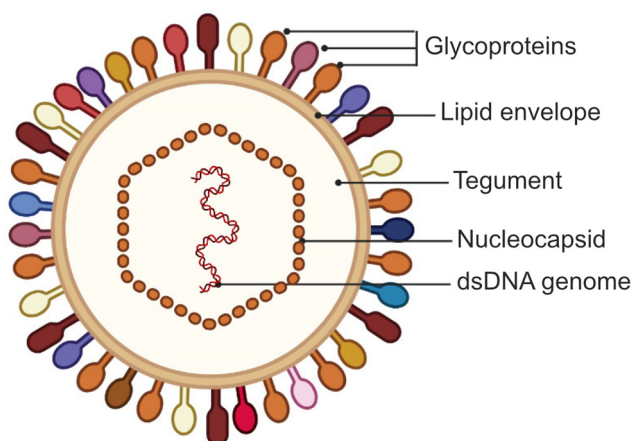
Figure 1. Schematic representation of the herpesvirus virion highlighting the key structural elements. The linear dsDNA genome is surrounded by an icosahedral nucleocapsid, which is in turn enclosed by a proteinaceous tegument layer. A lipid bilayer envelope with embedded membrane glycoproteins constitutes the outermost part of the particle. Adapted from Zheng *et al.*, Viruses, 2022 (3).

3.1.2 Herpesvirus replication cycle

Viral glycoproteins first mediate virion attachment to the host cell membrane via interaction with surface proteoglycans, after which they bind to cellular receptors to facilitate particle entry by membrane fusion. Upon cell entry, the released capsid is transported to the nucleus where it deposits the viral genome. Viral genes are then transcribed in a temporally regulated cascade. First, immediate-early (IE) genes produce regulatory proteins that in turn initiate the transcription of early (E) genes required for viral DNA replication. Viral DNA replicates in the nucleus by a rolling-circle mechanism followed by transcription of late (L) genes mainly encoding virion components, such as capsid and tegument proteins. Capsids containing the newly replicated viral DNA assemble in the nucleus and acquire the tegument and envelope when exiting the nucleus and passing through the endoplasmic reticulum (ER) and Golgi apparatus before being released from the cell in exocytic vesicles that fuse with the host cell membrane (4) (Fig. 2).
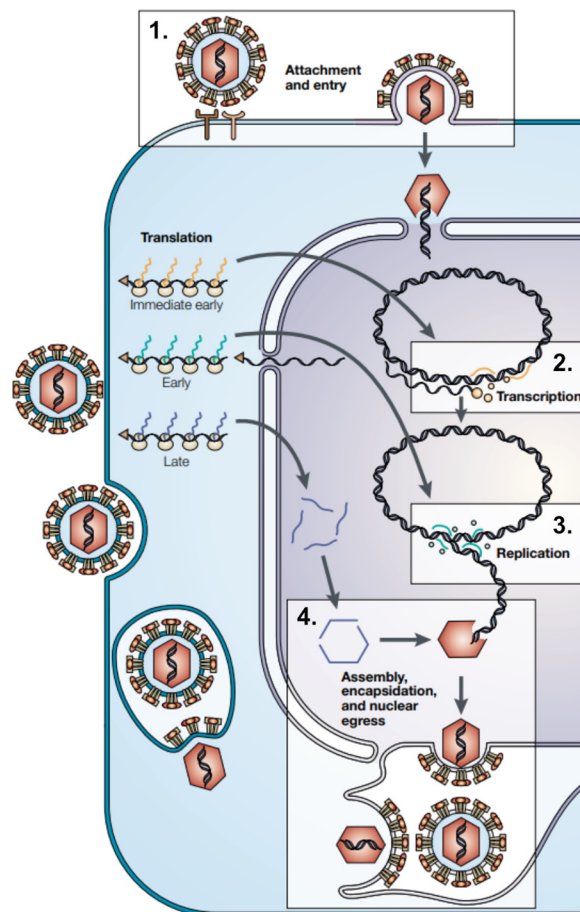
Figure 2. Simplified view of the herpesviral replication cycle. 1. Viral membrane glycoproteins mediate particle attachment and binding to cellular surface receptors. Upon particle entry by membrane fusion, the capsid is delivered to the nucleus and the linear dsDNA genome injected through the nuclear pore. 2. In the nucleus, the viral genome circularizes, and the temporally regulated viral transcription cascade commences with the transcription of immediate-early (IE) genes (yellow). 3. IE gene products initiate the transcription of early (E) genes (green) required for viral DNA replication. The viral DNA replicates by a rolling-circle mechanism followed by late (L) gene transcription. 4. L proteins (blue) serve as structural components of the assembling viral particles. In the nucleus, the newly replicated viral genome is enclosed by the capsid, after which the nucleocapsid buds into the perinuclear space. The new particle acquires its lipid envelope by passing through the nuclear, ER and Golgi membranes. Finally, the mature virion is released from the cell by exocytosis. Adapted from Coen & Schaffer, Nat Rev Drug Discov., 2003 (5).

This productive stage of the herpesviral replication cycle, known as the lytic cycle, is characterized by genome-wide viral gene transcription and production of infectious progeny causing rupture of the infected cell. In addition to lytic replication, all herpesviruses share the ability to establish latency in the infected host. This non-productive phase of the replication cycle allows the virus to evade immune recognition, since only a limited number of viral genes are expressed, and no viral particles are produced. Some herpesviruses integrate into the host genome for latent replication, whereas most persist as extrachromosomal circular episomes that are replicated by the cellular machinery and passed to the daughter cells during cell division. The ability to enter latency allows herpesviruses to establish lifelong infections in varying host tissues specific to each virus. Certain stimuli, such as changes in the cellular microenvironment or in the host's immune status, can cause the latent virus to reactivate and to re-enter the lytic cycle, facilitating viral spread within the infected host as well as transmission to a new host (2).

3.2 γ-Herpesviruses

Members of the γ-herpesvirus subfamily (*Gammaherpesvirinae*) are characterized by their lymphotropism, i.e., their ability to establish infection and persist in lymphocytes, their narrow host range, which is often restricted to only a few related species, as well as their capacity to induce lymphoproliferation and tumorigenesis. The subfamily includes two human pathogenic viruses (6). Epstein-Barr virus (EBV), which belongs to the genus *Lymphocryptovirus*, was the first γ-herpesvirus and the first human tumor virus to be discovered. With a global seroprevalence of approximately 95%, it is one of the most prevalent human viruses (7). EBV is primarily transmitted through saliva. The virus establishes primary infection in epithelial cells of the oropharynx, from where it spreads to infect circulating B cells. Although often asymptomatic in young children, primary infection during adolescence can lead to infectious mononucleosis, characterized by fever, pharyngitis, lymphadenopathy, and fatigue (8). EBV persists in a latent state within memory B cells (9), and chronic EBV infection is linked to various human malignancies, including the B cell lymphomas Burkitt's lymphoma (10) and Hodgkin lymphoma (11), and the epithelial tumors nasopharyngeal carcinoma (10) and gastric carcinoma (12).

3.2.1 Kaposi's sarcoma-associated herpesvirus (KSHV)

Kaposi's sarcoma-associated herpesvirus (KSHV), also known as human herpesvirus 8, is the other human pathogenic representative of the γ-herpesvirus subfamily and a member of the genus *Rhadinovirus*. Similar to the related EBV, KSHV is an oncogenic virus, a property that among human herpesviruses is unique to the γ-subfamily. KSHV is associated with three human malignancies: Kaposi's sarcoma (KS) (13), primary effusion lymphoma (PEL) (14) and a type of multicentric Castleman's disease (MCD) (15). KS is an endothelial lymphatic neoplasm typically forming

cutaneous lesions on the trunk and the extremities, whereas PEL and MCD are of B cell origin. All these KSHV-associated malignancies are usually observed in an immunocompromised setting, e.g., human immunodeficiency virus (HIV)-infection, with KS being considered an acquired immunodeficiency syndrome (AIDS)-defining condition in HIV-positive individuals (16).

KSHV was discovered in 1994 by Chang and Moore who detected novel herpesviral DNA sequences in KS lesion biopsies using PCR-based representational difference analysis (13). The KSHV genome consists of a 140 kb long unique coding region (LUR) flanked by 35-45 copies of 0.8 kb GC-rich tandem repeat sequences at both termini (17, 18). The LUR contains at least 89 open reading frames (ORFs) that are numbered according to their positional homologs conserved in herpesvirus saimiri (HVS), a prototype rhadinovirus infecting squirrel monkeys. The ORFs termed K1 to K15 do not share any apparent amino acid homology with HVS genes (6, 18).

In contrast to the ubiquitously present EBV, KSHV seroprevalence exhibits marked geographic variation. In high-level endemic areas, such as Central and Eastern Africa, seroprevalence rates exceeding 50% among general adult population are reported, whereas in Europe, North America and other non-endemic areas only 1-6% of the population is KSHV-positive (19). The virus is mainly shed in saliva (20) and transmitted in close contact between family members in endemic areas and through sexual contact in non-endemic areas.

In patient samples KSHV has been detected in endothelial and epithelial cells, B cells, and monocytes (21-23). In contrast to α- and β-herpesviruses, the default mode of KSHV replication is latency, during which the viral latency-associated nuclear antigen (LANA) tethers the viral episome to the host chromosome at the terminal repeat region, thereby ensuring equal distribution of episomes to the daughter cells upon DNA replication (24, 25). Various environmental stimuli can reactivate KSHV from latency by inducing expression of the viral replication and transcription activator (RTA), the major lytic switch protein encoded by ORF50 (26). In cell culture, KSHV lytic replication can be chemically induced by applying sodium butyrate or phorbol ester treatment (27, 28).

3.2.2 Murine gammaherpesvirus 68 (MHV-68)

As the limited host range of human γ-herpesviruses precludes experimental animal studies, infection of laboratory mice with murine gammaherpesvirus 68 (MHV-68) is used instead to model γ-herpesvirus pathogenesis and the host immune response to infection. MHV-68 is a rodent rhadinovirus that was first isolated from the bank vole (*Clethrionomys glareolus*) in Slovakia in 1980 (29, 30). The viral genome contains a 118 kb unique coding region flanked by variable numbers of 1.23 kb GC-rich tandem repeats, and it encodes approximately 80 proteins, most of which have homologous counterparts in KSHV and other rhadinoviruses (31, 32).

In the wild, MHV-68 infection is thought to occur intranasally. In contrast to the related KSHV that establishes latency by default, MHV-68 first enters the lytic replication cycle mainly targeting alveolar epithelial cells of the lung. The acute lung infection resolves within 10-12 days and is

followed by a lifelong persistent infection with B cells being the main latent reservoir of the virus (33, 34). At two weeks post-infection, B and T cell expansion in the spleen results in splenomegaly (35), and an infectious mononucleosis-like syndrome, reminiscent of that caused by EBV, is observed. In the long term, approx. 10% of persistently infected mice develop a lymphoproliferative disease with the incidence increasing to 60% following immunosuppressive treatment (36), thus reflecting some aspects of KSHV and EBV pathology in humans.

In contrast to the human γ-herpesviruses, the host range of MHV-68 is less restricted *in vitro*, and the virus is capable of productively infecting epithelial and fibroblast cell lines originating from several mammalian species, including humans and other primates (37).

3.3 Protein aggregation and degradation

Protein aggregation is a common cellular occurrence often resulting from protein misfolding due to mutations, perturbed translation, defective protein assembly, or cellular stress caused by, for instance, a viral infection. Misfolding exposes aggregation-prone hydrophobic surfaces of the protein that are usually buried within the tertiary structure. Since aggregation has the potential to impair normal protein function, cellular protein quality control machinery is responsible for preventing aggregation and disposing of already formed aggregates. Molecular chaperones, such as heat shock proteins, prevent aggregation by repairing misfolded proteins and assisting in proper folding (38). Damaged proteins that are beyond chaperone-mediated repair are targeted for degradation either by the proteasome or by the lysosome via autophagy (Fig. 3).

3.3.1 Degradation of soluble proteins

Degradation by the ubiquitin-proteasome system (UPS) requires substrate ubiquitination, a three-step enzymatic process mediated by a ubiquitin-activating E1 enzyme, a ubiquitin-conjugating E2 enzyme and an E3 ubiquitin ligase resulting in a covalent linkage of ubiquitin to a lysine residue (K) either on the target or on ubiquitin itself to form a polyubiquitin chain (39). The canonical signal for degradation by the 26S proteasome is K48-linked polyubiquitin (40) that is first recognized by the proteasomal 19S regulatory particle. The substrate is then deubiquitinated and finally degraded by the 20S catalytic core of the proteasome. Due to the narrow central channel of the 20S catalytic core, the UPS can only degrade soluble, monomeric peptides and polypeptides (41).

Monomeric protein substrates can also be degraded by chaperone-mediated autophagy (CMA). To initiate CMA, heat shock cognate protein 70 (Hsc70) recognizes the misfolded, cytosolic substrate containing a KFERQ-like motif and delivers it to the lysosome-associated membrane protein 2A (LAMP-2A) (42, 43). The LAMP-2A receptor then multimerizes and forms a translocation complex allowing the substrate to enter the lysosomal lumen, where it is eventually degraded. Oxidative stress conditions increase LAMP-2A expression, thereby inducing CMA activity that is proportional to the LAMP-2A levels on the lysosomal membrane (43, 44).

3.3.2 Degradation of protein aggregates

Protein aggregates, bacteria, damaged organelles, and other intracellular inclusions that are too large to be processed by UPS or CMA, are degraded by selective autophagy. Selective autophagy substrates are often marked by K63-linked polyubiquitin and tend to assemble into larger aggregates (45). They attract p62/sequestosome 1 (SQSTM1), neighbor of BRCA1 gene 1 (NBR1), and other autophagy receptors that bind the ubiquitinated cargo. Together with adaptor proteins, such as autophagy-linked FYVE protein (ALFY), the receptors recruit the cargo to the forming crescent-shaped isolation membrane, known as the phagophore (46, 47). Phagophore elongation requires ubiquitin-like conjugation reactions mediated by gene products of autophagy-related (*Atg*) genes. ATG12 first conjugates to ATG5 to form an oligomeric ATG5-ATG12-ATG16L complex (48, 49), which in turn conjugates ATG8 protein homologs, such as microtubule-associated protein 1 light chain 3 (LC3), to the lipid phosphatidylethanolamine (PE) present on the inner phagophore membrane (50, 51). Lipidated ATG8 proteins are involved in membrane biogenesis that closes the phagophore membrane to form a double-membrane vesicle, the autophagosome (51, 52). The autophagosome then fuses with a lysosome or a late endosome to form an autophagolysosome, in which both the ubiquitinated cargo and the cargo receptors are degraded by intracellular acid hydrolases. The resulting macromolecules are released back to the cytosol for recycling (53).
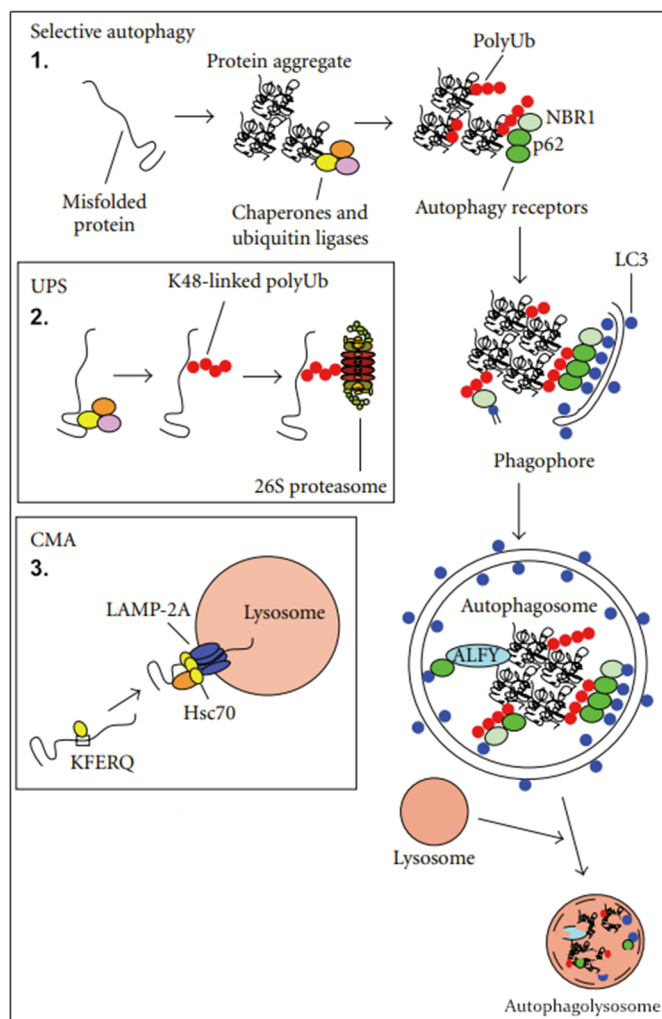
Figure 3. Schematic overview of cellular protein degradation pathways. Misfolded proteins recognized by chaperones can be degraded by selective autophagy, the ubiquitin-proteasome system (UPS), or chaperone-mediated autophagy (CMA). 1. In selective autophagy, ubiquitinated protein aggregates attract p62, NBR1, and other autophagy receptors. Together with adaptor proteins such as ALFY, the receptors recruit the cargo to the nascent phagophore via interaction with LC3 on the phagophore membrane. The phagophore membrane closes to form a double-membrane autophagosome that subsequently fuses with a lysosome. The sequestered material is degraded by acid hydrolases within the resulting autophagolysosome. 2. In the UPS, the 26S proteasome, composed of a 20S catalytic core and a 19S regulatory particle, degrades soluble protein substrates marked by K48-linked polyubiquitin. 3. In CMA, misfolded soluble proteins containing a KFERQ-like motif are recognized by Hsc70 and delivered to the lysosomal lumen for degradation via the LAMP-2A receptor. Adapted from Lamark & Johansen, Int J Cell Biol., 2012 (54).

3.4 APOBEC family of cellular cytosine deaminases

Apolipoprotein B mRNA-editing enzyme, catalytic polypeptide-like (APOBEC) protein family comprises the cellular RNA- and/or DNA-editing cytosine deaminases APOBEC1-4 and activation-induced deaminase (AID). APOBEC proteins share a conserved cytosine deaminase fold, in which the zinc-coordinating active site is surrounded by three loops (L1, L3, and L7) of varying size and amino acid composition. The loop residues mediate substrate binding and consequently influence catalytic rate and target sequence preference of the APOBEC proteins (55, 56).

The first APOBEC family member to be characterized was the name-giving APOBEC1 (A1), a mammalian RNA-editing enzyme that edits apolipoprotein B pre-mRNA in the small intestine by deaminating a cytosine (C) base at position 6666 to uracil (U), thereby producing a truncated protein required for lipid metabolism (57, 58).

AID, that is considered one of the ancestral members of the APOBEC family due to its conservation in jawed vertebrates (59), is expressed in germinal center B cells where it is responsible for antibody diversification by deaminating cytosine residues in the DNA of the immunoglobulin locus to facilitate somatic hypermutation, gene conversion, and class-switch recombination (60, 61).

The less studied members of the APOBEC family are APOBEC2 (A2) (62) and APOBEC4 (A4) (63). The *A2* gene is expressed in skeletal and cardiac muscle tissue of jawed vertebrates (64) and displays *in vitro* RNA deamination activity (62), but does not act on a DNA substrate (65). Instead, A2 was recently shown to act as a transcriptional regulator of muscle cell development and differentiation by mediating epigenetic control of cell fate (66). The *A4* gene was identified based on sequence similarity to the APOBEC family (63), but despite containing a predicted deaminase domain, the absence of conserved key residues surrounding the catalytic site suggests that the gene product is most likely devoid of deaminase activity (67). In contrast to the other APOBEC family members that are restricted to vertebrates, genomic analyses have identified *A4* orthologs also in aquatic invertebrates and in some algal lineages, suggesting an early emergence of the *A4* gene during metazoan evolution (68).

3.4.1 The APOBEC3 subfamily

The *APOBEC3* (*A3*) genes originate from diversification events in the ancestral *A3* locus in placental mammals. The expanded *A3* locus contains a varying number of genes organized in a tandem array between two vertebrate-conserved flanking genes, resulting in a varying number of corresponding A3 gene products in different mammalian species (59, 69). A3 proteins are innate immune effectors that induce C-to-U deamination in a single-stranded DNA (ssDNA) substrate resulting in guanine (G) to adenine (A) mutations on the complementary strand (70). Similar to other catalytically active members of the APOBEC family, A3 proteins deaminate their substrate by a zinc-dependent hydrolytic mechanism (58, 69, 71), but differ in their target dinucleotide sequence preferences (72), tissue-specific expression patterns (64, 73), as well as subcellular localization (74-76). In humans and other Old World anthropoids there are seven A3 proteins (A3A to –D and A3F to –H) (59, 69, 73) which display a steady-state nuclear, cytoplasmic or cell-wide localization (77, 78). In contrast, sheep and cattle encode four A3 proteins that are present either cell-wide or in the cytoplasm (79), whereas rodents only have a single cytoplasmic A3 protein (59, 69).

3.4.2 APOBEC3 proteins as viral restriction factors

Due to their mutagenic potential, human A3 proteins function as restriction factors for several viruses with ssDNA replication intermediates. The first A3 family member this property was ascribed to was APOBEC3G (A3G), a restriction factor for HIV-1. A3G is packaged into HIV-1 viral particles where it induces C-to-U deamination in the reverse-transcribed viral cDNA that in turn results either in the degradation of viral cDNA prior to integration or in the production of defective viral proteins (70, 80). Reciprocally, HIV-1 has evolved to overcome A3G-mediated restriction by using its virion infectivity factor (Vif) protein to exclude A3G from nascent virions and to target it for degradation via the ubiquitin-proteasome pathway (81, 82). Subsequently, it was discovered that APOBEC3D, -3F and -3H similarly interfere with HIV-1 replication and are counteracted by the viral Vif protein (83-85). Besides HIV-1, human A3 proteins have been shown to target a number of different DNA-based viruses, such as hepatitis B virus (86-88), parvoviruses (89, 90), papillomaviruses (91), and polyomaviruses (92), as well as endogenous transposable elements (77, 93), by either deamination-dependent or –independent mechanisms.

The antiviral functions of A3 proteins are not restricted to humans, as illustrated by the sole murine A3 (mA3) protein that is involved in counteracting mouse retroviruses. mA3 is packaged into mouse mammary tumor virus (MMTV) particles where it inhibits the viral reverse transcriptase leading to a reduced viral replication and spread *in vivo* (94, 95). Furthermore, mA3 restricts Friend murine leukemia virus (F-MuLV) replication and pathogenesis *in vivo* in a deaminase-independent manner by contributing to the production of neutralizing antibodies to control viremia (96, 97).

Although beneficial in host defense against parasitic elements, the DNA-editing ability of A3 proteins is a double-edged sword, as it can also target genomic DNA. In fact, A3-associated mutational

signatures have been identified in 50% of human cancer genomes and were recently shown to stem mainly from A3A deaminase activity (98). Besides A3A, A3B and A3H also have access to the cell nucleus and are believed to contribute to the observed A3-associated mutagenesis in human cancers (99-101).

3.5 Ribonucleotide reductase in herpesviruses

Despite the genomic variation between herpesviruses reflecting their adaptation to different biological niches, genes involved in core processes of the viral replication cycle, such as DNA replication and particle assembly, are conserved across all three *Orthoherpesviridae* subfamilies. One of these conserved gene products is the large subunit of the viral ribonucleotide reductase (RNR), an enzyme involved in nucleotide metabolism. RNR catalyzes the substitution of the 2'OH-group of a ribonucleotide di- or triphosphate by a hydrogen atom in the *de novo* synthesis of deoxyribonucleoside triphosphates (dNTPs) (102, 103). All living organisms and large DNA viruses encode an RNR to supply dNTPs required for DNA replication and repair.

Herpesviral RNR structurally resembles its eukaryotic homologs and has most likely been captured from the host genome during co-evolution. It is characterized as a class I RNR based on its heterotetrameric structure composed of homodimers of the large (R1) and small subunit (R2) (104). The genes encoding each of the subunits are expressed with early kinetics during the lytic viral replication cycle. The R1 protein is the catalytic subunit that also contains the allosteric site for substrate specificity facilitating a balanced supply of all four dNTPs (105). The R2 protein is an iron-coordinating regulatory subunit that generates a free protein radical required for substrate activation (102). The virus-encoded RNR uncouples herpesvirus replication from cellular DNA replication, enabling productive infection of differentiated, non-dividing cells with low dNTP pools (106, 107).

The class I R1 subunits from herpesviruses to eukaryotes, including humans, share a conserved C-terminal homology domain (Fig. 4A). In contrast to the heterotetrameric, enzymatically active RNR of α- and γ-herpesviruses, β-herpesviruses lack a gene encoding the small R2 subunit. Moreover, their large R1 subunit displays only partial conservation of the catalytic residues and the nucleotide-binding site, resulting in a catalytically inactive enzyme (108-110). Instead of encoding their own nucleotide metabolic enzymes, β-herpesviruses manipulate the host cell cycle to ensure a sufficient supply of dNTPs. For instance, human cytomegalovirus (HCMV) inhibits cellular DNA synthesis by blocking cell cycle progression at the transition to the synthesis (S) phase, thereby exploiting the active cellular nucleotide metabolism for its own DNA replication (111-113).
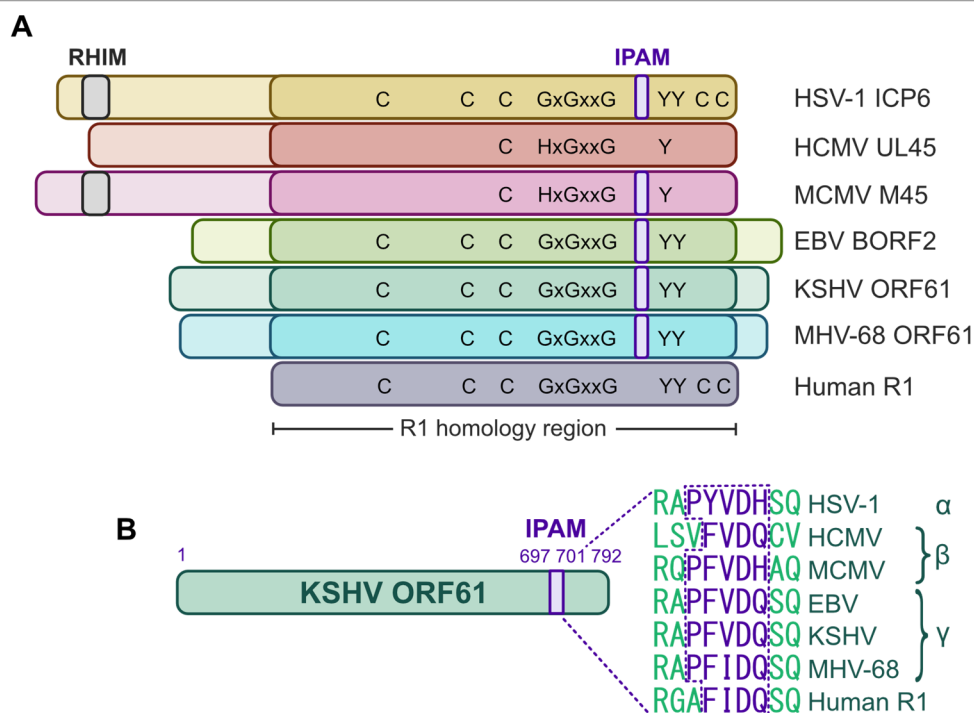
Figure 4. (A) Schematic representation of selected herpesvirus R1 proteins and the human R1 homolog with aligned R1 homology regions. The N-terminal RIP Homotypic Interaction Motif (RHIM) and the C-terminal Induced Protein Aggregation Motif (IPAM), as well as the nucleotide-binding site GxGxxG and the catalytic cysteine (C) and tyrosine (Y) residues are indicated. Adapted from Muscolino *et al.*, Int J Mol Sci., 2021 (114). (B) Localization of the IPAM in the KSHV ORF61 amino acid sequence and an alignment of the IPAM sequences within selected herpesvirus R1 proteins across all three subfamilies (α, β, γ) and in the human R1 homolog. Adapted from Luoto *et al.*, J Virol., 2025 (115).

3.5.1 Immune evasion functions of MCMV and HSV-1 R1 proteins

Interestingly, several herpesviruses have repurposed their R1 proteins for functions independent of nucleotide metabolism, a property that was first described for M45, the R1 protein of murine cytomegalovirus (MCMV) (116). M45 interferes with cellular innate immune signaling and promotes survival of infected cells by binding the cellular adaptor protein receptor-interacting protein kinase 1 (RIPK1) (117, 118) and nuclear factor (NF)-κB essential modulator (NEMO), a subunit of the NF-κB-activating IκB kinase (119). This leads to inhibition of a type of programmed cell death, known as necroptosis, and of NF-κB-mediated pro-inflammatory signaling. The inhibition mechanism involves sequestration of RIPK1 and NEMO in cytoplasmic protein aggregates that are subsequently recruited to autophagosomes for degradation by selective autophagy (119, 120). The M45 aggregate formation and target protein binding is dependent on a C-terminal Induced Protein Aggregation Motif (IPAM) that is conserved in the herpesviral R1 proteins across all three subfamilies (Fig. 4B). M45 aggregation most likely requires oligomerization, as mutating the IPAM abolishes both aggregation and M45 self-interaction (120). Besides IPAM, M45 interaction with RIPK1 involves a RIP Homotypic Interaction Motif (RHIM) that is present in the extended N-terminal domain of M45 (118) (Fig. 4A). Of note, UL45, the M45 homolog of HCMV, contains only a partially conserved IPAM (Fig. 4B).

IPAM-dependent R1 protein aggregation as a means to counteract the host immune response is not restricted to MCMV M45. The HSV-1 R1 protein ICP6, that contains both an N-terminal RHIM (121) and a C-terminal IPAM (120), also binds RIPK1 (122) and sequesters it in protein aggregates, thereby inhibiting necroptotic cell death. Similar to M45, the ICP6 aggregates form in an IPAM-dependent manner and are subject to autophagic degradation (120) (Fig. 5).
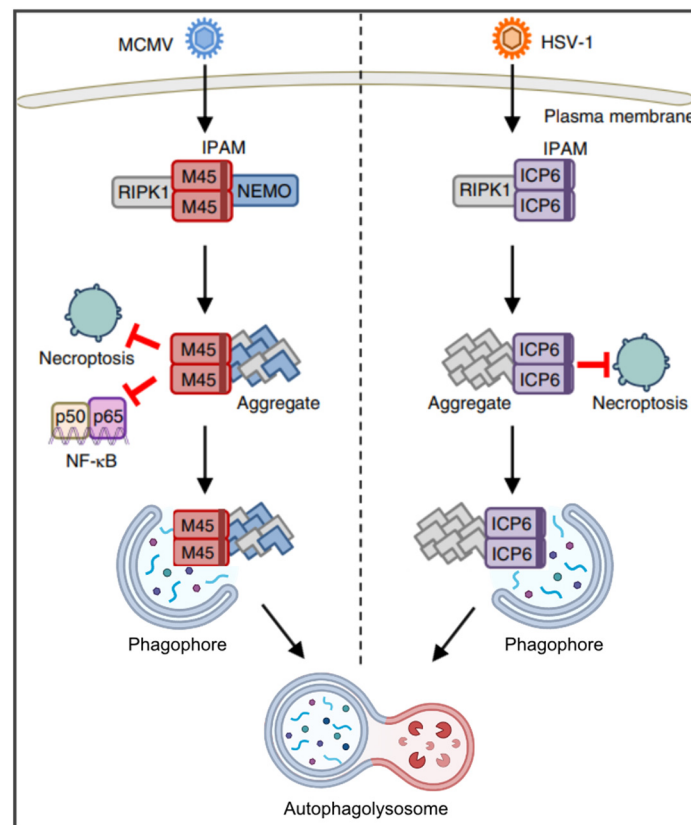
Figure 5. MCMV and HSV-1 R1 proteins are involved in counteracting the host immune response. The C-terminal IPAM mediates self-interaction of the R1 proteins and their binding to cellular targets. The R1-induced aggregation of the target proteins prevents downstream immune signaling. The aggregates are recruited to the forming phagophore and subsequently degraded by fusion of the mature autophagosome with the lysosome. Adapted from Muscolino *et al.*, Nat Microbiol., 2020 (120).

3.5.2 APOBEC3B inhibition by the EBV R1 protein

Herpesvirus dsDNA genome replication in the cell nucleus creates ssDNA intermediates that are suitable targets for deamination by nuclear A3 proteins. Indeed, the only constitutively nuclear A3 protein, APOBEC3B (A3B), has been shown to target the γ-herpesvirus EBV. In response, EBV has repurposed its R1 protein, BORF2, to shield the viral genome from deleterious deamination events during lytic replication. Consequently, a recombinant EBV lacking the *BORF2* gene exhibits reduced viral titers, decreased infectivity, and an accumulation of A3B-signature C/G-to-T/A mutations compared to the parental virus (123).

Among γ-herpesvirus R1 proteins, BORF2 was the first to be assigned a function beyond dNTP synthesis. BORF2 achieves A3B neutralization by a combination of two distinct mechanisms. It directly inhibits A3B deaminase activity by engaging a large surface of the A3B C-terminal catalytic

domain (ctd), primarily loop 7 (L7) and loop 1 (L1) residues, thereby precluding A3B interaction with the ssDNA substrate (123, 124). Furthermore, it relocalizes A3B out of the nucleus and sequesters it in large, pleomorphic condensates in the cytoplasm (123). The cryo-electron microscopy (-EM) structure of the BORF2-A3Bctd complex, together with subsequent mutagenesis experiments, suggests that BORF2 dimerization at the N-terminal interface is required for higher-order condensate formation but not for A3B relocalization. Intriguingly, this interface does not overlap with the region that is involved in canonical R1 dimerization required for RNR activity, suggesting that BORF2 exists in cells in at least two different dimeric complexes (124).

The BORF2 residues L133 and Y134, that make contact with A3Bctd, map to a novel short helix insertion (SHI), whereas the interacting residues Y481 and R484 are part of an additional helical loop structure (HLS). BORF2 SHI and HLS are not conserved in eukaryotic R1 proteins but likely represent evolutionary viral adaptations to facilitate efficient A3B neutralization (124).

R1-mediated herpesviral A3B countermeasures are not unique to EBV. In fact, this host-pathogen interaction likely dates back to the emergence of the ancestral *A3B* gene in the primate lineage leading to humans and other Old World anthropoids. In support of this hypothesis, only the R1 proteins of γ-herpesviruses that infect A3B-encoding primate species are capable of binding to human A3B and altering its subcellular localization (125). Accordingly, the R1 protein ORF61 of the human pathogenic KSHV alone is sufficient to confer A3B accumulation in cytoplasmic condensates in transfected cells (126).

Reminiscent of lytic EBV infection, the α-herpesvirus HSV-1 relocalizes A3B from the nucleus to the cytoplasm in an R1-dependent manner in infected cells, supporting a mechanistic conservation beyond the γ-subfamily, albeit with less prominent cytoplasmic R1 condensate formation (126). In contrast to BORF2-null EBV, the presence of A3B does not impair HSV-1 ΔICP6 replication compared to the parental virus, suggesting that HSV-1 might encode additional A3B inhibitors or be less susceptible to A3B-mediated deamination (126). Interestingly, A3B relocalization is also induced by the β-herpesvirus HCMV, but the approach differs mechanistically from that observed with HSV-1 and γ-herpesviruses. Instead of the viral R1 protein UL45, which is dispensable for A3B relocalization, an as-yet-undefined mechanism involving at least one viral protein present early in HCMV infection appears to mediate A3B relocalization to the cytoplasmic compartment (127).

4. Aim of the study

The large dsDNA genomes of herpesviruses encode a vast array of proteins, many of which have multiple functions. In addition to its role in nucleotide metabolism, several herpesviruses have repurposed the large, catalytic R1 subunit of the viral ribonucleotide reductase to subvert cellular immune defenses.

The MCMV R1 protein M45 induces aggregation and subsequent autophagic degradation of cellular RIPK1 and NEMO to prevent necroptosis and NF-κB-mediated inflammatory signaling. This process requires a C-terminal Induced Protein Aggregation Motif (IPAM) that is conserved in herpesviral R1 homologs across all subfamilies. HSV-1 similarly employs its R1 protein ICP6 to bind and sequester RIPK1 in an IPAM-dependent manner, whereas the γ-herpesvirus EBV uses its R1 protein BORF2 to relocalize the cellular cytosine deaminase APOBEC3B (A3B) from the nucleus, the site of viral DNA replication, to the cytoplasm to prevent deleterious mutations. Whether R1-mediated countermeasures of the host immune response are a conserved feature in γ-herpesvirus infection has not been investigated.

The aim of the present work was the first detailed characterization of the R1 protein ORF61 of KSHV and MHV-68, two γ-herpesviruses of the genus *Rhadinovirus*. The study aimed to uncover whether rhadinovirus R1 proteins aggregate in an IPAM-dependent manner during infection and whether the aggregates are subject to autophagy. Furthermore, the study pursued to visualize structural details of R1 aggregates in infected cells and to investigate the conservation of R1-mediated A3B countermeasures in rhadinovirus infection. To identify as-yet-unknown targets of rhadinovirus R1 proteins, a proteomics-based approach was employed.

5. Results

5.1 Rhadinovirus R1 proteins form elongated cytoplasmic condensates

MCMV and HSV-1 R1 proteins are known to aggregate in the cytoplasm of infected cells to sequester cellular target proteins. This process is dependent on a C-terminal IPAM motif that is conserved in the R1 proteins across all three herpesvirus subfamilies (Fig. 4). To test if the R1 protein of KSHV, a human pathogenic γ-herpesvirus of the genus *Rhadinovirus*, forms similar condensates in infected cells in an IPAM-dependent manner, fluorescently tagged recombinant KSHVs were constructed using *en passant* mutagenesis (see 8.1.11). To create a lytically replicating KSHV mNeon-ORF61, a green fluorescent protein (mNeonGreen) was N-terminally fused to the KSHV R1 protein ORF61 in a KSHV bacterial artificial chromosome (BAC) clone (KSHV$_{Lyt}$) that is engineered to constitutively express the viral replication and transcription activator (RTA) protein (128). This virus in turn served as a backbone for KSHV mNeon-ORF61*mut*IPAM, in which the IPAM was disrupted by two alanine substitutions (PFVDQ to PFVAA). ARPE-19 human epithelial cells were then infected with both viruses and the mNeon-positive structures imaged by confocal laser scanning microscopy (cLSM). As shown in Fig. 6A, mNeon-ORF61 underwent dynamic morphological changes in the course of infection from small dot-like perinuclear structures at 24 hours post-infection (hpi) to elongated condensates of considerable size at 48 hpi. In contrast, when the IPAM was mutated, ORF61 did not form large condensates even at later times (72 hpi) but instead stayed mainly dispersed across the cytoplasm apart from occasional small dots (Fig. 6A, lower panels). This suggests that the formation of elongated KSHV ORF61 condensates is an IPAM-dependent process. To ensure that the condensate formation was not dependent on a specific cell type, telomerase-immortalized microvascular endothelial (TIME) cells were infected with KSHV mNeon-ORF61 and imaged by cLSM (Fig. 6B). In line with the observations in epithelial cells, small mNeon-positive dots were detected after 24 h and larger elongated condensates later in infection, suggesting that ORF61 condensate formation is not restricted to a certain cell type.
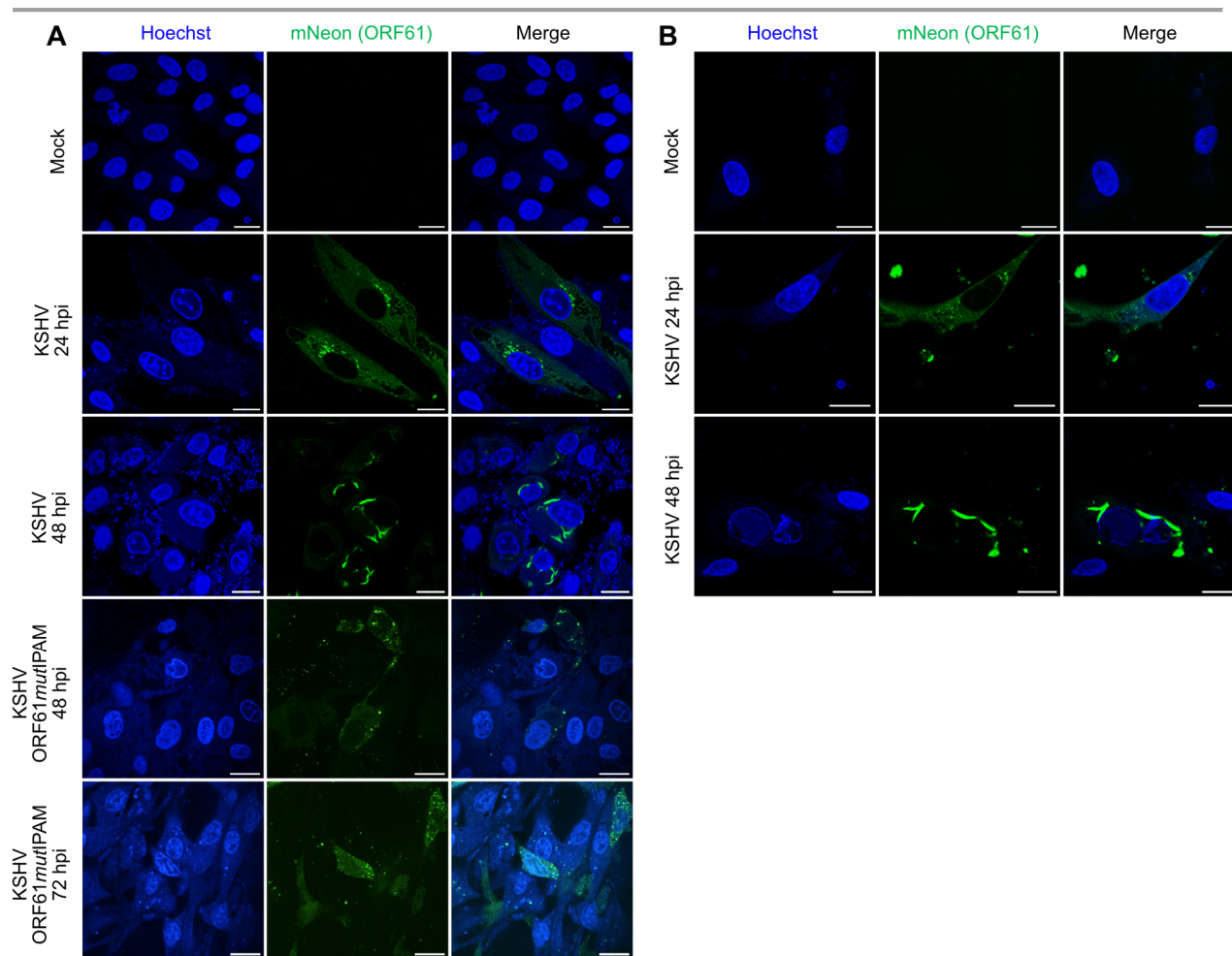
Figure 6. KSHV ORF61 forms IPAM-dependent elongated cytoplasmic condensates independent of the cell type. Confocal microscopy images of (A) ARPE-19 epithelial cells infected with KSHV mNeon-ORF61 or mNeon-ORF61*mut*IPAM and (B) TIME endothelial cells infected with KSHV mNeon-ORF61. Cells were fixed at indicated times post-infection, and nuclei were counterstained with Hoechst 33342. Fluorescence images were acquired by cLSM. Scale bar, 20 μm.

To test whether the peculiar morphology of the ORF61 condensates is a conserved feature of γ-herpesviruses, ORF61 of MHV-68, a related rodent rhadinovirus, was analyzed. Analogous to the KSHV mutant described above, an MHV-68 ORF61-mNeon recombinant virus was created using *en passant* mutagenesis. As N-terminal tagging of MHV-68 ORF61 altered the morphology of the protein (data not shown), the tag was instead introduced to the C-terminus. Upon infection of mouse fibroblasts, MHV-68 ORF61-mNeon formed condensates that appeared as small dot-like structures early in infection (6 hpi), as observed by cLSM, and grew to acquire an elongated shape at 24 hpi (Fig. 7A), structurally resembling KSHV ORF61 (Fig. 6). To ensure that the observed ORF61 morphology was not an artifact caused by the mNeonGreen tag, a small FLAG epitope tag was C-terminally fused to MHV-68 ORF61 to create an ORF61-FLAG recombinant virus. Mouse fibroblasts were then infected with MHV-68 ORF61-FLAG, FLAG-positive structures were visualized by immunofluorescence staining early and late in infection and analyzed by cLSM. As shown in Fig. 7B, the morphology of ORF61-FLAG condensates resembled that of their mNeon-tagged counterparts. To investigate the importance of IPAM for MHV-68 ORF61 condensate formation, an

38

ORF61*mut*IPAM-FLAG virus was constructed by introducing two alanine substitutions (PFIDQ to PFVAA) to the IPAM amino acid sequence. Reminiscent of the KSHV IPAM mutant, MHV-68 ORF61*mut*IPAM lost the ability to form large condensates, and ORF61 was instead present throughout the cytoplasm even at a later time point (Fig. 7B). This indicated that an intact IPAM is a prerequisite for MHV-68 ORF61 condensate formation.
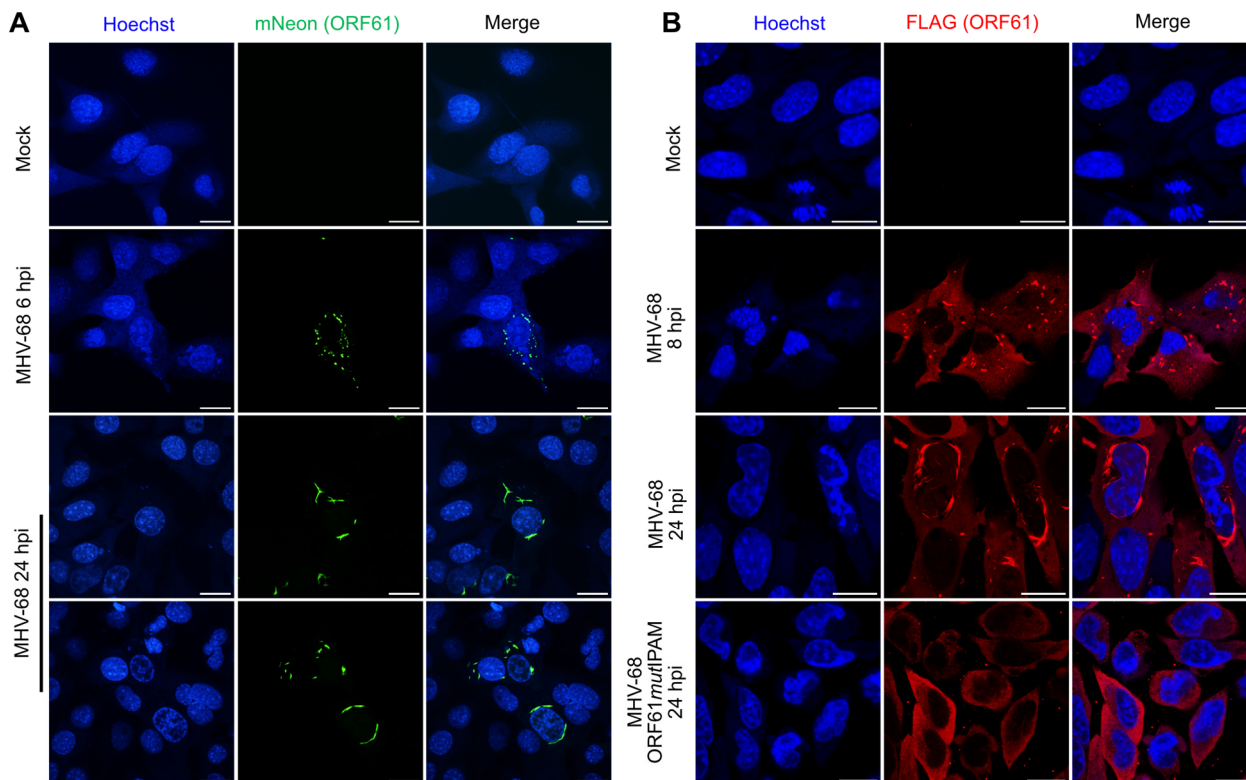
Figure 7. MHV-68 ORF61 accumulates in IPAM-dependent elongated cytoplasmic condensates. Confocal microscopy images of (A) MEF cells infected with MHV-68 ORF61-mNeon and (B) murine 10.1 fibroblasts infected with MHV-68 ORF61- or ORF61*mut*IPAM-FLAG. Cells were fixed at indicated times post-infection, and nuclei were counterstained with Hoechst 33342. 10.1 cells were immunostained with an anti-FLAG antibody. Fluorescence images were acquired by cLSM. Scale bar, 20 μm.

5.2 Rhadinovirus R1 proteins become insoluble during infection

As shown in Figs. 6 and 7, KSHV and MHV-68 R1 proteins undergo dynamic structural changes during infection, and this reorganization requires an intact IPAM. To assess the impact of these changes on the solubility of the R1 proteins, ARPE-19 cells were infected with KSHV expressing mNeon-tagged ORF61 (Fig. 8A) and mouse fibroblasts with MHV-68 expressing FLAG-tagged ORF61 (Fig. 8B). The infected cell lysates were then separated into soluble and insoluble fractions by centrifugation at different times post-infection, and ORF61 detected by immunoblot. At early times, the ORF61 protein of both viruses was predominantly soluble but accumulated in the insoluble fraction as the infection proceeded. In contrast, such a change in solubility was not observed with ORF61*mut*IPAM which stayed soluble throughout the infection, further illustrating the importance of the IPAM for the structural properties of ORF61. Although a small amount of insoluble KSHV ORF61*mut*IPAM was

detected, the levels were considerably lower compared to ORF61 and remained constant over time without a gradual increase.
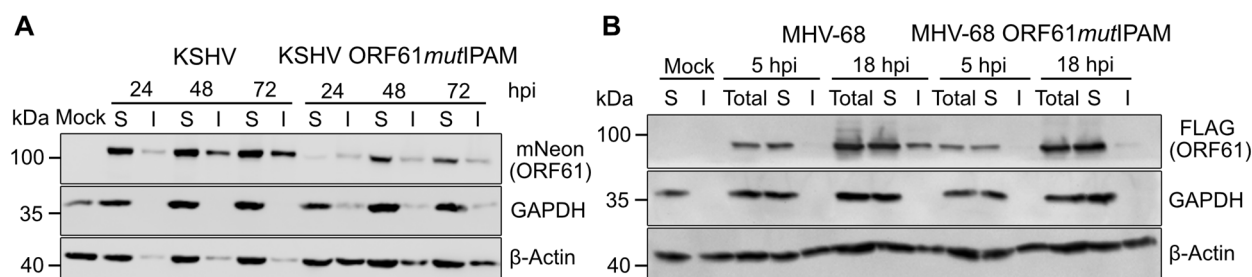

Figure 8. Rhadinovirus R1 proteins become insoluble during infection. (A) ARPE-19 cells were infected with KSHV mNeon-ORF61 or mNeon-ORF61*mut*IPAM (MOI 0.1 TCID$_{50}$/cell) and harvested at different times post-infection. The detergent-soluble (S) and -insoluble (I) fractions were analyzed by immunoblot. GAPDH was used as a fractionation control and β-Actin as a loading control. (B) Murine 10.1 fibroblasts were infected with MHV-68 ORF61-FLAG or ORF61*mut*IPAM-FLAG (MOI 2 TCID$_{50}$/cell) and harvested at different times post-infection. Total cell lysates and the detergent-soluble (S) and insoluble (I) fractions were analyzed by immunoblot.

5.3 Rhadinovirus R1 protein condensates are not subject to autophagy

MCMV and HSV-1 R1 protein aggregates have been shown to be degraded by autophagy (120). To test if insoluble ORF61 is similarly targeted to autophagic degradation, ARPE-19 cells were infected with KSHV mNeon-ORF61 and mouse fibroblasts with MHV-68 ORF61-FLAG in the presence or absence of the autophagy inhibitor 3-methyladenine (3-MA). At 24 hpi, the infected cell lysates were separated into soluble and insoluble fractions, and ORF61 was detected by immunoblot (Fig. 9A). In contrast to the MCMV R1 protein M45, which accumulated in the insoluble fraction upon 3-MA treatment and was used as a positive control, the amount of insoluble KSHV and MHV-68 ORF61 was not altered by autophagy inhibition, suggesting that autophagy does not play a crucial role in the turnover of ORF61 aggregates.

To further corroborate these findings in a genetic knockout setting, autophagy-deficient *Atg5*$^{-/-}$ mouse fibroblasts and corresponding *Atg5*$^{+/+}$ control cells were infected with MHV-68 ORF61-FLAG, and the accumulation of insoluble ORF61 was compared by immunoblot using MCMV M45-HA infection as a control. Consistent with the outcome of pharmacologic autophagy inhibition, the amount of insoluble MHV-68 ORF61 in *Atg5*$^{-/-}$ cells was not increased compared to control cells (Fig. 9B), confirming that autophagy is not substantially involved in the turnover of ORF61 aggregates.
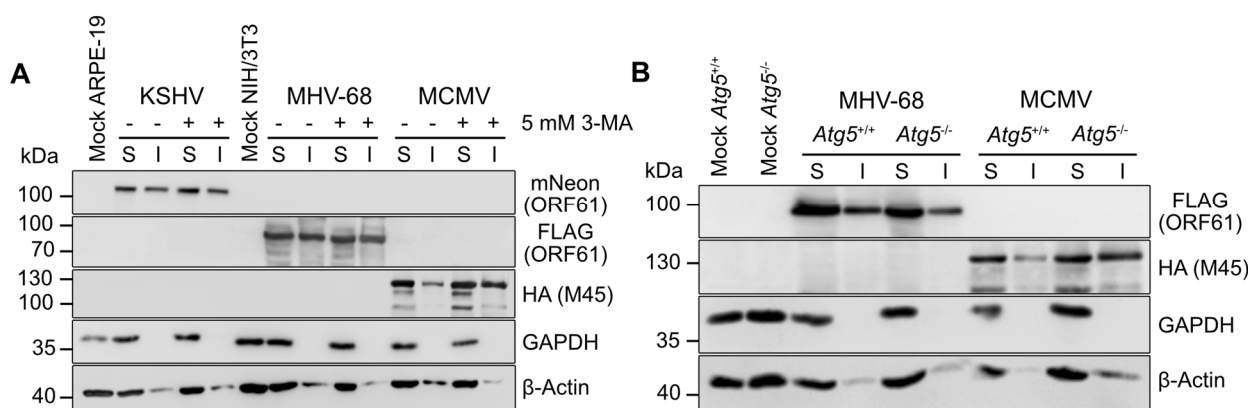
Figure 9. Rhadinovirus R1 proteins are not subject to autophagy. (A) ARPE-19 cells were infected with KSHV mNeon-ORF61 at MOI 0.1 $TCID_{50}$/cell and NIH/3T3 mouse fibroblasts with either MHV-68 ORF61-FLAG or MCMV M45-HA at MOI 5 $TCID_{50}$/cell. At 6 hpi, cells were treated with 5 mM 3-methyladenine (3-MA) until lysate collection to inhibit autophagy or left untreated. Cell lysates were collected at 24 hpi and separated into soluble (S) and insoluble (I) fractions. (B) $Atg5^{+/+}$ and $Atg5^{-/-}$ MEF cells were infected with either MHV-68 ORF61-FLAG or MCMV M45-HA at MOI 3 $TCID_{50}$/cell. At 24 hpi, cell lysates were harvested and separated into soluble (S) and insoluble (I) fractions.

5.4 ORF61 protein condensates are solid filamentous aggregates

For a further structural characterization of the strikingly shaped KSHV and MHV-68 ORF61 condensates, they were expressed as mCherry-tagged fusion proteins in U2OS cells and analyzed by fluorescence recovery after photobleaching (FRAP) in collaboration with Enrico Caragliano (CSSB/LIV). At 24 h post-transfection, 1 μm-diameter areas of the fluorescent condensates were bleached with a 563 nm laser and the recovery of fluorescence recorded at 2 frames per second for 6 min (Fig. 10A). In contrast to the liquid mCherry-Nucleolin condensates, that recover fluorescence rapidly upon bleaching (120, 129) and served as a soluble control, no recovery was observed with the mCherry-tagged ORF61 condensates (Figs. 10B and 10C), suggesting that they are indeed solid protein aggregates.
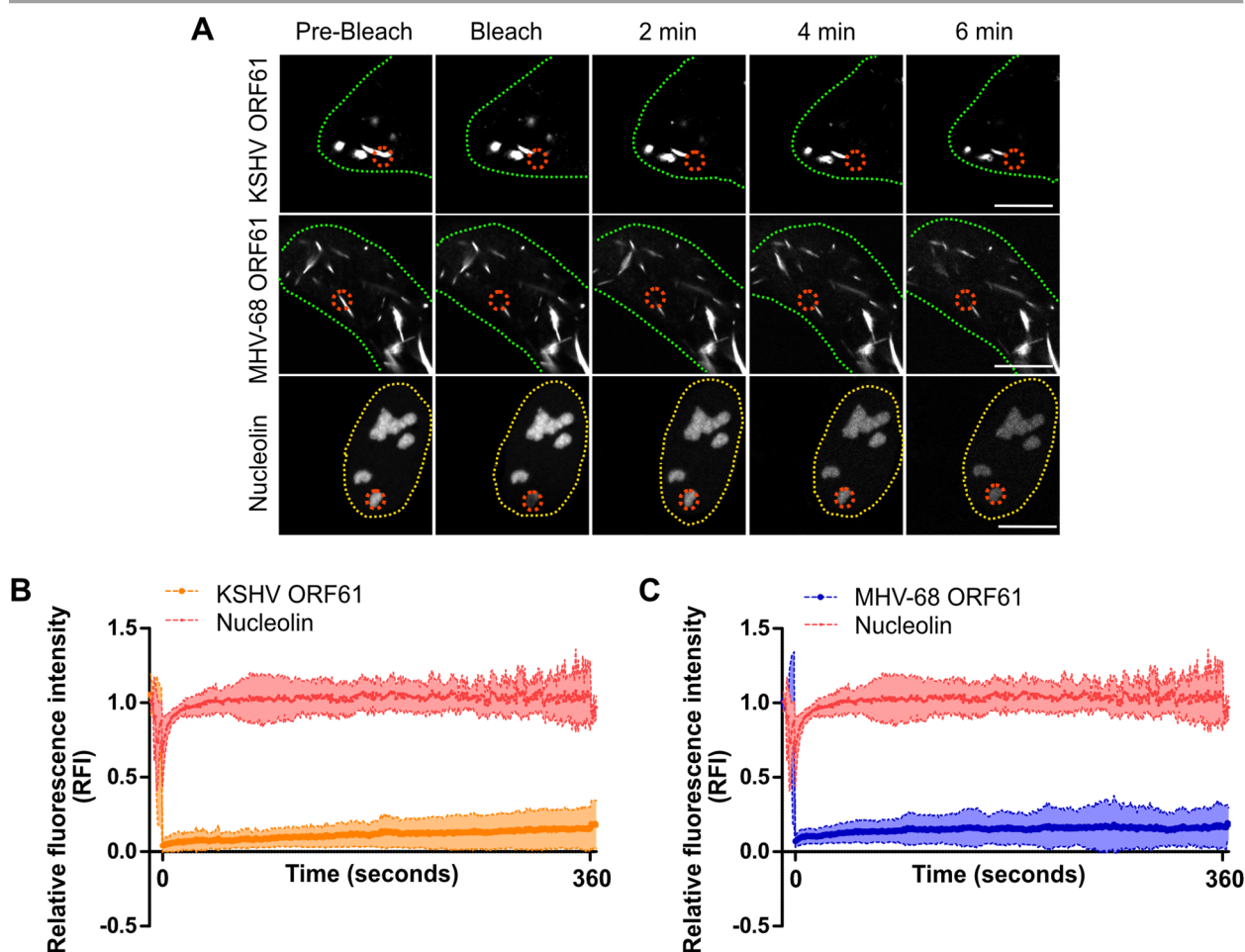
**Figure 10. Rhadinovirus ORF61 protein condensates display properties of solid aggregates.** (A) Fluorescence recovery after photobleaching (FRAP) analysis of mCherry-tagged R1 proteins. KSHV and MHV-68 ORF61-pmCherry were expressed in U2OS cells by plasmid transfection. 24 h later, mCherry-positive structures were half-bleached, and fluorescence recovery was recorded at 2 frames per second for 6 min. pmCherry-Nucleolin was used as a soluble control. Scale bar, 10 μm. (B and C) Relative fluorescence intensity (RFI) of bleached areas over time in at least ten different cells per sample. The shaded areas are the mean values ± SEM. Data generated in collaboration with Enrico Caragliano (CSSB/LIV).

To gain more insight into the structure of ORF61 aggregates in the context of infection, correlative light and electron microscopy (CLEM) was used to analyze cells infected with either KSHV or MHV-68 expressing an mNeon-tagged ORF61 (in collaboration with Carola Schneider and Rudolph Reimer, LIV). At 40 hpi (KSHV) and 20 hpi (MHV-68), the cells were fixed and fluorescent Z-stacks of the mNeon-positive aggregates acquired by cLSM. Ultrathin serial sections of the same cells were then prepared and imaged by transmission electron microscopy (TEM). Finally, the EM images were correlated with the mNeon-positive structures observed in the confocal images to obtain a high-resolution view of individual aggregates. Interestingly, the CLEM analysis showed that the elongated ORF61 aggregates of both KSHV and MHV-68 were composed of filament bundles. In the case of KSHV ORF61, the filaments were rather loosely packed with single filaments being clearly visible (Fig. 11A), whereas MHV-68 ORF61 formed more compact stacks of filaments (Fig. 11B).
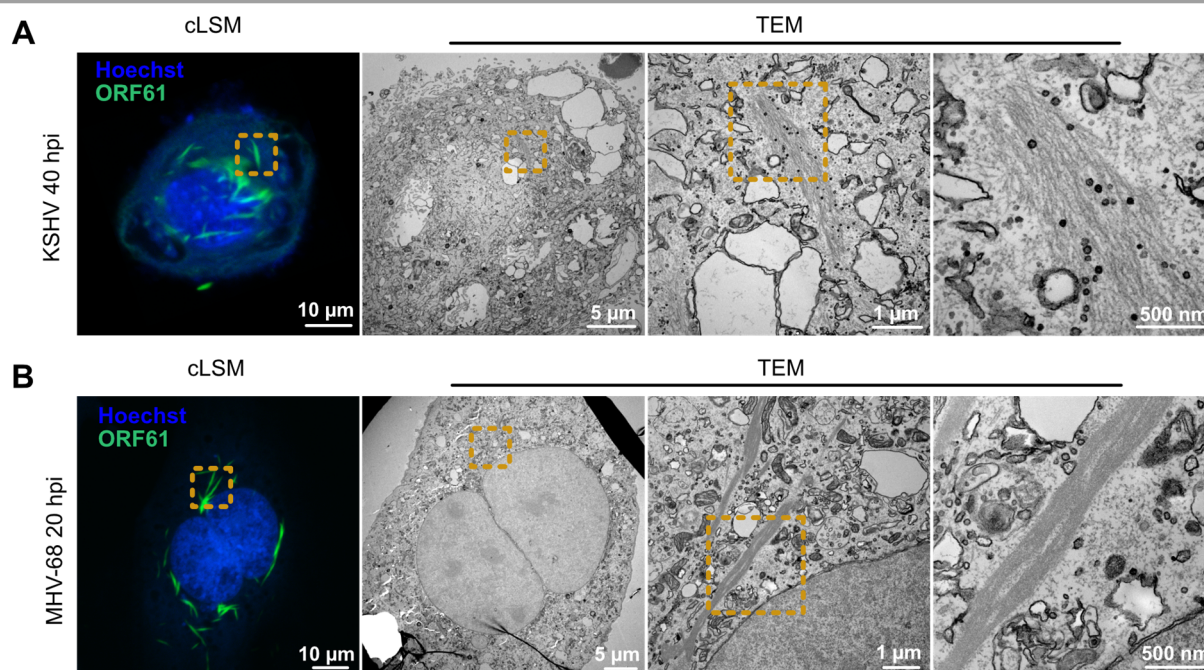
Figure 11. Rhadinovirus ORF61 aggregates are composed of filament bundles. Correlative light and electron microscopy (CLEM) of ORF61 aggregates. (A) ARPE-19 cells were infected with KSHV mNeon-ORF61, and (B) MEF cells with MHV-68 ORF61-mNeon. At 40 hpi (KSHV) or 20 hpi (MHV-68), cells were fixed, and nuclei were stained with Hoechst 33342. Fluorescent Z-stacks were acquired by cLSM. Ultrathin 50 nm serial sections of the samples were prepared and imaged by transmission electron microscopy (TEM). Representative overview images and magnified views of the indicated areas are shown. Data generated in collaboration with Carola Schneider and Rudolph Reimer (LIV).

5.5 Filamentous ORF61 aggregates do not contain F-actin or vimentin

To investigate whether cellular cytoskeletal filaments are present in the ORF61 aggregates, F-actin was visualized by rhodamine phalloidin staining in cells infected with either KSHV or MHV-68 expressing mNeon-tagged ORF61. At 48 hpi (KSHV) or 18 hpi (MHV-68), cells were fixed and stained with rhodamine phalloidin. As shown in Fig. 12A, the phalloidin signal did not co-localize with the mNeon-positive aggregates, suggesting that the filamentous ORF61 aggregates do not contain F-actin. To test if ORF61 aggregates are associated with the intermediate filament protein vimentin that is present in mesenchymal cells, such as fibroblasts (130), human foreskin fibroblasts (HFF) were infected with KSHV mNeon-ORF61. At 24 and 48 hpi, cells were fixed to visualize vimentin by indirect immunofluorescence. Vimentin encircles cellular deposits for aggregated and misfolded proteins termed aggresomes (131), but it was not detected within or surrounding ORF61 aggregates (Fig. 12B). Taken together, these data suggested that the elongated filamentous aggregates formed by the rhadinovirus ORF61 proteins do not contain F-actin or vimentin.
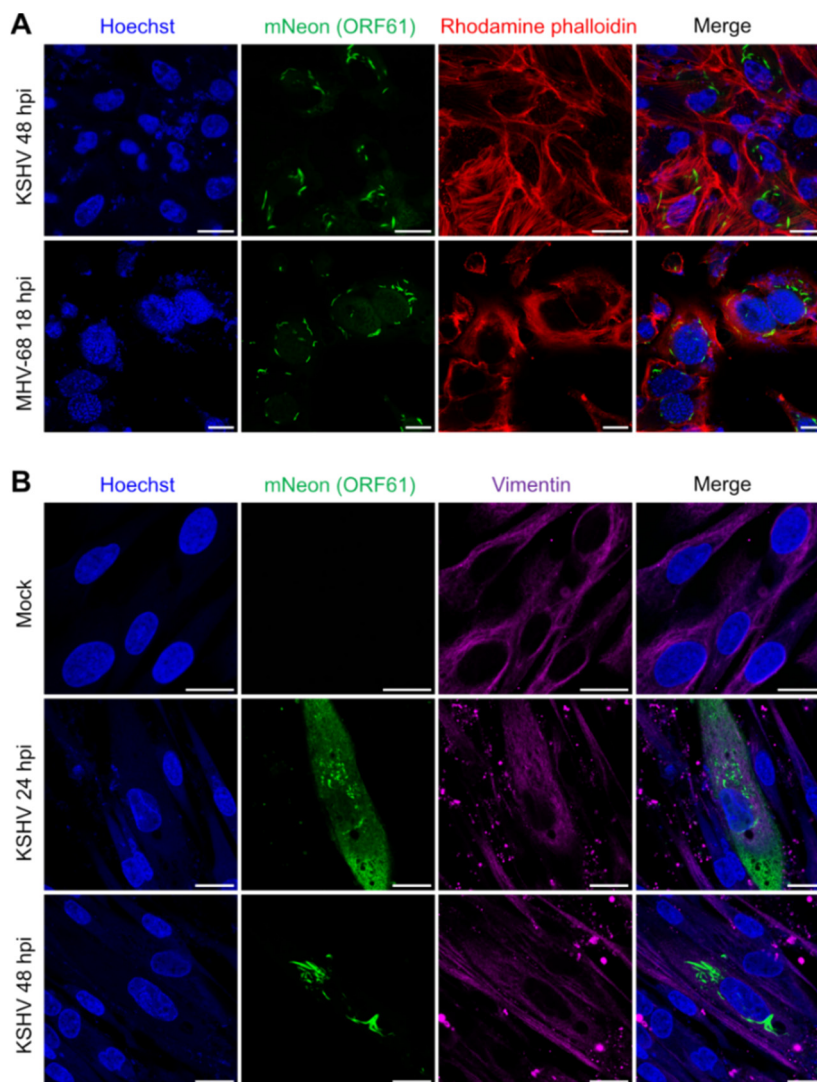
Figure 12. Filamentous ORF61 aggregates do not contain F-actin or vimentin. (A) Confocal microscopy images of ARPE-19 cells infected with KSHV mNeon-ORF61 and MEF cells infected with MHV-68 ORF61-mNeon. At 48 hpi (KSHV) or 18 hpi (MHV-68), cells were fixed, F-actin was stained with rhodamine phalloidin, and nuclei were stained with Hoechst 33342. Fluorescence images were acquired by cLSM. (B) HFF cells were infected with KSHV mNeon-ORF61, fixed at 24 or 48 hpi, stained with an anti-vimentin antibody and Hoechst 33342, and analyzed by cLSM. Scale bar, 20 μm.

5.6 APOBEC3B localizes to KSHV ORF61 aggregates in transfected cells

Previous studies have demonstrated that the EBV and HSV-1 R1 proteins, BORF2 and ICP6, relocalize the cellular cytosine deaminase APOBEC3B (A3B) out of the nucleus and sequester it in the cytoplasm to protect the replicating viral genome from its mutagenic effect (123, 126). To test if A3B similarly localizes to the KSHV ORF61 aggregates and if the IPAM is involved in the process, U2OS cells were transfected with FLAG-tagged KSHV ORF61 or ORF61*mut*IPAM and HA-tagged A3 expression plasmids. A3G, a cytoplasmic A3 enzyme, was included as a control to rule out a general effect on A3 proteins, and the tagged proteins were detected by indirect immunofluorescence. As shown by the confocal microscopy images in Fig. 13, A3B was excluded from the nuclei and co-localized with ORF61 aggregates in the cytoplasm of co-transfected cells, whereas A3G did not. In contrast, ORF61*mut*IPAM, that was unable to form cytoplasmic aggregates, did not alter A3B localization.

44
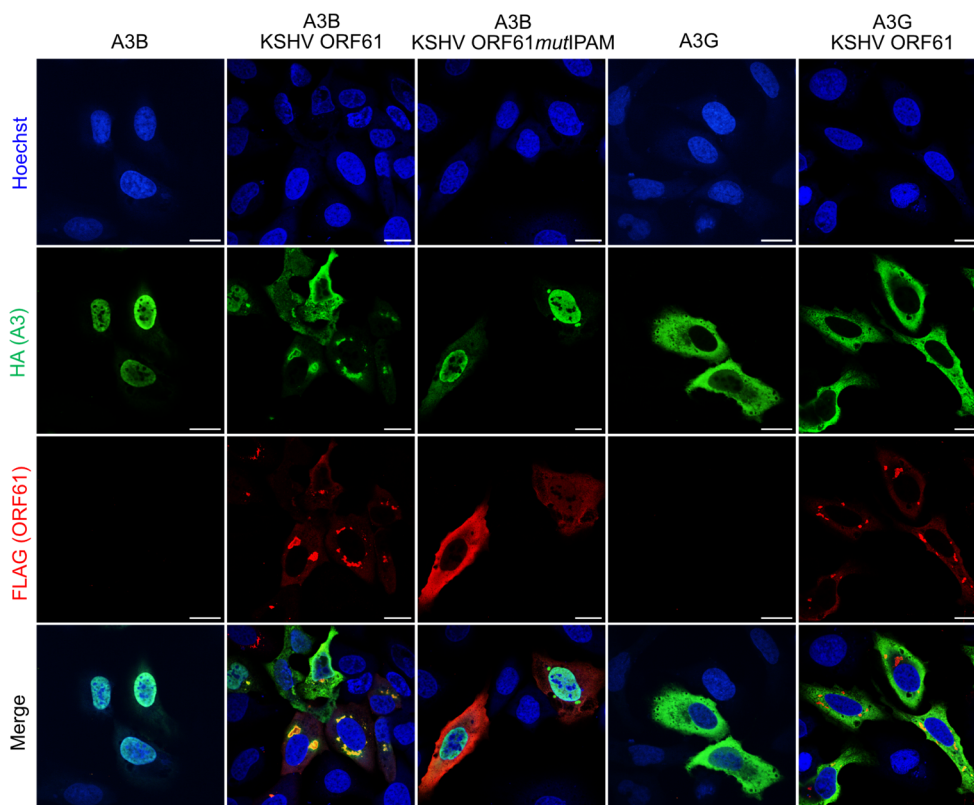
Figure 13. A3B relocalizes from the nucleus to the cytoplasmic KSHV ORF61 aggregates in transfected cells. U2OS cells were transfected with plasmids expressing A3B-HA or A3G-HA and KSHV ORF61-FLAG or ORF61*mut*IPAM-FLAG. Cells were fixed, immunostained with anti-HA and anti-FLAG antibodies and counterstained with Hoechst 33342. Fluorescence images were acquired by cLSM. Scale bar, 20 μm.

5.7 MHV-68 ORF61 does not relocalize human or mouse APOBECs

To investigate whether the observed structural similarity between KSHV and MHV-68 ORF61 aggregates (Fig. 11) also translates to their cellular interaction partners, U2OS cells were transfected with FLAG-tagged MHV-68 ORF61 and either HA-tagged A3B or A3G, followed by indirect immunofluorescence analysis of protein localization. As shown by the confocal microscopy images in Fig. 14, A3B did not localize to the cytoplasmic MHV-68 ORF61 aggregates but instead remained in the nucleus, suggesting that MHV-68 ORF61 does not share the ability of its KSHV homolog to sequester human A3B. This observation reflects the cellular environment naturally encountered by the virus during infection, since the rodent host species of MHV-68 lack A3B and only express a single cytoplasmic APOBEC3 protein (59). However, as the immunofluorescence staining of co-transfected U2OS cells in Fig. 14 shows, neither the cytoplasmic murine APOBEC3 (mA3) nor the more distantly related mA1 with a cell-wide localization co-localized with MHV-68 ORF61, suggesting that MHV-68 ORF61 does not sequester the tested APOBEC proteins of its host in cytoplasmic aggregates.
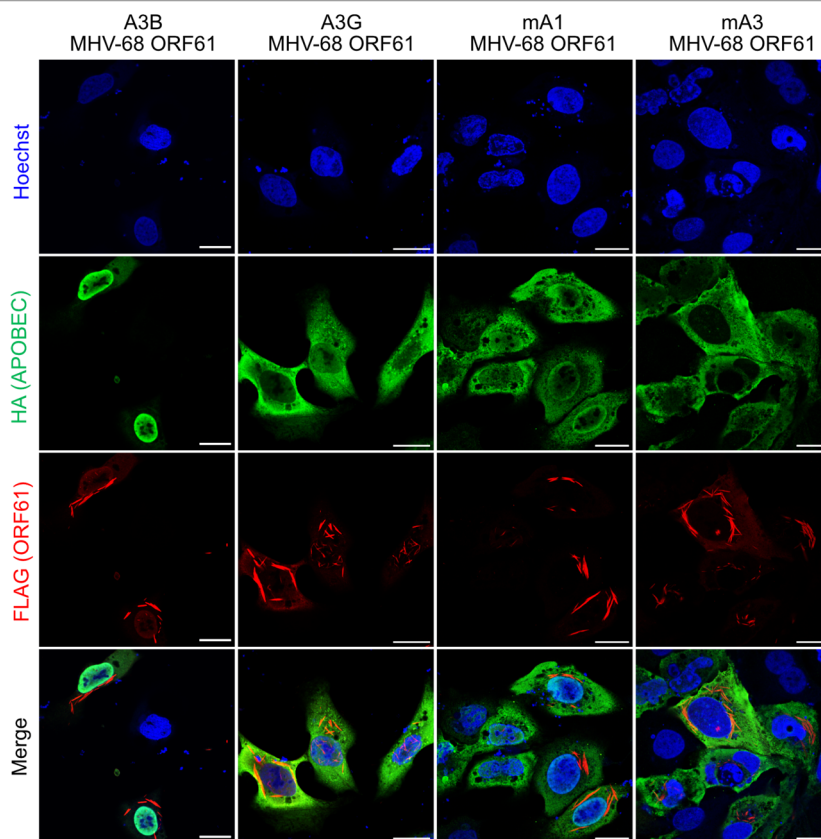
Figure 14. MHV-68 ORF61 does not relocalize human or mouse APOBECs. U2OS cells were transfected with plasmids expressing A3B-HA, A3G-HA, mA1-HA, or mA3-HA and MHV-68 ORF61-FLAG. Cells were fixed, immunostained with anti-HA and anti-FLAG antibodies and counterstained with Hoechst 33342. Fluorescence images were acquired by cLSM. Scale bar, 20 μm.

5.8 Rhadinovirus R1 proteins do not interact with RIPK1 or NEMO

Apart from A3B, herpesviral R1 proteins are known to interact with other cellular factors: HSV-1 ICP6 binds RIPK1, and MCMV M45 binds both RIPK1 and NEMO to prevent necroptosis and NF-κB signaling (117-120, 122). To test whether rhadinovirus R1 proteins share the same cellular targets, KSHV and MHV-68 ORF61-HA were co-expressed with either FLAG-tagged human or murine RIPK1 or murine NEMO in HEK-293A cells. At 24 h post-transfection, the R1 proteins were immunoprecipitated using an anti-HA antibody, and the co-precipitating proteins were visualized by immunoblot (Fig. 15). While RIPK1 and NEMO co-precipitate with MCMV M45, they were not detected in ORF61 precipitates, indicating that these interactions are not conserved in rhadinoviruses.
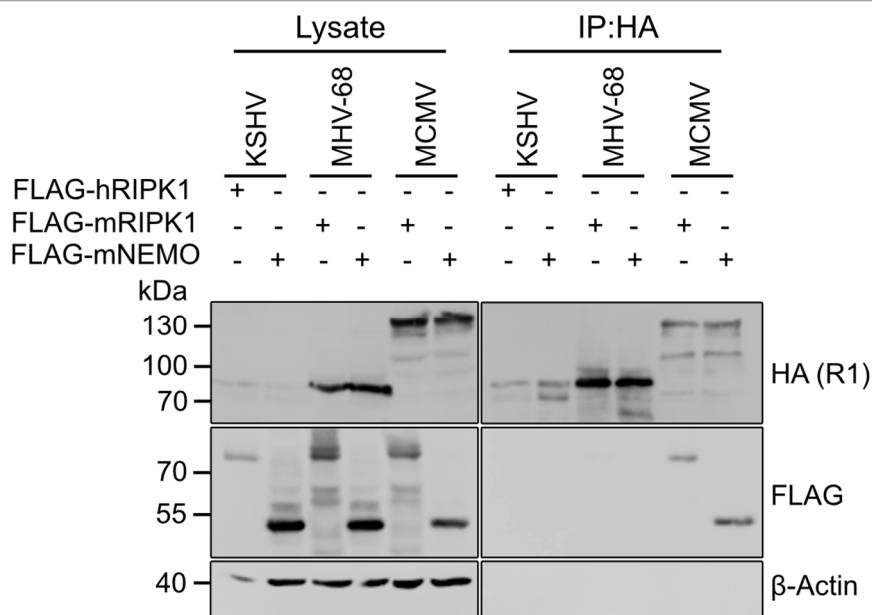
Figure 15. Unlike the homologous MCMV M45, rhadinovirus R1 proteins do not interact with RIPK1 or NEMO. HEK-293A cells were transfected with plasmids encoding HA-tagged R1 proteins and FLAG-tagged human or murine RIPK1 or murine NEMO. At 24 h post-transfection, cells were lysed and R1 proteins precipitated using an anti-HA antibody. Co-precipitating proteins were visualized by immunoblot. MCMV M45 was used as a positive control.

5.9 KSHV ORF61 requires an intact IPAM for A3B binding and relocalization during lytic infection

To overcome the lack of a commercially available anti-A3B antibody suitable for immunofluorescence and to be able to study the interplay between ORF61 and A3 proteins in an infectious context, RPE-1 human epithelial cells stably expressing doxycycline-inducible tagged A3B and A3G were generated. A3B and A3G, under the control of a tetracycline-responsive element (TRE) promoter, were fused to the red fluorescent protein mScarlet and an HA epitope tag for detection by fluorescence microscopy and immunoblot, respectively. The Tet-inducible expression of mScarlet-HA-tagged A3B or A3G was verified by treating the cells with increasing concentrations of doxycycline for 24 h and detecting the A3 proteins by immunoblot (Fig. 16A). The cells were then infected with KSHV mNeon-ORF61, mNeon-ORF61*mut*IPAM or MHV-68 ORF61-mNeon, and A3 expression was induced 16 h later with 1 µg/ml doxycycline. At 40 hpi, cell lysates were collected and the mNeon-tagged ORF61 proteins precipitated. As shown by the immunoblot of co-precipitating proteins, A3B co-precipitated only with KSHV ORF61 but not with KSHV ORF61*mut*IPAM or MHV-68 ORF61 (Fig. 16B), thereby confirming the phenotype observed in transfected cells (Figs. 13 and 14). A3G did not co-precipitate with either of the ORF61 proteins.

To corroborate the immunoprecipitation results, A3B- and A3G-mScarlet-expressing cells were infected with either KSHV mNeon-ORF61 or mNeon-ORF61*mut*IPAM. At 16 hpi, A3 expression was induced with 1 µg/ml doxycycline, and at 48 hpi cells were fixed and imaged by cLSM (Fig. 16C). To determine the co-localization rate between ORF61 and A3 proteins, Pearson's correlation coefficient was calculated for ORF61 and A3 signals using Z-stacks ($n = 10$) acquired for each condition. To

assess changes in the subcellular localization of A3B, nuclear A3B intensity (%) of each sample (n = 12) was determined as a percentage of the sum A3B fluorescence intensity of the whole cell (both analyses in collaboration with Enrico Caragliano, CSSB/LIV). As shown in Figs. 16C to E, A3B-mScarlet was relocalized out of the nucleus to the cytoplasm where it accumulated in the filamentous ORF61 aggregates. Consistent with the immunoprecipitation data, disruption of the IPAM precluded co-localization, and the ORF61*mut*IPAM virus failed to relocalize A3B that remained in the nucleus (Figs. 16C to E). Similarly, the localization of cytoplasmic A3G was not altered and it did not localize to the ORF61 aggregates (Figs. 16C and 16D). Taken together, the immunoprecipitation and fluorescence microscopy results indicate that KSHV ORF61 sequesters A3B in cytoplasmic aggregates in an IPAM-dependent manner during lytic infection.
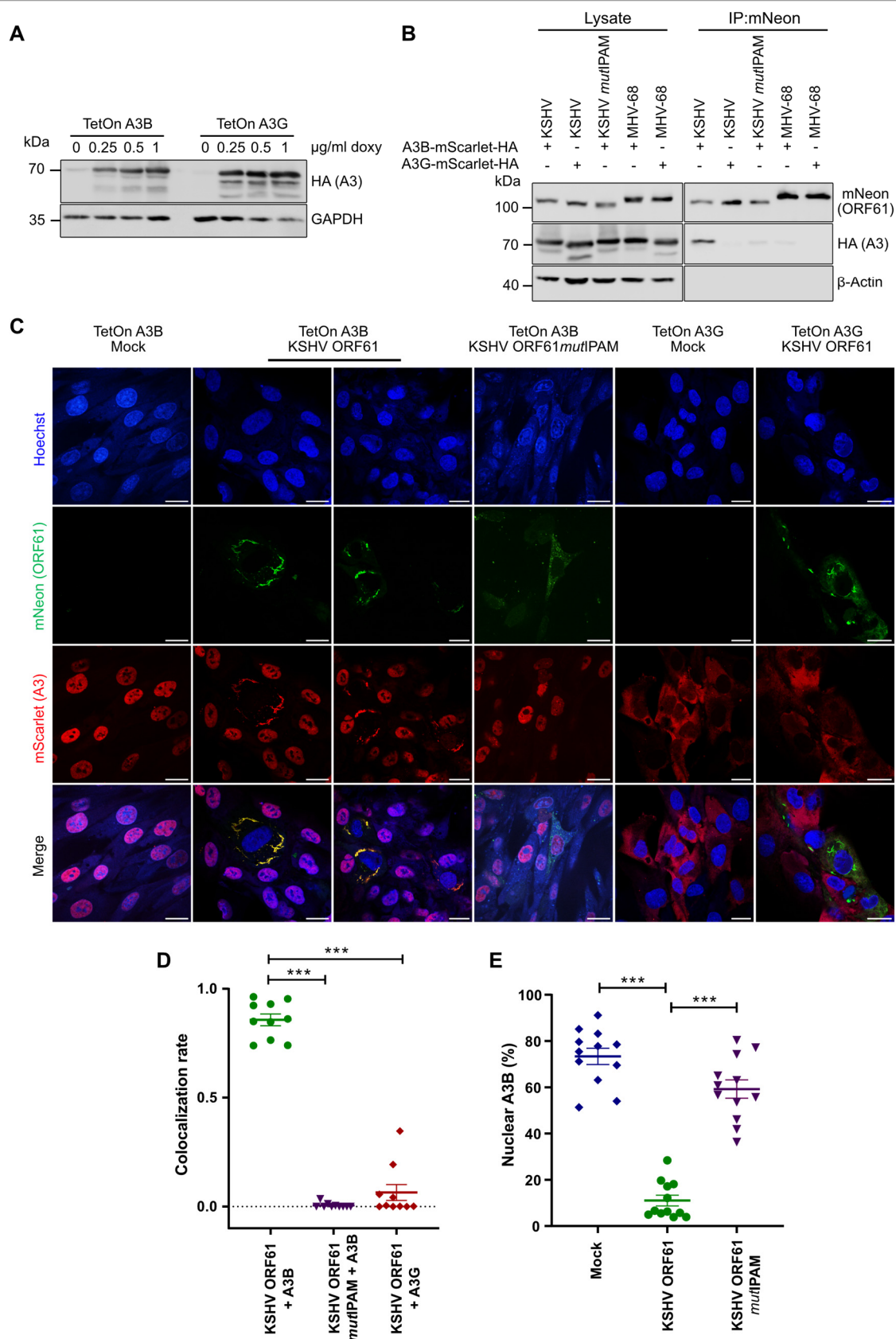
Figure 16. KSHV ORF61 binds and relocalizes A3B in an IPAM-dependent manner in infected cells. (A) Immunoblot of the Tet-inducible expression of mScarlet-HA-tagged A3B and A3G in stably transduced RPE-1 cells 24 h after treatment with varying concentrations of doxycycline. (B) TetOn A3B and A3G RPE-1 cells were infected with either KSHV mNeon-ORF61, KSHV mNeon-ORF61*mut*IPAM (MOI 0.1 TCID$_{50}$/cell) or MHV-68 ORF61-mNeon (MOI 5 TCID$_{50}$/cell). A3 expression was induced 16 h later with 1 µg/ml doxycycline and cell lysates were used for mNeon pulldown at 40 hpi. Co-precipitating proteins were detected by immunoblot. (C) TetOn A3B and A3G RPE-1 cells infected with KSHV mNeon-ORF61 or KSHV mNeon-ORF61*mut*IPAM. A3

expression was induced at 16 hpi with 1 µg/ml doxycycline. At 48 hpi, cells were fixed, nuclei were counterstained with Hoechst 33342, and fluorescence images were acquired by cLSM. Scale bar, 20 µm. (D) Co-localization was quantified by calculating Pearson's correlation coefficient for ORF61 and A3 signals using Z-stacks acquired for each condition (n = 10). Mean values ± SEM are shown. Significance was calculated using an unpaired Student's t-test. ***, P <0.001. (E) The percentage of nuclear A3B fluorescence intensity was determined by dividing the nuclear by the total A3B intensity for each infected cell (n = 12). Mean values ± SEM are shown. Significance was calculated using an unpaired Student's t-test. ***, P <0.001. Quantitative image analysis (panels D and E) performed by Enrico Caragliano (CSSB/LIV).

5.10 KSHV ORF61 is crucial for efficient replication and protection from A3B-mediated genome editing

Upon observing that the IPAM is a prerequisite for KSHV and MHV-68 ORF61 aggregation (Figs. 6A and 7B) and, in the case of KSHV ORF61, for A3B relocalization and sequestration (Figs. 13, 16C and 16E), the importance of both processes for viral replication was investigated. To this end, multistep replication kinetics of KSHV and MHV-68 carrying an intact or a mutated IPAM were determined by infecting cells at a low MOI in triplicate and quantifying the amount of infectious virus in the supernatant at different time points. As shown in Fig. 17A, MHV ORF61*mut*IPAM viral titers in MEF cells were similar to those of the parental virus, suggesting that the ability to form ORF61 aggregates was not required for efficient MHV-68 replication in these cells. In contrast, KSHV showed a discernible replication defect upon IPAM disruption in TetOn A3B RPE-1 cells with a nearly 100-fold titer reduction compared to the parental virus (Fig. 17B). Interestingly, the IPAM mutant replicated to reduced titers even without A3B induction but displayed a more pronounced replication defect upon A3B overexpression. These results suggested that ORF61 aggregation has an impact on KSHV replication and that the observed replication defect can be partially attributed to impaired A3B sequestration.

Next, differential DNA denaturation PCR (3D-PCR) was applied to test if the inability of KSHV ORF61*mut*IPAM to sequester A3B renders the virus more susceptible to A3B-mediated deamination. 3D-PCR allows differential amplification of template DNA based on the GC content by making use of the lower temperature required to denaturate AT-rich templates, such as viral genome fragments deaminated by APOBEC3 proteins (132). Since A3 proteins deaminate ssDNA cytosine residues to uracil, which corresponds to a G-to-A mutation on the complementary strand (70), the GC content of edited sequences is reduced, allowing their amplification by 3D-PCR at lower denaturation temperatures.

TetOn A3B RPE-1 cells were infected with KSHV mNeon-ORF61 or ORF61*mut*IPAM with or without doxycycline-induced A3B overexpression. Viral DNA was extracted from supernatants on day 7 post-infection, and a previously described nested-PCR approach (133) was adapted to amplify a fragment of the viral immediate-early gene ORF45, which contains several 5'-TC-dinucleotides suitable for A3B-mediated deamination (72). Following a first amplification of a 577-bp-fragment of ORF45, equal amounts of the resulting PCR products served as a template for a second-round PCR amplification of a smaller 411 bp fragment using a denaturation temperature gradient from 84.4 to

86°C. As shown in Fig. 17C, the ORF45 fragment of KSHV ORF61*mut*IPAM was amplified at lower denaturation temperatures compared to that of the parental virus (left panel), corresponding to an increased accumulation of deamination events upon IPAM disruption. Doxycycline-induced A3B overexpression led to a shift in the minimal denaturation temperature for both viruses (right panel), suggesting that genome deamination by overexpressed A3B was incompletely counteracted by ORF61 in infected RPE-1 cells. These results confirmed that the sequestration of A3B in filamentous cytoplasmic ORF61 aggregates serves to protect the KSHV genome from A3B-mediated genome editing.
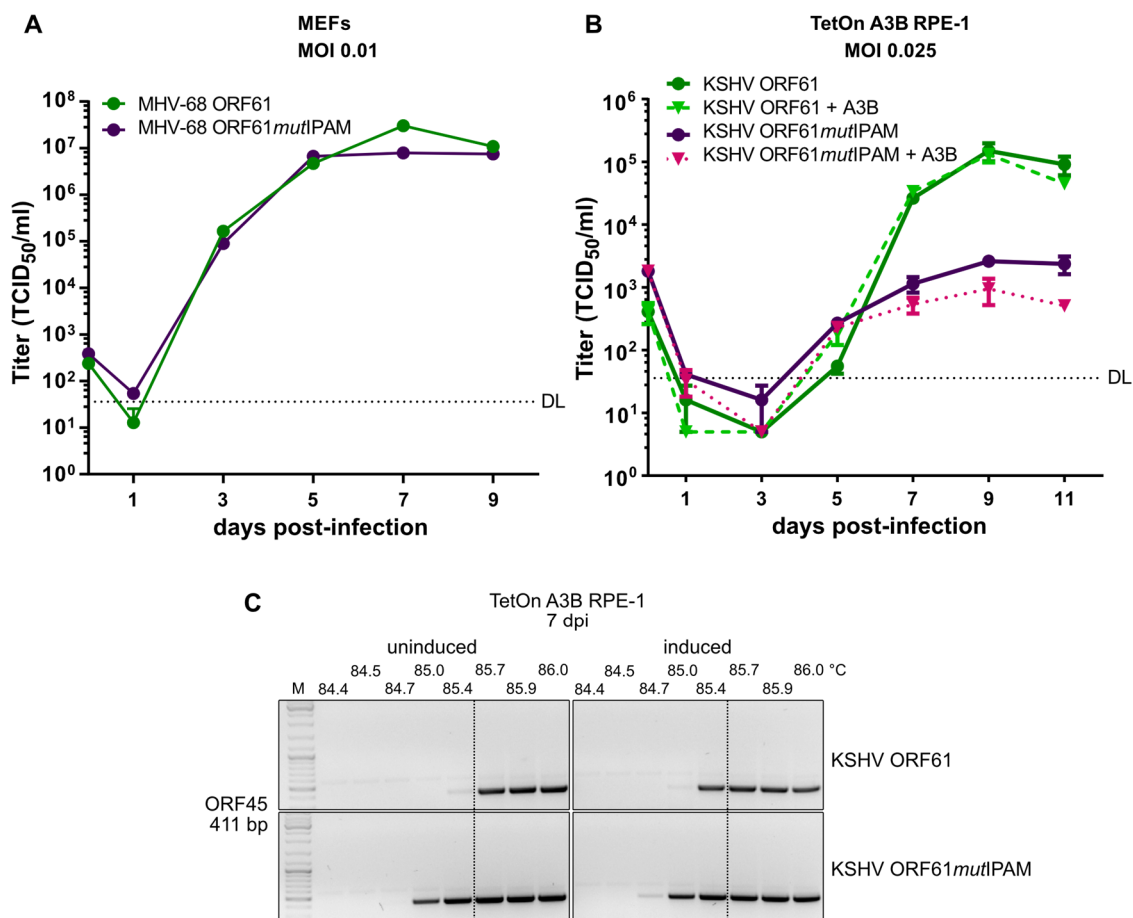
Figure 17. Requirement of the KSHV ORF61 IPAM for efficient replication and protection from A3B-mediated genome editing. (A) Multistep MHV-68 replication kinetics. MEF cells were infected with MHV-68 ORF61-FLAG or ORF61*mut*IPAM-FLAG at MOI 0.01 TCID$_{50}$/cell. Viral titers in the supernatants were determined. Mean values ± SEM of triplicates are shown. DL, detection limit. (B) Multistep KSHV replication kinetics. TetOn A3B RPE-1 cells were infected with either KSHV mNeon-ORF61 or mNeon-ORF61*mut*IPAM at MOI 0.025 TCID$_{50}$/cell. At 4 hpi, the cells were treated with 1 μg/ml doxycycline to induce A3B expression or left untreated. Viral titers were determined in the supernatants. Mean values ± SEM of triplicates are shown. DL, detection limit. (C) Differential DNA denaturation PCR (3D-PCR) of KSHV mNeon-ORF61 and mNeon-ORF61*mut*IPAM with (induced) or without (uninduced) A3B overexpression in TetOn A3B RPE-1 cells. DNA extracted from supernatants at 7 dpi was used to PCR-amplify a fragment of the viral ORF45 by a nested approach. A PCR with a denaturation temperature gradient was used to determine the lowest denaturation temperature that allowed amplification. The dotted lines indicate the lowest denaturation temperature for the ORF45 fragment of KSHV mNeon-ORF61 without A3B induction. M, DNA size marker.

5.11 LC-MS/MS screen to identify cellular proteins present in MHV-68 ORF61 aggregates

Despite the obvious structural similarities between MHV-68 and KSHV R1 protein aggregates (Figs. 6 and 7), MHV-68 ORF61 was shown to differ from its KSHV homolog in terms of cellular interactors. It did not bind the KSHV ORF61 target protein A3B nor did it sequester mA3 or the related mA1 (Figs. 14 and 16B). However, it seemed likely that the distinctively shaped ORF61 aggregates would be involved in sequestering cellular restriction factors or immune modulators. In an attempt to identify proteins accumulating in MHV-68 ORF61 aggregates, a liquid chromatography-tandem mass spectrometry (LC-MS/MS)-based screen was carried out (in collaboration with Bente Siebels, Antonia Gocke, and Hartmut Schlüter, Core Facility Mass Spectrometric Proteomics, University Medical Center Hamburg-Eppendorf). As MHV-68 ORF61*mut*IPAM does not form aggregates but instead remains soluble throughout infection (Figs. 7B and 8B), it was hypothesized that the sequestered ORF61 target proteins would be enriched in the insoluble fraction of ORF61-infected cell lysates compared to ORF61*mut*IPAM-infected lysates. The abundance of the remaining insoluble cellular material would be comparable between the samples, and it could therefore be excluded from the analysis as background.

To test this approach, MEF cells were infected with either MHV-68 ORF61- or ORF61*mut*IPAM-FLAG at MOI 3 $TCID_{50}$/cell in five replicates. At 24 hpi, cells were lysed in a mild lysis buffer and the soluble and insoluble fractions separated by centrifugation. The detergent-insoluble cell pellets were collected in SDS-PAGE sample buffer, sonicated to improve dissolution, boiled at 95°C and submitted to LC-MS/MS analysis (Fig. 18A). The log_2-transformed and normalized protein abundances in the insoluble fractions of MHV-68 ORF61-infected cells were compared to those in ORF61*mut*IPAM-infected cells. To identify statistically significant differences, the Student's *t*-test with Benjamini-Hochberg false discovery rate (FDR)-correction was applied on proteins found in at least 30% of all samples (1455 proteins). After defining a log_2-fold change ≥ 1 and a *P* value ≤ 0.05 as cut-offs for significance, a total of 120 proteins were identified as being enriched in the insoluble fraction of MHV-68 ORF61-infected cells compared to ORF61*mut*IPAM-infected cells (Fig. 18B). The presence of ORF61 itself among the most enriched proteins served as a technical validation of the approach.

To verify a possible sequestration by ORF61, the genes encoding some of the most abundant proteins were cloned into expression plasmids. U2OS cells were then transfected with these HA-tagged constructs either alone or together with ORF61-FLAG, the proteins were visualized by indirect immunofluorescence, and the cells imaged by cLSM. Among the proteins selected for a first round of testing were the E3 ubiquitin ligase UHRF1, the most abundant protein of the screen (Fig. 18B), as well as the ubiquitin-binding protein Tax1-binding protein 1 (TAX1BP1) and bone marrow stromal antigen 2 (BST2/tetherin), an antiviral factor that has been shown to inhibit the release of several enveloped viruses by tethering the viral particles to the cell membrane (134-136). As seen in Fig. 18C, none of these proteins co-localized directly with the ORF61 FLAG-signal. TAX1BP1 dots and BST2

condensates localized adjacent to the ORF61 filaments, thus suggesting a possible interaction, but with no evidence of sequestration, these findings were not investigated further.
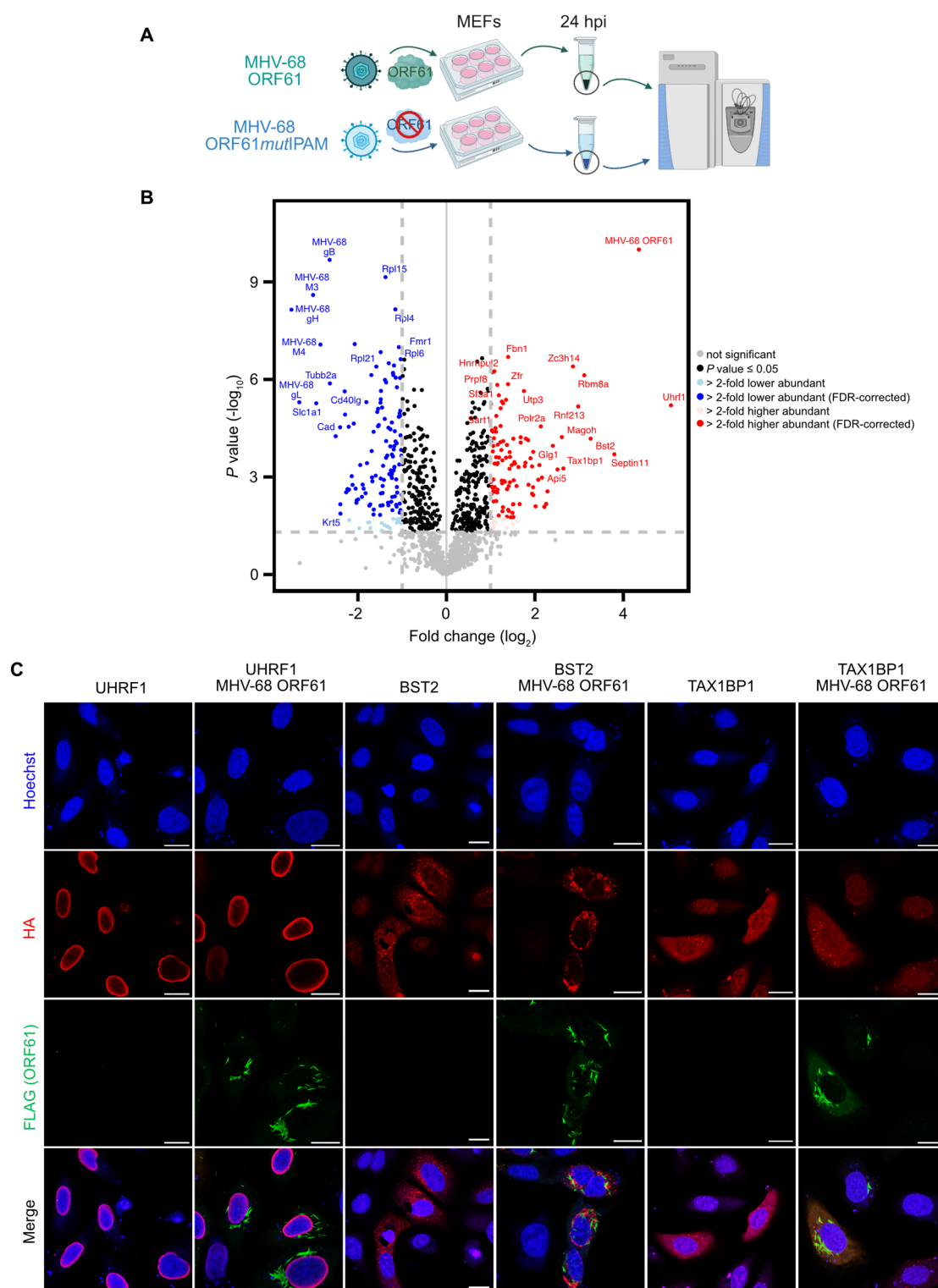
Figure 18. LC-MS/MS screen to identify proteins sequestered in MHV-68 ORF61 aggregates. (A) Experimental setup of the LC-MS/MS screen. MEF cells were infected with either MHV-68 ORF61- or ORF61*mut*IPAM-FLAG at MOI 3 $TCID_{50}$/cell in five replicates. At 24 hpi, cells were lysed and lysates separated into detergent-soluble and -insoluble fractions. The insoluble pellets were collected in SDS-PAGE sample buffer, sonicated, boiled, and submitted to LC-MS/MS analysis. Image created with BioRender.com. (B) Volcano plot representing the pairwise, two-tailed Stundent's *t*-test results comparing protein abundances in the insoluble

fractions of MHV-68 ORF61- and ORF61*mut*IPAM-infected cells with and without false discovery rate (FDR) correction by Benjamini-Hochberg. Cut-offs for significance were set to a $\log_2$-fold change ≥ 1 and a *P* value ≤ 0.05 and are indicated by the dashed lines. Data generated and statistical analysis performed by Bente Siebels, Antonia Gocke, and Hartmut Schlüter (Core Facility Mass Spectrometric Proteomics, University Medical Center Hamburg-Eppendorf). (C) U2OS cells were transfected with plasmids expressing HA-tagged mouse UHRF1, BST2 or TAX1BP1 and MHV-68 ORF61-FLAG. Cells were fixed, immunostained with anti-HA and anti-FLAG antibodies and counterstained with Hoechst 33342. Fluorescence images were acquired by cLSM. Scale bar, 20 µm.

5.12 RNF213 localizes to rhadinovirus R1 aggregates in transfected cells

Among the five most abundant proteins detected in the insoluble fraction of MHV-68 ORF61-infected cells by LC-MS/MS, RING finger protein 213 (RNF213) was the most intriguing interactor candidate. RNF213 (also termed mysterin in humans) is a large, interferon-inducible cytoplasmic protein of approximately 590 kDa in size. RNF213 harbors both a RING and a RZ finger ubiquitin ligase domain at its C-terminus, and mutations around and within the RING finger domain have been associated with the onset of Moyamoya disease, a rare cerebrovascular disorder mainly affecting the East Asian population (137, 138). In addition to its antimicrobial role involving ubiquitination of intracellular bacteria, such as *Salmonella* and *Listeria monocytogenes* (139, 140), RNF213 functions as a restriction factor for γ-herpesviruses. It has been shown to polyubiquitinate the RTA lytic switch protein of both KSHV and MHV-68 and to target it for degradation through the ubiquitin-proteasome system, thereby restricting *de novo* infection and lytic reactivation (141). It would therefore be advantageous for the virus to be able to efficiently neutralize RNF213, e.g., by sequestering it in aggregates. To test if RNF213 truly accumulates in KSHV and MHV-68 ORF61 aggregates, HEK-293A cells were transfected with fluorescently tagged mouse or human RNF213 expression plasmids and either MHV-68 ORF61-pmCherry or KSHV ORF61-pEGFP, respectively. As shown by the cLSM images in Figs. 19A and 19B, the RNF213 signal did indeed co-localize with the ORF61 aggregates, suggesting that the two proteins might interact. Although these preliminary data are encouraging, additional experiments are required to verify the interaction and to characterize its functional consequences in the context of infection.
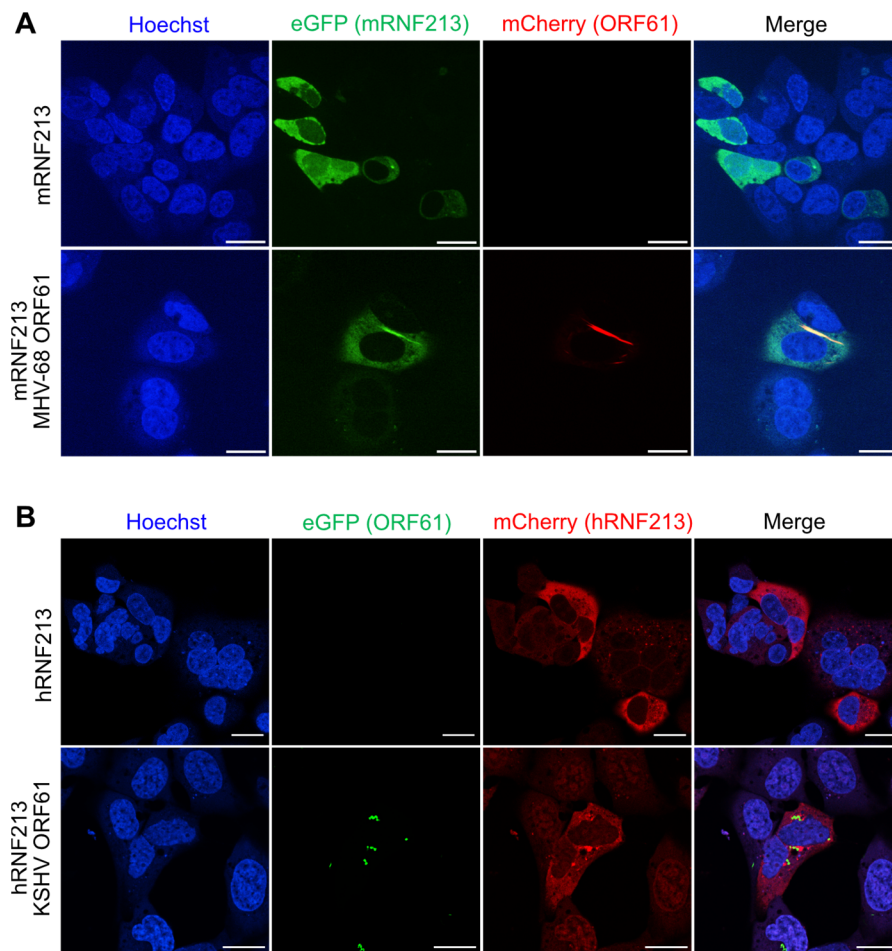
Figure 19. RNF213 localizes to ORF61 aggregates in transfected cells. HEK-293A cells were transfected with plasmids expressing either (A) eGFP-mRNF213 and MHV-68 ORF61-mCherry or (B) mCherry-hRNF213 and KSHV ORF61-eGFP. After 24 h, cells were fixed, and nuclei were counterstained with Hoechst 33342. Fluorescence images were acquired by cLSM. Scale bar, 20 μm.

6. Discussion

The present work set out to elucidate the role of KSHV and MHV-68 ORF61 in counteracting the host immune response, and whether the underlying mechanism involves IPAM-mediated aggregation and subsequent aggregate degradation by autophagy. The results show that both proteins form distinct, filamentous aggregates in infected cells. The ORF61 aggregates are not substantially degraded by autophagy, but their sequestration function is involved in subverting host defenses, as illustrated by KSHV ORF61 that relocalizes A3B out of the nucleus to cytoplasmic aggregates in an IPAM-dependent manner. An IPAM mutant KSHV, that fails to form ORF61 filaments and to alter A3B localization, is more susceptible to genome deamination, suggesting that A3B sequestration serves to protect the replicating viral genome from detrimental mutations.

6.1 KSHV and MHV-68 R1 proteins display a distinct, filamentous morphology

R1 proteins of the β-herpesvirus MCMV and the α-herpesvirus HSV-1 have been shown to accumulate in the insoluble fraction of infected cell lysates and to form dot-like aggregates in the cytoplasm of infected cells. In electron micrographs, MCMV M45 aggregates appear as amorphous, electron-dense condensates (120). The present work structurally characterized the R1 protein ORF61 of the γ-herpesviruses KSHV and MHV-68. Similar to M45, ORF61 becomes increasingly insoluble in the course of infection (Fig. 8) and does not recover fluorescence after photobleaching (Fig. 10), a property indicative of a solid structure. As shown by CLEM analysis of infected cells, KSHV and MHV-68 R1 proteins are both composed of filament bundles that measure up to several microns in length (Fig. 11). This striking morphology is in sharp contrast to the small, globular aggregates formed by their MCMV and HSV-1 homologs (120). Detailed structural studies of the EBV homolog BORF2 in an infectious context are lacking, but the structure of purified BORF2 bound to the A3B catalytic C-terminal domain (ctd) has been solved by cryo-EM (124). Intriguingly, transfected BORF2 often forms large, elongated condensates that resemble the filamentous ORF61 aggregates, and an *in silico* structural model of KSHV ORF61 overlays well with the BORF2 cryo-EM structure (125), collectively suggesting conservation of the R1 protein structure within the γ-subfamily. Admittedly, the condensates formed by R1 proteins of other related primate γ-herpesviruses upon overexpression do not acquire filamentous morphology (125), but rather resemble the more globular KSHV ORF61 aggregates observed in transfected cells (Fig. 13), thus implying a key role for a viral factor or a virus-induced process in filament formation.

As the BORF2 dimerization interface in the BORF2-A3Bctd complex differs from the predicted canonical R1 dimerization interface, Shaban *et al.* conclude that BORF2 exists in two dimeric complexes in cells: as a canonical dimer forming part of the enzymatically active, heterotetrameric RNR, and as a non-canonical dimer giving rise to large, A3B-binding oligomers. In the BORF2-A3Bctd complex, BORF2 dimerization is mediated by electrostatic interactions between the N-terminal

residues E8, D26 and R39. R39 of each monomer thereby interacts with E8 of the same monomer and with D26 of the opposing monomer (124). These residues are only partially conserved in KSHV and MHV-68 ORF61, but both ORF61 proteins contain similarly charged residues in the vicinity of these positions, raising the possibility that they similarly dimerize at a non-canonical, N-terminal interface. In contrast, M45 and ICP6, that do not form filamentous aggregates, lack charged residues at the corresponding positions and most likely do not share the dimerization interface of γ-herpesvirus R1 proteins.

6.2 Cellular processing of KSHV and MHV-68 R1 proteins

The dot-like MCMV M45 and HSV-1 ICP6 aggregates are targeted to autophagosomes for degradation by selective autophagy (119, 120) (Fig. 5). In contrast, autophagy does not seem to play a key role in the turnover of KSHV and MHV-68 ORF61 proteins, since they do not accumulate in the insoluble fraction upon pharmacologic or genetic inhibition of autophagosome formation (Fig. 9). The large, filamentous ORF61 aggregates, that appear later during infection (Figs. 6 and 7), are potentially impervious to autophagic degradation due to their size and shape. The dot-like ORF61 condensates, that rather resemble M45 and ICP6 aggregates and are observed before filament formation (Figs. 6 and 7), might be more suitable autophagy targets, but perhaps grow and nucleate ORF61 filament formation too rapidly, thereby exceeding the degradation capacity of the cell. As the autophagy cargo receptors preferably bind ubiquitinated cargo (45), it is also conceivable that the ubiquitination status or other post-translational modifications might make ORF61 aggregates less accessible to the autophagy machinery. As for other degradation pathways, the sheer size of the ORF61 filaments is likely to render them resistant to degradation by the ubiquitin-proteasome system or other pathways that only process monomeric, soluble proteins.

6.3 Herpesvirus-induced filament formation

The present study is the first to report the formation of filamentous aggregates by the KSHV and MHV-68 ORF61 proteins in virus-infected cells. The ORF61 aggregate architecture, consisting of filament bundles that measure up to several hundred nanometers in width and several microns in length (Fig. 11), represents a unique morphology among herpesviral proteins. However, smaller herpesviral filaments have been previously described.

The HSV-1 ssDNA-binding protein ICP8, that is required for prereplication site and replication compartment (RC) formation in infected cell nuclei (142, 143), has been shown to form 10-20 nm-wide filaments *in vitro* (144, 145). Interestingly, these ICP8 filaments seem to be indispensable for the assembly of HSV-1 RCs. ICP8 mutants that have lost the ability to form filaments are unable to nucleate RC formation, despite retaining all essential interactions with other viral replication proteins. It is hypothesized that the ICP8 filaments contribute to the assembly of HSV-1 RCs by providing a scaffold onto which other necessary viral and cellular proteins can be recruited (146).

Since the ORF61 aggregates are exclusively cytoplasmic, they are unlikely to contribute to RC formation. Due to their large size and dispersed distribution in the cytoplasm, it seems equally unlikely that they serve as a scaffold to locally concentrate cellular or viral factors.

In addition to filament-forming viral proteins, herpesvirus infection is known to cause a profound reorganization of the cellular cytoskeleton, thereby giving rise to filamentous cellular structures. The viral US3 kinase of the porcine α-herpesvirus pseudorabies virus (PRV) induces the formation of actin- and microtubule-containing cell projections that enhance the intercellular spread of viral particles shielding them from the effect of neutralizing antibodies (147). Furthermore, α-herpesvirus infection leads to the accumulation of actin filaments in infected nuclei. These filaments, that are observed in PRV- and HSV-1-infected neurons and to a lesser extent in epithelial cells, facilitate the formation of viral capsid assembly sites. Capsids also seem to migrate along the nuclear actin filaments by myosin-mediated transport to reach the nuclear envelope for budding (148).

Although neither F-actin nor the intermediate filament vimentin was detected in ORF61 aggregates by immunofluorescence (Fig. 12), the involvement of other cellular cytoskeleton constituents in ORF61 filament formation cannot be excluded. The filament bundles might also be resistant to staining, albeit not inherently impermeable, as demonstrated by the successful immunofluorescence staining of the ORF61-FLAG fusion protein in infected cells (Fig. 7B).

6.4 ORF61-like filaments in RNA virus infection

The present study provides the first evidence that KSHV ORF61 forms prominent, filamentous aggregates in infected cells to sequester cellular target proteins (Figs. 16B and 16C) and additionally implies a similar function for the homologous MHV-68 ORF61 (Fig. 19A). Intriguingly, morphologically similar filament bundles have been previously observed in the nuclei of cells infected by the mosquito-borne RNA virus Rift Valley fever virus (RVFV). These nuclear filaments are formed by the RVFV non-structural small (NSs) protein (149), and when analyzed by EM, they assemble to 0.5 µm wide bundles that consist of thinner parallel fibrils (150), strikingly resembling KSHV and MHV-68 ORF61 aggregates (Fig. 11). Similar to ORF61, RVFV NSs filaments seem to exert a sequestration function to subvert the host antiviral response. Subunits of transcription factor II H, that is required for transcription initiation by RNA Pol II, are present in the nuclear NSs filaments (151). Furthermore, a subunit of a chromatin-remodeling corepressor complex regulating transcriptional activation of the interferon-β (IFN-β) promoter interacts with NSs filaments, resulting in sequestration of the complex in the IFN-β promoter region and subsequent repression of *IFN-β* gene expression (152). Thus, unrelated viral proteins of RNA and DNA viruses form very similar, prominent filaments to counteract cellular restriction factors and immune mediators.

6.5 Importance of the IPAM for herpesviral R1 protein structure

Despite the apparent morphological differences between herpesvirus R1 protein aggregates from different subfamilies, the conserved C-terminal Induced Protein Aggregation Motif (IPAM) seems to be a key structural determinant shared by these proteins. In MCMV and HSV-1, the IPAM mediates both self-interaction of the R1 proteins as well as their interaction with the cellular target proteins. Consequently, IPAM disruption renders MCMV M45 and HSV-1 ICP6 unable to oligomerize and to form dot-like aggregates (120). Similarly, an IPAM mutant EBV BORF2 loses its ability to form large condensates in transfected cells (114). Reminiscent of this phenotype, the present study shows that an intact IPAM is required for KSHV (Fig. 6A) and MHV-68 (Fig. 7B) ORF61 filament formation, as well as for APOBEC3B sequestration and relocalization by KSHV ORF61 (Figs. 16B and 16C). Although transfection experiments did not permit definitive conclusions regarding the role of the IPAM in ORF61 self-interaction (data not shown), the findings presented here collectively underline the importance of the IPAM for the structural architecture of herpesvirus R1 proteins independent of the subfamily.

Among the viral R1 proteins, only the structure of BORF2 has been determined. Cryo-EM analysis of the purified BORF2-A3Bctd complex revealed a large binding interface between the two proteins and identified the BORF2 residues L133, Y134, Y481 and R484 as crucial for the interaction. A single amino acid substitution in each of the positions was sufficient to abolish the interaction (124). Considering that KSHV ORF61 only shares around 42% primary amino acid identity with BORF2 (125), it is not surprising that only the first two of these residues are conserved in ORF61. However, as the predicted structure of KSHV ORF61 displays a high degree of similarity to the cryo-EM structure of BORF2 bound to A3Bctd (125), both γ-herpesvirus R1 proteins probably bind A3B in a similar manner. HSV-1 ICP6, that also binds and relocalizes A3B (126) but forms globular aggregates instead of filaments (120), does not share any of the aforementioned A3B-interacting residues, suggesting that it binds A3B by a different mechanism.

Although the aggregation of MCMV, HSV-1, KSHV, and MHV-68 R1 proteins is an IPAM-dependent process ((120) and this study), a property that also seems to be conserved in BORF2 (114), the IPAM residues do not contribute to the formation of the non-canonical dimerization interface in the BORF2 cryo-EM structure, but are instead buried within the structure. A possible explanation is that the IPAM forms part of the structural core of the R1 proteins and is therefore only indirectly involved in dimerization and subsequent higher-order oligomerization. In line with this, the observed loss of target protein binding by IPAM mutant R1 proteins ((120) and this study) likely stems from a compromised overall structure rather than alterations at the binding interface.

6.6 Biological relevance of IPAM-dependent A3B relocalization by KSHV ORF61

As shown in the present work, the KSHV R1 protein ORF61 binds A3B and relocalizes it out of the nucleus to filamentous, cytoplasmic aggregates in an IPAM-dependent manner during lytic infection. Disruption of the IPAM by two alanine substitutions (PFVDQ to PFVAA) not only abolishes A3B binding and redistribution (Figs. 16B and 16C) but also impairs KSHV replication in RPE-1 human epithelial cells (Fig. 17B). Although the temporal kinetics are not affected, the peak titers of KSHV ORF61*mut*IPAM are considerably reduced compared to the parental virus. Doxycycline-mediated A3B overexpression further restricts ORF61*mut*IPAM replication but has no impact on the parental virus. The observed increased deamination of the ORF61*mut*IPAM viral genome upon A3B overexpression (Fig. 17C) suggests that the incapability of the mutant to remove the mutagenic A3B from the nucleus or to inhibit its deaminase activity is at least partially responsible for the observed replication defect. However, as the IPAM lies in the vicinity of the C-terminal R1 catalytic residues (Fig. 4A), a compromised RNR function could also contribute to the observed impaired replication. In support of this hypothesis, the replication defect of the IPAM mutant only becomes apparent on day 7 (Fig. 17B) when the cells have most likely entered quiescence due to contact inhibition, resulting in low cellular dNTP pools. A KSHV ORF61 mutant unable to redistribute A3B while retaining all other protein functions would allow distinction between A3B-dependent and -independent effects. It would also be worthwhile to test whether knocking out A3B could alleviate or reverse the increased genome deamination and reduced replication of KSHV ORF61*mut*IPAM.

The observation that KSHV with an intact IPAM is also susceptible to deamination upon A3B induction, albeit to a lesser extent than the mutant (Fig. 17C), suggests that the increased deamination activity resulting from A3B overexpression likely overwhelms the counteracting capacity of the virus. However, since A3B overexpression does not lead to reduced replication of the KSHV ORF61 virus (Fig. 17B), this degree of genome deamination appears to fall short of a critical threshold detrimental for viral replication.

6.7 The function of MHV-68 ORF61 filaments remains enigmatic

The IPAM-dependent MHV-68 ORF61 aggregates observed in infected cells (Fig. 7B) closely resemble those formed by their KSHV homolog (Fig. 6A) and are similarly composed of filament bundles (Fig. 11). However, in contrast to the IPAM mutant KSHV, MHV-68 ORF61*mut*IPAM replicates to titers comparable to the parental virus (Fig. 17A). On the one hand, this suggests that IPAM disruption does not affect MHV-68 RNR function, although the effect might be negligible in rapidly dividing immortalized cells, such as MEFs, and more pronounced in another cell type. On the other hand, the efficient replication of the ORF61*mut*IPAM virus suggests that in case MHV-68 ORF61 aggregates share the ability of many of their homologs to counteract cellular targets, this function is either generally redundant, i.e., shared by another viral protein, only relevant *in vivo*, or cell type-

dependent. Maybe the target is only present at low levels or even completely absent in fibroblasts, which were the cell type used to determine the replication kinetics.

Despite the morphological similarities with its A3B-interacting KSHV counterpart, MHV-68 ORF61 does not sequester or alter the localization of A3B or the murine A3 protein (mA3) (Figs. 14 and 16B). Since mA3 is a cytoplasmic protein, it does not pose an imminent threat to the replicating viral genome and, accordingly, does not restrict MHV-68 replication *in vivo* (153, 154). Interestingly, human A3A and A3B have been shown to impair MHV-68 replication when co-transfected with the infectious viral genome, but the restriction is lost when the cells are infected using intact viral particles. This suggests that A3A and A3B, although present in the nucleus (77), either do not have access to viral ssDNA substrate in RCs of infected cells due to compartmental separation, or are antagonized by a viral protein other than ORF61, such as a structural virion component (153).

It seems unlikely that MHV-68 ORF61 forms such prominent aggregates in infected cells without using them to sequester cellular immune mediators or antiviral factors. Apart from a single study postulating a possible link between MHV-68 ORF61 and an altered track-like morphology of the antiviral promyelocytic leukemia nuclear bodies (155), no cellular targets or interaction partners of the MHV-68 R1 protein have been described. Thus, an LC-MS/MS interactor screen was performed as a part of this study to identify ORF61 binding partner candidates. Since attempts to immunoprecipitate insoluble ORF61 were unsuccessful, an experimental setup without an enrichment step was employed (Fig. 18A). The drawback of this approach is that it detects all proteins that are more abundant in the MHV-68 ORF61-infected insoluble cell fraction compared to the ORF61*mut*IPAM-infected control, independent of a direct interaction with ORF61. Strikingly, several of the most abundant proteins identified by the screen are either associated with RNA metabolism, e.g., RNA-binding protein 8A (RBM8A), Zinc finger CCCH domain-containing protein 14 (ZC3H14), and Protein mago nashi homolog (MAGOH), or with the ubiquitin system, e.g., the E3 ubiquitin ligases UHRF1 and RNF213, and the ubiquitin adaptor protein Tax1-binding protein 1 (TAX1BP1) (Fig. 18B). While components of the spliceosome were not intuitive sequestration targets for ORF61, the focus was placed on the ubiquitin system proteins and the known antiviral factor bone marrow stromal antigen 2 (BST2)/tetherin (134). Despite being the most abundant protein identified in the MS screen, the ubiquitin ligase UHRF1 was solely detected in the nucleus and did not exhibit relocalization upon co-transfection with MHV-68 ORF61 (Fig. 18C), suggesting that it is not sequestered in ORF61 aggregates. It is also conceivable that the lack of additional viral factors in transfected cells precludes sequestration, but this would distinguish MHV-68 from its KSHV homolog which alone is sufficient to relocalize and sequester nuclear A3B (Fig. 13). Similar to UHRF1, none of the other tested interactor candidates localized to the MHV-68 ORF61 aggregates in co-transfection experiments (Fig. 18C), except for RNF213 (Fig. 19A).

As an inhibitor of KSHV and MHV-68 lytic replication (141), RNF213 is an intriguing target candidate for ORF61-mediated sequestration and neutralization, and, indeed, it seems to be present in KSHV

and MHV-68 ORF61 aggregates in transfected cells (Fig. 19). Another explanation for the observed co-localization is that, rather than being selectively targeted by ORF61, RNF213 instead ubiquitinates or otherwise targets ORF61 aggregates, in analogy to its mode of action against intracellular pathogens, such as *Salmonella* (139) and *Toxoplasma gondii* (156). In support of this hypothesis, the ubiquitin-binding protein TAX1BP1 that RNF213 recruits to the ubiquitin-decorated *T. gondii* parasitophorous vacuoles (156), is among the top hits in the MHV-68 ORF61 interactor screen (Fig. 18B) and is found in the vicinity of ORF61 aggregates in transfected cells (Fig. 18C). Further investigation is required to elucidate whether the multifunctional RNF213 targets ORF61 or, conversely, whether KSHV and MHV-68 have repurposed ORF61 to neutralize the antiviral effect of RNF213.

6.8 Concluding remarks

Despite differences in morphological features and cellular processing, herpesviral R1 proteins across all subfamilies share the property of aggregation to counteract distinct, albeit partially overlapping sets of cellular target proteins. MCMV M45 sequesters RIPK1 and NEMO in cytoplasmic IPAM-dependent aggregates and targets them for subsequent degradation by selective autophagy. HSV-1 ICP6 similarly binds and targets RIPK1 for autophagic degradation in an IPAM-dependent manner. In addition, ICP6 binds the cytosine deaminase A3B and relocalizes it out of the nucleus to the cytoplasmic compartment. Mutagenic A3B is also counteracted by EBV BORF2, which inhibits its deaminase activity and redistributes it from the nucleus to cytoplasmic condensates. As shown in the present work, KSHV ORF61 utilizes a similar strategy and relocalizes A3B to the cytoplasm in an IPAM-dependent manner. While it is probable that the observed MHV-68 ORF61 aggregates likewise aid in sequestering and neutralizing target proteins, the identity of these targets and of additional proteins potentially present in other herpesviral R1 aggregates remains to be determined.

7. Materials

7.1 Cells

Name	Description	Reference
ARPE-19	Spontaneously immortalized human retinal pigment epithelial cells	ATCC (CRL-2302)
TIME	Human telomerase reverse transcriptase (hTERT)-immortalized human microvascular endothelial cells	(157)
MEF	Mouse embryonic fibroblasts immortalized with the SV40 large T antigen	Riken BRC (RCB2710)
10.1	Spontaneously immortalized embryonic fibroblasts isolated from BALB/c mice, defect in p53	(158)
NIH/3T3	Spontaneously immortalized embryonic fibroblasts isolated from NIH/Swiss mice	ATCC (CRL-1658)
$Atg5^{-/-}$ MEF	$Atg5$ knockout mouse embryonic fibroblasts immortalized with the SV40 large T antigen	Riken BRC (RCB2711)
U2OS	Human osteosarcoma-derived cells with epithelial morphology	ATCC (HTB-96)
HFF	Life-extended human foreskin fibroblasts	(159)
HEK-293A	Human embryonic kidney epithelial cells immortalized with hAdV5 E1A and E1B	Invitrogen
HEK-293T	Human embryonic kidney epithelial cells immortalized with the SV40 large T antigen	ATCC (CRL-11268)
RPE-1 puro	hTERT-immortalized human retinal pigment epithelial cells (ATCC CRL-4000), in which the $PuroR$ gene was knocked out using CRISPR/Cas9	E. Ostermann, unpublished data
TetOn A3B RPE-1	RPE-1 puro cells stably expressing APOBEC3B-mScarlet-HA under the control of a tetracycline responsive element (TRE) promoter	This study
TetOn A3G RPE-1	RPE-1 puro cells stably expressing APOBEC3G-mScarlet-HA under the control of a TRE promoter	This study

7.2 Viruses

Name	Description	Reference
KSHV$_{Lyt}$	Constitutively lytic, BAC16-derived KSHV BAC clone expressing RTA under the control of a cellular PGK promoter	(128)
KSHV mNeon-ORF61	KSHV$_{Lyt}$, in which the eGFP-HygroR cassette was replaced by a ZeoR cassette and mNeonGreen introduced to the N-terminus of ORF61	This study
KSHV mNeon-ORF61mutIPAM	KSHV mNeon-ORF61 with a mutated IPAM (PFVDQ to PFVAA)	This study
MHV-68 ORF61-mNeon	MHV-68 BAC pHA3 (160), in which the eGFP cassette was replaced by a ZeoR cassette and mNeonGreen introduced to the C-terminus of ORF61	This study
MHV-68 ORF61-FLAG	MHV-68 BAC pHA3 (160), in which a 3xFLAG-tag was fused C-terminally to ORF61	This study
MHV-68 ORF61mutIPAM-FLAG	MHV-68 ORF61-FLAG with a mutated IPAM (PFIDQ to PFIAA)	This study

| MCMV M45-HA | MCMV Smith pSM3fr-MCK-2fl BAC, in which M45 ORF carrying a C-terminal HA-tag was reintroduced after a deletion | (161) |

7.3 Bacteria

Name	Genotype	Growth temperature (°C)	Reference
E. coli DH10B	F– *mcrA* Δ(*mrr-hsd*RMS-*mcr*BC) φ80*lac*ZΔM15 Δ*lac*X74 *rec*A1 *end*A1 *ara*D139 Δ (*ara-leu*)7697 *gal*U *gal*K λ– *rps*L(StrR) *nup*G	37	Life Technologies
E. coli GS1783	DH10B λ *cI*857 Δ(*cro-bioA*)<>*araC*-P$_{BAD}$*I-sceI*	30	(162)

7.4 Plasmids

Name	Description	Reference
pEPkan-S	Template plasmid for *en passant* mutagenesis encoding an *I-SceI-aphAI* cassette, KanR	(163)
pcDNA3	Expression vector, AmpR	Invitrogen
pmCherry-N1	Cloning vector for creating a fusion protein with a C-terminal mCherry, KanR	Clontech Laboratories
peGFP-N1	Cloning vector for creating a fusion protein with a C-terminal eGFP, KanR	Clontech Laboratories
peGFP-C1	Cloning vector for creating a fusion protein with an N-terminal eGFP, KanR	Clontech Laboratories
pLIX402	Lentiviral vector for Tet-inducible expression, AmpR, PuroR	Addgene (#41394)
pMD2.G	Lentiviral packaging plasmid encoding the viral *env* gene, AmpR	Robert J. Lebbink, UMC Utrecht
pCMV-dR8.91	Lentiviral packaging plasmid encoding the viral *gag*, *pol* and *rev* genes, AmpR	Robert J. Lebbink, UMC Utrecht
pcDNA3-mNeonGreen-kan	Shuttle plasmid for *en passant* mutagenesis encoding mNeonGreen and an *I-SceI-aphAI* cassette	(129)
pmCherry-Nucleolin	Expression plasmid encoding human nucleolin N-terminally tagged with mCherry	(120)
pcDNA3-A3B-HA	Expression plasmid encoding APOBEC3B with a C-terminal 3xHA-tag	(164)
pcDNA3-A3G-HA	Expression plasmid encoding APOBEC3G with a C-terminal 3xHA-tag	(165)
pCMV-mA1-BE3	Expression plasmid encoding murine APOBEC1, AmpR	Addgene (#113421)
pCMV-mA3-BE3	Expression plasmid encoding murine APOBEC3, AmpR	Addgene (#113419)
pcDNA3-MCMV M45-HA	Expression plasmid encoding MCMV M45 with a C-terminal HA-tag	(117)
pcDNA3.1-hRIPK1-Flag	Expression plasmid encoding human RIPK1 with an N-terminal FLAG-tag	Addgene (#112487)
pcDNA3-mRIPK1-Flag	Expression plasmid encoding murine RIPK1 with an N-terminal FLAG-tag	Patricia M. Fliss
pcDNA3-Flag-mNEMO	Expression plasmid encoding murine NEMO with an N-terminal FLAG-tag	Patricia M. Fliss

mRNF213-pFastBAC1	Expression plasmid encoding codon-optimized murine RNF213 for expression in insect cells, AmpR	(166)
mCherry-hRNF213-3xFLAG	Expression plasmid encoding human RNF213 (mysterin) with an N-terminal mCherry- and a C-terminal 3xFLAG-tag, AmpR	(167)

The following plasmids were generated for this study:

Name	Description	Cloning approach
KSHV ORF61-pmCherry	Expression plasmid encoding KSHV ORF61 C-terminally tagged with mCherry	KSHV ORF61 sequence from KSHV$_{Lyt}$ was introduced into pmCherry-N1 using EcoRI and BamHI
MHV-68 ORF61-pmCherry	Expression plasmid encoding MHV-68 ORF61 C-terminally tagged with mCherry	MHV-68 ORF61 sequence from MHV-68 BAC pHA3 was introduced into pmCherry-N1 using BglII and SalI
pcDNA3-KSHV ORF61-FLAG	Expression plasmid encoding KSHV ORF61 with a C-terminal 3xFLAG-tag	KSHV ORF61 sequence from KSHV$_{Lyt}$ was introduced into pcDNA3 using BamHI and EcoRI. Tag sequence was included in the reverse primer
pcDNA3-KSHV ORF61*mut*IPAM-FLAG	Expression plasmid encoding KSHV ORF61 with a C-terminal 3xFLAG-tag and a mutated IPAM (PFVDQ to PAAAA)	PFVDQ to PAAAA IPAM mutation was introduced into pcDNA3-KSHV ORF61-FLAG using overlap extension PCR
pcDNA3-MHV-68 ORF61-FLAG	Expression plasmid encoding MHV-68 ORF61 with a C-terminal 3xFLAG-tag	MHV-68 ORF61 sequence from MHV-68 BAC pHA3 was introduced into pcDNA3 using EcoRV and XbaI. Tag sequence was included in the reverse primer
pcDNA3-mA1-HA	Expression plasmid encoding murine APOBEC1 with a C-terminal 3xHA-tag	mA1 sequence from pCMV-mA1-BE3 and 3xHA sequence from pcDNA3-A3B-HA were introduced into pcDNA3 using homology-based DNA assembly
pcDNA3-mA3-HA	Expression plasmid encoding murine APOBEC3 with a C-terminal 3xHA-tag	mA3 sequence from pCMV-mA3-BE3 and 3xHA sequence from pcDNA3-A3B-HA were introduced into pcDNA3 using homology-based DNA assembly
pcDNA3-KSHV ORF61-HA	Expression plasmid encoding KSHV ORF61 with a C-terminal HA-tag	KSHV ORF61 sequence from KSHV$_{Lyt}$ was introduced into pcDNA3 using BamHI and EcoRI. Tag sequence was included in the reverse primer
pcDNA3-MHV-68 ORF61-HA	Expression plasmid encoding MHV-68 ORF61 with a C-terminal HA-tag	MHV-68 ORF61 sequence from MHV-68 BAC pHA3 was introduced into pcDNA3 using EcoRV and XbaI. Tag sequence was included in the reverse primer

pLIX402-A3B-mScarlet-HA	Lentiviral expression plasmid encoding APOBEC3B fused C-terminally to mScarlet and a 3xHA-tag	A3B sequence (amplified from pcDNA3-A3B-HA), mScarlet- and 3xHA-sequences were introduced into pLIX402 using homology-based DNA assembly
pLIX402-A3G-mScarlet-HA	Lentiviral expression plasmid encoding APOBEC3G fused C-terminally to mScarlet and a 2xHA-tag	A3G sequence (amplified from pcDNA3-A3G-HA), mScarlet- and 2xHA-sequences were introduced into pLIX402 using homology-based DNA assembly
p3xHA-N1	Cloning vector for creating a fusion protein with a C-terminal 3xHA-tag, KanR	3xHA-sequence was introduced into peGFP-N1 in place of eGFP using homology-based DNA assembly
p3xHA-UHRF1	Expression plasmid encoding mouse UHRF1 C-terminally tagged with 3xHA	Mouse UHRF1 sequence (amplified from mouse cDNA) was introduced into p3xHA-N1 using EcoRI and KpnI
pcDNA3-HA-BST2	Expression plasmid encoding mouse BST2 with an N-terminal HA-tag	Mouse BST2 sequence (amplified from mouse cDNA) was introduced into pcDNA3 using KpnI and EcoRI. Tag sequence was included in the forward primer
p3xHA-TAX1BP1	Expression plasmid encoding mouse TAX1BP1 C-terminally tagged with 3xHA	Mouse TAX1BP1 sequence (amplified from mouse cDNA) was introduced into p3xHA-N1 using EcoRI and KpnI
KSHV ORF61-peGFP	Expression plasmid encoding KSHV ORF61 C-terminally tagged with eGFP	KSHV ORF61 sequence from KSHV ORF61-pmCherry was introduced into peGFP-N1 using EcoRI and BamHI
peGFP-mRNF213 5,892	Shuttle plasmid for constructing N-terminally eGFP-tagged mRNF213 for expression in mammalian cells	The first 5,892 nt of mRNF213 sequence from mRNF213-pFastBAC1 were introduced into peGFP-C1 using BamHI and HpaI
eGFP-mRNF213-pFastBAC1	Expression plasmid encoding N-terminally eGFP-tagged mRNF213 for expression in mammalian cells	VspI (blunted)-XbaI fragment of peGFP-mRNF213 5,892 was introduced into mRNF213-pFastBAC1 digested with BpiI (blunted) and XbaI

7.5 Primers

7.5.1 Primers for molecular cloning

Name	Sequence 5'-3'	Application
KSHV ORF61-pmCherry <u>EcoRI</u> fwd	TATA<u>GAATTC</u>CCACCATGTCTGTCCGG ACATTTTG	Cloning KSHV ORF61 into pmCherry using EcoRI and BamHI restriction sites
KSHV ORF61-pmCherry <u>BamHI</u> rev	TTAA<u>GGATCC</u>TTCTGACAGACCAGGCA CTC	

MHV-68 ORF61-pmCherry <u>BglII</u> fwd	TATA<u>AGATCT</u>CCACCATGGCGACCCAAACCATG	Cloning MHV-68 ORF61 into pmCherry using BglII and SalI restriction sites
MHV-68 ORF61-pmCherry <u>SalI</u> rev	TTAA<u>GTCGAC</u>TTTTGACAGTGCAGACAAGAAGC	
KSHV ORF61 pcDNA3 <u>BamHI</u> fwd	TATA<u>GGATCC</u>CCACCATGTCTGTCCGGACATTTTG	Cloning KSHV ORF61-3xFLAG into pcDNA3 using BamHI and EcoRI restriction sites
KSHV ORF61-3xFLAG pcDNA3 <u>EcoRI</u> rev	TTAA<u>GAATTC</u>CTACTTGTCGTCGTCGTCCTTGTAGTCGATGTCGTGGTCCTTGTAGTCACCGTCGTGGTCCTTGTAGTCCTGACAGACCAGGCACTC	
KSHV ORF61*mut*IPAM fwd	GGGCTCGTGCCAGGGCGCCGGCAGCAGCAGCA AGCCAGTCCATGAGCTTCTT	Introducing IPAM mutation (PFVDQ to PAAAA) into pcDNA3-KSHV ORF61-FLAG by overlap extension PCR
BGH rev	TAGAAGGCACAGTCGAGG	
pcDNA3 fwd	CGTGTACGGTGGGAGGTC	
KSHV ORF61*mut*IPAM rev	AAGAAGCTCATGGACTGGCTTGCTGCTGCTGC CGGCGCCCTGGCACGAGCCC	
MHV-68 ORF61 pcDNA3 <u>EcoRV</u> fwd	TATA<u>GATATC</u>CCACCATGGCGACCCAAACCATG	Cloning MHV-68 ORF61-3xFLAG into pcDNA3 using EcoRV and XbaI restriction sites
MHV-68 ORF61-3xFLAG pcDNA3 <u>XbaI</u> rev	TTAA<u>TCTAGA</u>CTACTTGTCGTCGTCGTCCTTGTAGTCGATGTCGTGGTCCTTGTAGTCACCGTCGTGGTCCTTGTAGTCTTGACAGTGCAGACAAGAAGC	
mA1-3xHA pcDNA3 Gibson 1 fwd	ATAGGGAGACCCAAGCTTGGTACCGAGCTCATGAGTTCCGAGACAGGCCCT	
mA1-3xHA pcDNA3 Gibson 1 rev	GTCAGGAACATCGTATGGGTACATGAATTGTTTCAACCCTGTAGCCCAAAGGA	
mA3-3xHA pcDNA3 Gibson 1 fwd	ATAGGGAGACCCAAGCTTGGTACCGAGCTCATGGGACCATTCTGTCTGGGATG	Cloning mA1- and mA3-3xHA into pcDNA3 by homology-based DNA assembly
mA3-3xHA pcDNA3 Gibson 1 rev	GTCAGGAACATCGTATGGGTACATGAATTGAGACATCGGGGGTCCAAGCTG	
3xHA pcDNA3 Gibson 2 fwd	CAATTCATGTACCCATACGATGTTCCTGACTATGCGGGCTATCCCTATGACG	
3xHA pcDNA3 Gibson 2 rev	GAGCGGCCGCCAGTGTGATGGATATCTGCATTAAGCAGCGTAATCTGGAACGT	
KSHV ORF61-HA pcDNA3 <u>EcoRI</u> rev	TTAA<u>GAATTC</u>CTA AGCGTAATCTGGAACATCGTATGGGTACTGACAGACCAGGCACTC	Cloning KSHV ORF61-HA into pcDNA3 with KSHV ORF61 pcDNA3 BamHI fwd using BamHI and EcoRI restriction sites
MHV-68 ORF61-HA pcDNA3 <u>XbaI</u> rev	TTAA<u>TCTAGA</u>CTA AGCGTAATCTGGAACATCGTATGGGTATTGACAGTGCAGACAAGAAGC	Cloning MHV-68 ORF61-HA into pcDNA3 with MHV-68 ORF61 pcDNA3 EcoRV fwd using EcoRV and XbaI restriction sites

A3B-mScarlet-HA pLIX402 Gibson 1 fwd	AGTGAACCGTCAGATCGCCTGGAGAAT TGGATGAATCCACAGATCAGAAATCC	
A3B-mScarlet-HA pLIX402 Gibson 1 rev	CACCTGATCCACCGGATCCACCTGATC CACCGGATCCACCGTTTCCCTGATTCT GGAGAATG	
A3G-mScarlet-HA pLIX402 Gibson 1 fwd	AGTGAACCGTCAGATCGCCTGGAGAAT TGGATGAAGCCTCACTTCAGAAACAC	Cloning A3B- and A3G-mScarlet-HA into pLIX402 by homology-based DNA assembly
A3G-mScarlet-HA pLIX402 Gibson 1 rev	CACCTGATCCACCGGATCCACCTGATC CACCGGATCCACCGTTTTCCTGATTCT GGAGAATGG	
A3-mScarlet-HA Gibson 2 fwd	GTGGATCAGGTGGATCCGGTGGATCAG GTGGATCCGGTGGATCAACTAGTGTG	
A3-mScarlet-HA Gibson 2 rev	AGTGGTGGTGGTGGTGGTGGACCGGAC GCGTCAAGCGTAGTCTGGGACGTC	
p3xHA-N1 Gibson fwd	AATTCTGCAGTCGACGGTACCGCGGGC CCGGGATCCACCGGTCGCCACCATGTA CCCATACGATGTTCCTGAC	Cloning 3xHA into peGFP-N1 in place of eGFP by homology-based DNA assembly
p3xHA-N1 Gibson rev	ATGTGGTATGGCTGATTATGATCTAGA GTCTTAAGCAGCGTAATCTGGAACGT	
Mouse UHRF1 p3xHA EcoRI fwd	TATA<u>GAATTC</u>ACCATGTGGATCCAGGT TCGAACTATG	Cloning mouse UHRF1 into p3xHA-N1 using EcoRI and KpnI restriction sites
Mouse UHRF1 p3xHA KpnI rev	TTAA<u>GGTACC</u>TTCCGGCCGCTGCCATA GCCAG	
HA-Mouse BST2 pcDNA3 KpnI fwd	TATA<u>GGTACC</u>ACCATGTACCCATACGA TGTTCCAGATTACGCTGCGCCCTCTTT CTATCACTATCT	Cloning HA-Mouse BST2 into pcDNA3 using KpnI and EcoRI restriction sites
HA-Mouse BST2 pcDNA3 EcoRI rev	TTAA<u>GAATTC</u>TCAAAAGAGCAGGAACA GTGACACTT	
Mouse TAX1BP1 p3xHA EcoRI fwd	TATA<u>GAATTC</u>ACCATGACATCCTTTCA AGAAGTCC	Cloning mouse TAX1BP1 into p3xHA-N1 using EcoRI and KpnI restriction sites
Mouse TAX1BP1 p3xHA KpnI rev	TTAA<u>GGTACC</u>TTGTCGAAGTTGAGAAC ATTCTG	

7.5.2 Primers for *en passant* mutagenesis

Name	Sequence 5'-3'	Application
KSHV$_{Lyt}$ ΔGFP Zeo BAC fwd	TGATAAGCTGTCAAACATGAGAATTGGTCG ACGGCCCAACTGTTGACAATTAATCATCGG CAT	Replacing the eGFP-HygroR cassette in KSHV$_{Lyt}$ with a ZeoR cassette
KSHV$_{Lyt}$ ΔGFP Zeo BAC rev	GCTCCGGTGCCCGTCAGTGGGCAGAGCGCA CATCGCCCACTCAGTCCTGCTCCTCGGCCA	
KSHV mNeon-ORF61 BAC fwd	GGACAGCTCCCAAGTGAACCTGACAAAATG TCCGGACAGATGATCCACCGGATCCACCCTT GTACAGCTCGTCCATGCCC	Introducing mNeonGreen followed by a linker to the N-terminus of ORF61 in KSHV$_{Lyt}$ ΔGFP BAC
KSHV mNeon-ORF61 BAC rev	GCCGCGTGTGGCCCCTGGACTGTGTTTCTGT AAGGTCATGGTGAGCAAGGGCGAGGAGGA	
KSHV ORF61 PFVAA IPAM mut BAC fwd	TGACTCTGTCCTCCTTGAGGAAGAAGCTCA TGGACTGGCTAGCTGCTACAAACGGCGCCC TGGCACGAGCCCTAGGGATAACAGGGTAAT CGATTT	Mutating the IPAM (PFVDQ to PFVAA) in KSHV mNeon-ORF61 BAC
KSHV ORF61 PFVAA IPAM mut BAC rev	TAAGCTACTGGATAGGGCTCGTGCCAGGGC GCCGTTTGTAGCAGCTAGCCAGTCCATGAG CTTCTTGCCAGTGTTACAACCAATTA	

MHV-68 ΔGFP Zeo BAC fwd	ATAGTAATCAATTACGGGGTCATTAGTTCATAGCCCATATTCAGTCCTGCTCCTCGGCCA	Replacing the eGFP cassette in MHV-68 BAC pHA3 with a ZeoR cassette
MHV-68 ΔGFP Zeo BAC rev	GTAAAACCTCTACAAATGTGGTATGGCTGATTATGATCAGTGTTGACAATTAATCATCGGCAT	
MHV-68 ORF61-mNeon BAC fwd	CATGGTAAATTTTACTGATTTTATTGAGAGCAATCAGTTACTTGTACAGCTCGTCCATGCCC	Introducing mNeonGreen preceded by a linker to the C-terminus of ORF61 in MHV-68 ΔGFP BAC
MHV-68 ORF61-mNeon BAC rev	GTGTTCACTATCTGTGGGTGCTTCTTGTCTGCACTGTCAAGGTGGATCCGGTGGATCAGTGAGCAAGGGCGAGGAGGAC	
MHV-68 ORF61-3xFLAG BAC fwd	ATCCATGGTAAATTTTACTGATTTTATTGAGAGCAATCAGCTACTTGTCGTCGTCGTCCTTGTAGTCGATGTCGTGGTCCGCCAGTGTTACAACCAATTA	Introducing a 3xFLAG-tag preceded by a linker to the C-terminus of ORF61 in MHV-68 BAC pHA3
MHV-68 ORF61-3xFLAG BAC rev	GTGTTCACTATCTGTGGGTGCTTCTTGTCTGCACTGTCAAGGCTCTGGCGACTACAAGGACCA	
MHV-68 ORF61 PFIAA IPAM mut BAC fwd	TTGCATAATCTTCATTCAAAAACAAGGTCATAGACTGGCTAGCTGCAATGAATGGTGCCCTAAGCATAGCTCTAGGGATAACAGGGTAATCGATTT	Mutating the IPAM (PFIDQ to PFIAA) in MHV-68 ORF61-FLAG BAC
MHV-68 ORF61 PFIAA IPAM mut BAC rev	CCTGTATGTACGCAGAGCTATGCTTAGGGCACCATTCATTGCAGCTAGCCAGTCTATGACCTTGTTGCCAGTGTTACAACCAATTA	

7.5.3 Primers for 3D-PCR

Name	Sequence 5'-3'	Application
KSHV ORF45 3D PCR fwd	AGGCAATAACTCGTGTGCTTTGTAAAT	First-round amplification of a 577-bp fragment of KSHV ORF45
KSHV ORF45 3D PCR rev	AAAATCCGTCATCCTGACTAACCCATC	
KSHV ORF45 3D PCR nested fwd	AGCACACACGATGAAGAGAGAATGCTT	Second round, nested amplification of a 411-bp fragment of KSHV ORF45
KSHV ORF45 3D PCR nested rev	TACCACTGCTACCGGTTTGGGCGTATG	

7.6 Antibodies

7.6.1 Primary antibodies

Antigen	Clone	Species	Dilution	Reference
FLAG	M2	Mouse	1:1000 WB 1:500 IF	Sigma
FLAG	Polyclonal	Rabbit	1:400 IF	F7425, Sigma
mNeonGreen	32F6	Mouse	1:1000 WB	Proteintech
GAPDH	14C10	Rabbit	1:1000 WB	Cell Signaling
β-Actin	AC-74	Mouse	1:3000 WB	Sigma
HA	3F10	Rat	1:500 WB 1:500 IF	Roche
HA	Polyclonal	Rabbit	1:100 IF 1:300 IP	H6908, Sigma
Vimentin	RV202	Mouse	1:50 IF	Santa Cruz

7.6.2 Secondary antibodies

Antigen	Species	Conjugate	Dilution	Reference
Mouse IgG	Goat	HRP	1:10000	DakoCytomation
Rabbit IgG	Swine	HRP	1:10000	DakoCytomation
Rat IgG	Goat	HRP	1:5000	Jackson ImmunoResearch
Mouse IgG light chain	Goat	HRP	1:5000	Jackson ImmunoResearch
Rabbit IgG	Goat	Alexa Fluor™ 488	1:1000	Thermo Fisher Scientific
Mouse IgG	Goat	Alexa Fluor™ 555	1:1000	Thermo Fisher Scientific
Rat IgG	Goat	Alexa Fluor™ 555	1:1000	Thermo Fisher Scientific
Mouse IgG	Goat	Alexa Fluor™ 647	1:1000	Thermo Fisher Scientific

7.7 Chemicals and reagents

7.7.1 Antibiotics

Name	Working concentration	Application	Reference
Ampicillin	100 µg/ml	Selection of bacteria	Carl Roth
Chloramphenicol	15 µg/ml	Selection of bacteria	Carl Roth
Kanamycin	50 µg/ml	Selection of bacteria	Carl Roth
Zeocin™	50 µg/ml	Selection of bacteria	Thermo Fisher Scientific
Puromycin	2.5 µg/ml	Selection of transduced cells	Sigma
Doxycycline	1 µg/ml	Induction of TRE promoter-controlled gene expression	Biomol

7.7.2 Enzymes

Name	Reference
FastDigest restriction enzymes and buffer	Thermo Fisher Scientific
DreamTaq DNA polymerase and buffer	Thermo Fisher Scientific
Phusion™ High-Fidelity DNA polymerase and buffer	Thermo Fisher Scientific
T4 DNA ligase and buffer	Thermo Fisher Scientific
FastAP thermosensitive alkaline phosphatase	Thermo Fisher Scientific
EDTA-free cOmplete™ protease inhibitor cocktail	Roche
Benzonase® endonuclease	Merck
Klenow Fragment	Thermo Fisher Scientific
NEBuilder® HiFi DNA Assembly Master Mix	New England Biolabs

7.7.3 Other reagents and chemicals

Name	Application	Reference
Hoechst 33342	Fluorescence microscopy	Invitrogen
Rhodamine phalloidin	Fluorescence microscopy	Invitrogen

GenJet™ In Vitro DNA transfection reagent	Transfection	SignaGen	
Polyethylenimine (PEI)	Transfection	Sigma	
3-Methyladenine (3-MA)	Autophagy inhibition	Sigma	
Polybrene	Lentiviral transduction	Sigma	
mNeonGreen-Trap Agarose	Immunoprecipitation	Proteintech	
Binding Control Agarose Beads	Immunoprecipitation	Proteintech	
rProtein A Sepharose™ Fast Flow resin beads	Immunoprecipitation	Cytiva	
Amersham™ enhanced chemiluminescence (ECL) detection reagent	Immunoblot	Cytiva	
Lumigen ECL Ultra TMA-6	Immunoblot	Lumigen	
LE Agarose	Agarose gel electrophoresis	Biozym	
TopVision Low Melting Point Agarose	Agarose gel electrophoresis	Thermo Fisher Scientific	
GeneRuler DNA Ladder Mix	Agarose gel electrophoresis	Thermo Fisher Scientific	
PageRuler™ Prestained Protein Ladder	SDS-PAGE	Thermo Fisher Scientific	

All other common chemicals were purchased from Carl Roth, Merck or Sigma.

7.8 Media

7.8.1 Cell culture media

Name	Component	Working concentration	Reference
DMEM growth medium	Dulbecco's Modified Eagle Medium (DMEM) w: 4.5 g/l glucose w: L-glutamine	1x	PAN-Biotech
	Fetal bovine serum (FBS) Standard, 0.2 µm sterile filtered	10%	PAN-Biotech
	HEPES	15 mM	Gibco
	Penicillin-Streptomycin (P/S)	100 U (P) 100 µg/ml (S)	Sigma
DMEM/F-12 growth medium	DMEM/F12 GlutaMAX™	1x	Gibco
	FBS Standard	10%	PAN-Biotech
	HEPES	15 mM	Gibco
	Sodium pyruvate	1 mM	Gibco
	P/S	100 U (P) 100 µg/ml (S)	Sigma
Endothelial growth medium	EBM®-2 Endothelial Cell Growth Basal Medium	1x	Lonza
	EGM®-2 MV Microvascular Endothelial SingleQuots®	1x	Lonza
	P/S	100 U (P) 100 µg/ml (S)	Sigma

	DMEM w: 4.5 g/l glucose w: L-glutamine	1x	PAN-Biotech
Tet-free DMEM growth medium	FBS Premium, tetracycline free, 0.2 μm sterile filtered	10%	PAN-Biotech
	HEPES	15 mM	Gibco
	P/S	100 U (P) 100 μg/ml (S)	Sigma
Dulbecco's Phosphate Buffered Saline (PBS)	Ready to use	1x	Sigma
0.5 % Trypsin-EDTA	Ready to use	1x	Sigma

7.8.2 Bacterial culture media

Name	Component	Reference
Lysogeny broth (LB) liquid medium	LB Broth (Lennox)	Carl Roth
LB agar	LB Broth (Lennox)	Carl Roth
	1.5% Agar-Agar, Kobe I	Carl Roth

7.9 Buffers

7.9.1 Small-scale plasmid DNA extraction from bacteria (Mini-Prep)

Name	Component	Application
S1 buffer pH 8.0	50 mM Tris-HCl	Resuspending the bacterial pellet
	10 mM EDTA	
	100 μg/ml RNase A	
S2 buffer	200 mM NaOH	Lysing the bacteria
	1% (v/v) SDS	
S3 buffer pH 5.1	2.8 M potassium acetate	Neutralizing the lysis buffer
Tris-HCl pH 8.0	10 mM Tris-HCl	Resuspending DNA

7.9.2 Agarose gel electrophoresis

Name	Component	Application
50x TAE buffer pH 8.0	2 M Tris-HCl	Used 1x for preparing agarose gel and as running buffer
	50 mM EDTA	
	5.7% (v/v) acetic acid	
10x TBE buffer pH 8.0	990 mM Tris-HCl	Used 0.5x for preparing agarose BAC gel and as running buffer
	40 mM EDTA	
	990 mM (w/v) boric acid	

7.9.3 SDS polyacrylamide gel electrophoresis (SDS-PAGE) and immunoblot

Name	Component	Application
NP40 lysis buffer pH 7.5	50 mM Tris-HCl	Mild cell lysis for lysate fractionation
	150 mM NaCl	
	1% (v/v) Nonidet P-40	
RIPA lysis buffer pH 7.5	50 mM Tris-HCl	Lysis and washing buffer for immunoprecipitation
	150 mM NaCl	
	0.1% (w/v) SDS	
	1% (v/v) Triton X-100	
	1% (w/v) sodium deoxycholate	
5x SDS-PAGE sample buffer pH 6.8	312 mM Tris-HCl	Lysis and SDS-PAGE loading buffer for soluble lysate fractions
	50% (v/v) glycerol	
	10% (w/v) SDS	
	25% (v/v) 2-mercaptoethanol	
	Bromophenol blue	
2x SDS-PAGE sample buffer pH 6.8	125 mM Tris-HCl	Lysis and loading buffer for SDS-PAGE
	20% (v/v) glycerol	
	4% (w/v) SDS	
	10% (v/v) 2-mercaptoethanol	
	Bromophenol blue	
10x running buffer	250 mM Tris	Used 1x as running buffer for SDS-PAGE
	1.92 M (w/v) glycine	
	1% (w/v) SDS	
Transfer buffer	50 mM Tris	Semi-dry blotting
	40 mM (w/v) glycine	
	0.04% (w/v) SDS	
	20% (v/v) methanol	
10x TBS-T pH 7.6	100 mM Tris-HCl	Used 1x for washing nitrocellulose membranes
	1.5 M NaCl	
	1% (v/v) Tween 20	
Tris-HCl resolving gel pH 8.8	10% (v/v) acrylamide:bisacrylamide (37.5:1)	Resolving gel for SDS-PAGE
	375 mM Tris-HCl	
	0.1% (v/v) SDS	
	0.1% (v/v) APS	
	0.1% (v/v) TEMED	

Tris-HCl stacking gel pH 6.8	4% (v/v) acrylamide:bisacrylamide (37.5:1)	Stacking gel for SDS-PAGE
	125 mM Tris-HCl	
	0.1% (v/v) SDS	
	0.1% (v/v) APS	
	0.1% (v/v) TEMED	

7.9.4 Immunoprecipitation

Name	Component
Minimal washing buffer pH 7.5	50 mM Tris-HCl
	150 mM NaCl
	10% (v/v) glycerol
Washing buffer 1 pH 7.5	1 mM Tris-HCl
	150 mM NaCl
	2 mM EDTA
	0.2% (v/v) Nonidet P-40
Washing buffer 2 pH 7.5	1 mM Tris-HCl
	500 mM NaCl
	2 mM EDTA
	0.2% (v/v) Nonidet P-40
Washing buffer 3 pH 7.5	10 mM Tris-HCl
Dilution buffer pH 7.5	10 mM Tris-HCl
	150 mM NaCl
	0.5 mM EDTA

7.9.5 Immunofluorescence

Name	Component
Fixing solution	4% (w/v) paraformaldehyde in PBS
Quenching solution	50 mM NH_4Cl in PBS
Permeabilization solution	0.5% Triton X-100 in PBS
TBS-BG blocking buffer	Tris-buffered saline (TBS)
	5% (w/v) glycine
	5% (w/v) BSA
	0.05% (v/v) Tween 20
	0.05% (v/v) NaN_3

7.10 Kits

Name	Reference
NucleoSpin Gel and PCR Clean-up	Macherey-Nagel
mi-Plasmid Miniprep	metabion
NucleoBond Xtra Midi	Macherey-Nagel
innuPREP DNA Mini Kit 2.0	Innuscreen GmbH

7.11 Other materials and equipment

Name	Application	Reference
GenePulser Xcell™	Electroporation	Bio-Rad
NanoDrop® ND-1000 Spectrophotometer	Measuring DNA concentration	Peqlab
GelDoc XR+	Visualization of DNA on agarose gels	Bio-Rad
Amersham™ Protran™ Premium 0.2 µm nitrocellulose membrane	Immunoblot	Cytiva
Whatman® gel blotting paper, grade GB003	Immunoblot	Sigma
TC10™ Automated Cell Counter	Counting cells	Bio-Rad
Herasafe™ KS laminar flow hood	Cell culture	Thermo Fisher Scientific
CoolCell LX freezing container	Freezing cells	BioCision
Bioruptor® Plus UCD-200 sonicator	Sample collection for LC-MS/MS analysis	Diagenode
Trans-Blot Turbo Transfer System	Semi-dry blotting	Bio-Rad
Fusion Capture Advance FX7 16.15	Immunodetection	Peqlab
µ-Slide 8 well	Immunofluorescence	ibidi
µ-Dish 35 mm Quad	FRAP	ibidi
µ-Dish 35 mm high Grid-500	CLEM	ibidi
Nikon Ti2 A1 confocal laser scanning microscope with a 1.4 NA 60x Plan Apo objective	Confocal fluorescence microscopy FRAP	Nikon
Nikon Ti2/Yokogawa CSU-W1 confocal spinning disk microscope with a 1.45 NA 100x Plan Apo objective	Confocal fluorescence microscopy	Nikon
0.75 NA 20x Plan Apo VC objective	CLEM	Nikon
Biometra TAdvanced Twin 48 thermocycler	(3D-)PCR	Analytik Jena

8. Methods

8.1 Molecular biology

8.1.1 Preparation of electrocompetent *E.coli* DH10B and GS1783

10 ml of LB medium was inoculated with *E.coli* DH10B or GS1783 and incubated overnight under continuous shaking without antibiotics at 37°C (DH10B) or with 15 μg/ml chloramphenicol at 30°C (GS1783). 200 ml of pre-warmed LB medium was then inoculated with 5 ml (DH10B) or 10 ml (GS1783) of pre-culture and incubated under the same conditions until OD_{600} of 0.5-0.6 was reached. In the case of GS1783, the Red recombinase system was induced for 15 min at 42°C followed by 20 min incubation on ice. DH10B were incubated on ice immediately after reaching the correct OD_{600}. The bacteria were then pelleted (5,000 × g, 4°C, 10 min), washed twice in 100 ml ice-cold ddH_2O and once in 10 ml sterile ice-cold 10% glycerol (5,000 × g, 4°C, 10 min). The pellet was resuspended in 1 ml sterile ice-cold 10% glycerol and aliquoted, and the aliquots were stored at -80°C.

8.1.2 Bacterial transformation

Aliquots of electrocompetent *E.coli* DH10B and GS1783 were thawed on ice. 40 μl of GS1783 was mixed with 150 ng of purified, PCR-amplified linear DNA or 1-10 ng of purified plasmid DNA, whereas 50 μl of DH10B was mixed with 4 μl of ligation product. The bacteria were electroporated in pre-chilled 2 mm electroporation cuvettes at 2.5 kV, 25 μF and 200 Ω, resuspended in LB medium and shaked at 30°C (GS1783) or 37°C (DH10B) for 1 h. Bacteria were then plated on LB agar containing the proper antibiotics for selection and incubated at the corresponding temperature overnight. Lower incubation temperature was used for GS1783 to prevent induction of the Red recombinase system. On the following day, single colonies were picked for liquid culture.

8.1.3 Small-scale plasmid DNA extraction from bacteria (Mini-Prep)

Single colonies of transformed bacteria were grown overnight in 3 ml LB medium containing the proper antibiotics at 37°C or in 5 ml LB culture at 30°C for low-copy BAC plasmid DNA extraction. 2 ml (4 ml for BAC extraction) of the culture was then subjected to plasmid DNA extraction essentially as described (168). Bacteria were pelleted by 2 min centrifugation at 21,000 × g and the medium discarded. The pellet was resuspended in 300 μl S1 buffer followed by alkaline lysis in 300 μl S2 buffer for 5 min at room temperature to selectively denature high molecular weight chromosomal DNA while preserving the integrity of circular plasmid DNA. The lysate was then neutralized in 300 μl S3 buffer for 5 min at 4°C to renature chromosomal DNA followed by 20 min centrifugation at 21,000 × g and 4°C to pellet proteins and clotted chromosomal DNA. 800 μl of the supernatant containing the plasmid DNA was then mixed with 640 μl isopropanol and centrifuged for at least 30 min at 21,000 × g and 4°C to precipitate the DNA. The DNA pellet was washed with 70% (v/v) ethanol, dried and resuspended in 50 μl ddH_2O.

To obtain DNA with a higher purity for immediate transfection, the extraction was performed using mi-Plasmid Miniprep kit (metabion) as per manufacturer's instructions. The DNA was dissolved in 50 µl 10 mM Tris (pH 8.0) and the DNA concentration measured with NanoDrop® ND-1000 Spectrophotometer (Peqlab).

8.1.4 Midscale plasmid DNA extraction from bacteria (Midi-Prep)

For a higher BAC or plasmid DNA yield, transformed bacteria were grown overnight in 200 ml LB medium containing the proper antibiotics at 37°C (DH10B) or 30°C (GS1783) and the plasmid DNA extracted using NucleoBond Xtra Midi kit (Macherey-Nagel) according to the manufacturer's protocol. Low-copy extraction protocol was used for BAC DNA and high-copy extraction protocol for plasmid DNA. The DNA was dissolved in 80-400 µl 10 mM Tris (pH 8.0), depending on the size of the pellet, and the DNA concentration was measured with NanoDrop® ND-1000 Spectrophotometer (Peqlab).

8.1.5 Phenol-chloroform DNA extraction

Upon excising large, digested DNA fragments from the agarose gel as described in section 8.1.8, the melted agarose was mixed thoroughly with an equal volume of phenol:chloroform:isoamyl alcohol (25:24:1). The resulting emulsion was separated into two phases by 10 min centrifugation at $21,000 \times g$ and room temperature (RT), after which the aqueous supernatant containing the DNA was transferred to a clean tube. For precipitating the DNA, 1/10 volume of sodium acetate (pH 5.5) and 2 volumes of ice-cold 100% ethanol were added and the mixture kept at -80°C for 20 min. The DNA was pelleted by 15 min centrifugation at $21,000 \times g$ and RT, and the pellet was washed with 70% (v/v) ethanol, dried and resuspended in 10 µl ddH$_2$O.

8.1.6 Polymerase chain reaction (PCR)

Phusion™ High-Fidelity DNA polymerase (Thermo Fisher Scientific) was used as per manufacturer's instructions for cloning and sequencing purposes which require proof-reading activity of the polymerase. DreamTaq DNA polymerase (Thermo Fisher Scientific) was used for differential DNA denaturation PCR (3D-PCR) as per manufacturer's instructions (see 8.1.12). 10-100 ng template DNA was used for amplification. T$_m$ Calculator from Thermo Fisher Scientific was used for determining the optimal annealing temperature of the primers.

8.1.7 DNA restriction digest

PCR products and plasmids were digested with FastDigest restriction enzymes (Thermo Fisher Scientific) for 45-60 min at 37°C according to the manufacturer's protocol. To degrade residual plasmid DNA stemming from the template, PCR products used for cloning were additionally digested with DpnI that only digests methylated DNA. FastAP, an alkaline phosphatase, was included in the

vector digest to dephosphorylate the vector and prevent its self-ligation. When the available unique restriction sites of the insert and vector were not compatible, Klenow Fragment (Thermo Fisher Scientific) was used to create compatible blunt ends according to the manufacturer's protocol.

8.1.8 Agarose gel electrophoresis

The restriction pattern of digested DNA was confirmed by agarose gel electrophoresis. Digested BAC DNA was run on 0.6% (w/v) TBE agarose at 50 V overnight for thorough separation, whereas PCR products and smaller plasmids were separated on 1% (w/v) TAE agarose at 100-120 V for 45-60 min. 0.5 μg/ml ethidium bromide was used to visualize DNA and the gels were imaged with GelDoc XR+ (Bio-Rad). Inserts and vector backbones were cut out under UV illumination and the DNA extracted using NucleoSpin Gel and PCR Clean-up kit (Macherey-Nagel) according to the manufacturer's protocol. When purifying larger fragments (> 15 kbp) from the gel, the digested DNA was separated on 1% (w/v) TAE low-melting agarose at 80 V for 90 min. The fragment was then cut out, incubated under shaking at 65°C to melt the agarose and subjected to phenol-chloroform DNA extraction to avoid DNA shredding caused by column purification (see 8.1.5).

8.1.9 Ligation

Digested inserts and linearized vectors were ligated at a molar ratio 5:1 (insert : vector) at 16°C overnight using T4 DNA ligase (Thermo Fisher Scientific) according to the manufacturer's protocol.

8.1.10 DNA sequencing

Sanger sequencing of PCR products and plasmid DNA was performed by Microsynth Seqlab GmbH (Maschmühlenweg 36, 37081 Göttingen, Germany), and Oxford Nanopore sequencing of BAC DNA was performed by Eurofins Genomics Germany GmbH (Anzinger Str. 7a, 85560 Ebersberg, Germany).

8.1.11 *En passant* mutagenesis

For introducing tag sequences, point mutations or deletions into the viral genome, a bacterial artificial chromosome (BAC) containing the full-length KSHV$_{Lyt}$ (128) or MHV-68 (160) genome was modified using *en passant* mutagenesis, essentially as described (162, 163). *En passant* mutagenesis is based on a Red recombination system that originates from λ phages and uses homologous recombination for insertion of linear dsDNA molecules. In the first step, a kanamycin selection cassette preceded by a I-SceI restriction site was amplified with primers containing both 40 bp homology sequences flanking the desired integration site in the viral genome and a sequence duplication of at least 30 bp for a second recombination upon excision of the selection cassette. Alternatively, a Zeocin™ selection cassette was amplified using a similar primer design, but without the sequence duplication. *E.coli* GS1783 containing the BAC were then transformed with 150 ng of

the purified PCR product and cointegrates selected on LB agar with 50 µg/ml kanamycin or Zeocin™ for successful integration and 15 µg/ml chloramphenicol for presence of the BAC. After 24 h incubation at 30°C, liquid cultures were inoculated with single clones and DNA extracted on the following day as described in 8.1.3. A successful integration of the selection cassette and integrity of the cointegrates was verified by restriction fragment length pattern (RFLP) analysis consisting of restriction digest of the BAC DNA with at least two different restriction enzymes (see 8.1.7) followed by gel electrophoresis (see 8.1.8). When introducing a deletion into the BAC cassette, the Zeocin™ cassette was subsequently not excised. The kanamycin cassette introduced with tag sequences or point mutations was removed in a second recombination step, for which 3-4 different cointegrates were selected. First, expression of the arabinose-inducible homing endonuclease I-SceI was induced by incubation in LB containing 2% L-arabinose for 1 h at 30°C, after which the temperature-inducible Red genes were induced by 25 min incubation at 42°C. After recovering at 30°C for at least 2.5 h, different dilutions of the liquid cultures, depending on their OD_{600}, were plated on LB agar containing 15 µg/ml chloramphenicol and 2% L-arabinose and incubated at 30°C for 24 h. Single clones were then picked for liquid culture and subsequent DNA extraction followed by RFLP analysis. Correct modification of the BAC DNA was verified by PCR and Sanger sequencing of the target region. The genome sequences of ORF61*mut*IPAM viruses, that are derivatives of the corresponding tagged ORF61 viruses, were additionally analyzed by Oxford Nanopore sequencing but no relevant deviations from the expected sequence were detected. Two independent clones of each modified BAC were subjected to midscale plasmid DNA extraction (see 8.1.4) and transfection into permissive cells for virus reconstitution (see 8.2.3).

8.1.12 Differential DNA denaturation PCR (3D-PCR)

TetOn A3B RPE-1 cells were infected with KSHV mNeon-ORF61 or mNeon-ORF61*mut*IPAM and either treated with 1 µg/ml doxycycline or left untreated. At 7 dpi, supernatants were collected and viral DNA extracted with an innuPREP DNA Mini Kit 2.0 (Innuscreen GmbH) as per manufacturer's instructions. A nested PCR approach (133) was adapted to amplify a fragment of the viral ORF45 gene using the extracted DNA as a template. In a first-round PCR a 577 bp fragment of ORF45 was amplified using DreamTaq DNA polymerase (Thermo Fisher Scientific) according to the manufacturer's protocol, thereby applying following cycling conditions: initial denaturation at 95°C for 5 min followed by 35 cycles of 1 min denaturation at 95°C, 30 s annealing at 60°C, 39 s elongation at 72°C and 10 min final elongation at 72°C. One µl of the product was then used as a template for a second PCR to amplify a 411 bp fragment applying the following PCR conditions: a denaturation temperature gradient from 84.4 to 86.0°C for 5 min followed by 35 cycles of 1 min denaturation at 84.4 to 86.0°C, 30 s annealing at 62°C, 25 s elongation at 72°C and 10 min final elongation at 72°C. Both PCRs were run on a Biometra TAdvanced Twin 48 thermocycler (Analytik Jena). The PCR

products were separated on a 1% TAE agarose gel, visualized with ethidium bromide and imaged with GelDoc XR+ (Bio-Rad).

8.2 Cell biology and virology

8.2.1 Cell culture

All human and murine cells were maintained on 10 or 15 cm cell culture dishes at 37°C, 5% CO_2 and 80% relative humidity. For TIME cells the dishes were coated with 0.4% gelatin. To maintain a sterile working environment, all cell culture work was performed under a laminar flow hood (Herasafe™ KS, Thermo Fisher Scientific). ARPE-19 cells were grown in DMEM/F-12 growth medium, TIME cells in endothelial growth medium, TetOn A3 RPE-1 cells in Tet-free DMEM growth medium and all other cells in DMEM growth medium (see 7.8.1 for medium composition).

Cells were passaged at 80-90% confluence by removing the medium, washing once with PBS and incubating shortly with trypsin-EDTA at 37°C. Trypsin was neutralized by adding serum-containing growth medium and the cells split 1:3 to 1:10. When passaging TIME cells, the trypsin was removed by centrifugation (150 × g, 5 min) before plating the cells. For determining the cell concentration, 10 µl of the thoroughly mixed cell suspension was analyzed with a TC10™ Automated Cell Counter (Bio-Rad).

For freezing cells, the cells were trypsinized and the desired number of cells (approx. $2x10^6$/vial) pelleted by centrifugation (150 × g, 5 min). The cell pellet was resuspended in freezing medium that consisted of 70% pure DMEM, 20% FBS and 10% DMSO for TIME cells and of 90% FBS and 10% DMSO for all other cells. 1 ml aliquots were frozen in a CoolCell LX freezing container (BioCision) at -80°C for at least 4 h. For long-time storage the cells were transferred to liquid nitrogen.

For thawing cells, the aliquots were thawed in a water bath at 37°C and then gently mixed with 9 ml of complete growth medium. The cells were pelleted at 150 × g for 5 min to remove the freezing medium, resuspended in fresh growth medium and transferred to a culture dish. To avoid centrifuging the sensitive TIME cells after thawing, the thawed aliquot was gently mixed with a complete growth medium and directly transferred to a gelatin-coated culture dish. On the following day, TIME cells were washed once with PBS to remove the freezing medium, and fresh medium was added.

8.2.2 Transfection of plasmid DNA

$3x10^6$ HEK-293T cells were seeded on a 10 cm dish for lentivirus production and $2.5x10^6$ HEK-293A cells for immunoprecipitation. On the following day, HEK-293T cells were transfected with 4 µg of a lentiviral vector and a total of 4 µg of packaging plasmids, whereas HEK-293A cells were transfected with a total of 6 µg of expression plasmids. The plasmid DNA was diluted in pure DMEM without supplements, mixed with PEI (Sigma) in a 4:1 ratio (4 µl PEI per µg DNA) followed by 20 min incubation at RT. The volume of growth medium was first reduced to 7 ml and the mixture was then

added dropwise on the culture dish. 6 h later the medium was discarded, the cells washed once with PBS and 8 ml of fresh medium added.

For confocal fluorescence microscopy, $3.5x10^4$ U2OS cells were seeded on a μ-Slide 8 well (ibidi) coated with 0.4% gelatin and for FRAP on a gelatin-coated μ-Dish 35 mm Quad (ibidi). On the following day, 400 ng plasmid DNA was diluted in pure DMEM and mixed with GenJet™ transfection reagent (SignaGen) in a 3:1 ratio as per manufacturer's instructions. After 10 min incubation at RT, the mixture was added dropwise to the cells. 6 h later the medium was discarded, the cells washed once with PBS and fresh medium added. When transfecting HEK-293A cells for imaging, $3.5x10^4$ cells on a gelatin-coated μ-Slide 8 well (ibidi) were transfected with 400 ng plasmid DNA in pure DMEM mixed with PEI (Sigma) in a 4:1 ratio, as described above. Due to low expressions levels, human and murine RNF213 expression plasmids were transfected in threefold excess relative to KSHV and MHV-68 ORF61 plasmids.

8.2.3 Transfection of BAC DNA

For virus reconstitution from BAC DNA, $2x10^5$ ARPE-19 cells (KSHV) or $1.5x10^5$ MEF cells (MHV-68) were seeded on a 6-well plate. On the following day, 3 μg of BAC DNA was diluted in pure DMEM, mixed with GenJet™ transfection reagent (SignaGen) in a 2:1 ratio and incubated 10 min at RT. The mixture was then added dropwise to the cells followed by 6 h incubation before the medium was discarded, the cells washed once with PBS and fresh medium added. After observing a cytopathic effect (CPE), the cells were transferred to a larger dish and used for virus stock production (see 8.2.6 and 8.2.7).

8.2.4 Lentivirus production and transduction

Lentiviral transduction was used to stably express genes of interest in target cells. Lentiviruses were produced by transfecting $3x10^6$ HEK-293T cells with 4 μg lentiviral vector encoding the gene of interest together with 3 μg of the pCMV-dR8.91 packaging plasmid encoding *gag* and *pol* and 1 μg of the pMD2.G packaging plasmid encoding *env*, as described in 8.2.2. After 48 h, the infectious supernatant was collected, filtered through a 0.45 μm syringe filter to remove cells and either frozen at -80°C for further use or directly used for transduction. 8 ml of fresh medium was added to the cells and the procedure repeated at 72 h post-transfection (hpt).

RPE-1 puro cells were transduced by seeding $1.5x10^5$ cells/well on a 6-well plate and infecting them on the following day with 3.5 ml of the lentivirus-containing supernatant collected at 48 hpt, thereby using 5 μg/ml Polybrene (Sigma) and centrifugal enhancement (1,065 × *g*, 37°C, 30 min). The medium was replaced 6 h later and the procedure repeated on the following day with the lentiviral supernatant collected at 72 hpt. After reaching confluency, the cells were transferred to a 10 cm dish and treated with 2.5 μg/ml puromycin to select for successfully transduced cells. The selection was continued until all non-transduced control cells died.

8.2.5 Generation of RPE-1 cells expressing inducible A3-mScarlet-HA

Human A3B and A3G sequences were PCR-amplified from pcDNA3-A3B-HA and pcDNA3-A3G-HA expression plasmids and cloned into the pLIX402 lentiviral vector together with mScarlet- and HA-sequences by homology-based DNA assembly using NEBuilder® HiFi DNA Assembly Master Mix (NEB) as per manufacturer's instructions. Lentiviruses encoding A3B-mScarlet-3xHA or A3G-mScarlet-2xHA were then produced and used to transduce RPE-1 puro cells, as described in 8.2.4. After selecting for transduced cells with 2.5 µg/ml puromycin, single-cell clones were obtained by limiting dilution.

8.2.6 KSHV stock production

A 6-well plate of ARPE-19 cells with $2x10^5$ cells/well was infected at MOI 0.005 using centrifugal enhancement (1,065 × g, 37°C, 30 min). After observing CPE, the cells and the infectious supernatant were transferred to larger dishes until obtaining at least 8-10 infected 15 cm dishes. Supernatants were collected every three days and stored at -80°C until further use. For enhancing the growth of KSHV ORF61*mut*IPAM in confluent cells, the growth medium was supplemented with 1 µM dNTPs at each harvest. When all the cells were infected, they were scraped from the plate, collected in PBS-sucrose-glutamate-serum (PSGC) buffer (169) and frozen at -80°C. To release cell-associated virus, the infected cells were subjected to three freeze-thaw cycles and mechanical lysis using a Dounce homogenizer. Lysed cells and thawed supernatant were then centrifuged at 3,000 × g and 4°C for 10 min to pellet cell debris. The resulting supernatant was centrifuged at 27,000 × g and 4°C for 4 h to concentrate the virus. The supernatant was then discarded and the pellets resuspended in a total of 1-1.5 ml DMEM/F-12 growth medium under gentle rocking on ice overnight. On the following day, the homogenized suspension was cleared of residual cell debris by 10 min centrifugation at 800 × g and 4°C and then frozen in 100 µl aliquots at -80°C.

8.2.7 MHV-68 stock production

At least five 15 cm dishes of MEF cells with $2x10^6$ cells/dish were infected at MOI 0.005. After observing CPE, supernatants were collected every two days and stored at -80°C until further use, continuing until all cells were infected. Thawed supernatants were then centrifuged at 5,000 × g and 4°C for 10 min to pellet cell debris. The resulting supernatant was centrifuged at 27,000 × g and 4°C for 4 h to concentrate the virus. The supernatant was then discarded and the pellets resuspended in a total of 0.7-1 ml DMEM growth medium under gentle rocking on ice overnight. On the following day, the homogenized suspension was cleared of residual cell debris by 10 min centrifugation at 2,000 × g and 4°C and then frozen in 50 µl aliquots at -80°C.

8.2.8 Virus titration by the median tissue culture infectious dose (TCID$_{50}$) method

TCID$_{50}$ is defined as the amount of virus required to infect 50% of a cell culture population. To determine the concentration of a given virus stock as TCID$_{50}$/ml, six 96-well plates were prepared with 2×10^3 ARPE-19 cells/well for KSHV titration and with 1.5×10^3 MEF cells/well for MHV-68 titration. A serial 10-fold dilution from 10^{-3} to 10^{-10} was prepared in triplicate in the appropriate growth medium, and each dilution was divided between two 96-well plates to infect one row (12 wells) each using 100 µl/well. After using all the dilutions, centrifugal enhancement ($1,065 \times g$, 37°C, 30 min) was applied to half of the six plates, whereas the other half was incubated at 37°C without centrifugation to obtain two different titers for each virus stock for different applications, similar to what has been described for MCMV (170). After 12-14 days (KSHV) or 6-7 days (MHV-68), the number of infected wells was determined for each dilution with focus formation as a readout and then used to calculate TCID$_{50}$/ml by the Spearman-Kärber method (171, 172).

The samples of viral replication kinetics (see 8.2.10) were titrated using the same approach, except that a single serial dilution starting from 10^{-1} was prepared for each biological replicate and in duplicate for the input. Centrifugal enhancement was used for KSHV titration.

8.2.9 Viral infection

To ensure a standardized approach suitable for comparisons, viral infections were performed using a defined multiplicity of infection (MOI), i.e., the number of viral particles available to infect a given cell. If required, centrifugal enhancement ($1,065 \times g$, 37°C, 30 min) (170) was used to increase infection efficiency. The volume of virus stock needed to infect cells at a given MOI was calculated using the following formula:

$$virus\ stock\ volume\ (ml) = \frac{number\ of\ cells\ \times\ MOI}{TCID50/ml}$$

For KSHV$_{Lyt}$, an MOI of 0.1 was found to be sufficient for infecting almost all the cells, suggesting that focus-forming units, the readout used in virus titration described in 8.2.8, are an underestimate of KSHV$_{Lyt}$ infectivity. Hence, a suitable MOI for KSHV$_{Lyt}$ infection experiments differs from that required for naturally lytic replicating viruses.

8.2.10 Viral replication kinetics

For MHV-68 multistep replication kinetics, 3.5×10^4 MEF cells/well on a 12-well plate were infected at MOI 0.01 with either MHV-68 ORF61-FLAG or ORF61*mut*IPAM-FLAG in triplicate. The input virus was removed 4 h later, the cells were washed with PBS and fresh medium added. Supernatants were

harvested at different times post-infection, cells washed with PBS and fresh medium added. Supernatants were stored at -80°C and titrated on MEF cells (see 8.2.8).

For KSHV multistep replication kinetics, 1.5×10^4 TetOn A3B RPE-1 cells/well on a 24-well plate were infected at MOI 0.025 with either KSHV mNeon-ORF61 or mNeon-ORF61*mut*IPAM in triplicate using centrifugal enhancement ($1,065 \times g$, 37°C, 30 min). Input virus was removed 4 h later, cells washed with PBS and fresh medium containing 1 µM dNTPs added. To induce A3B expression, cells were treated with 1 µg/ml doxycycline. Supernatants were harvested at different times post-infection, cells washed with PBS and fresh, dNTP-containing medium with or without doxycycline added. Supernatants were stored at -80°C and titrated on ARPE-19 cells (see 8.2.8).

8.3 Biochemistry

8.3.1 Cell lysate fractionation

Cells were harvested in a mild NP40 lysis buffer supplemented with an EDTA-free cOmplete Mini protease inhibitor cocktail (Roche). The samples were lysed for 30 min on ice with repeated swirling. Lysates were separated into detergent-soluble and -insoluble fractions by centrifugation ($21,000 \times g$, 4°C, 15 min). The soluble supernatant was boiled for 10 min at 95°C in 5x SDS-PAGE sample buffer and the insoluble cell pellet in 2x SDS-PAGE sample buffer.

8.3.2 SDS polyacrylamide gel electrophoresis (SDS-PAGE) and immunoblot

For protein detection in cell lysates, proteins were first denatured by boiling the lysates for 10 min at 95°C in SDS-PAGE sample buffer containing sodium dodecyl sulfate (SDS) and 2-mercaptoethanol. To separate the proteins according to their molecular weight, the denatured samples were loaded on a polyacrylamide gel consisting of a 4% Tris-HCl stacking gel and a 10% Tris-HCl resolving gel (see 7.9.3 for gel composition). The samples were run together with PageRuler™ Prestained Protein Ladder (Thermo Fisher Scientific) in 1x running buffer at 80-100 V for 3 h or until sufficient separation. Prior to protein transfer, the gel was equilibrated by 5 min incubation in transfer buffer. The proteins were then transferred from the gel onto Amersham™ Protran™ Premium 0.2 µm nitrocellulose membrane (Cytiva) by semi-dry blotting at 0.1 A/gel for 75 min using Trans-Blot Turbo Transfer System (Bio-Rad). After transfer, the membrane was washed shortly in 1x TBS-T, blocked by 45 min incubation in 5% (w/v) skimmed milk in 1x TBS-T at RT to prevent unspecific binding of the antibody and then incubated with the primary antibody diluted in 5% milk/TBS-T with gentle rotation at 4°C overnight. If necessary, the membrane was cut to enable simultaneous incubation with different antibodies. On the following day, the membrane was washed for 3 x 5 min in 1x TBS-T, incubated with the horseradish peroxidase (HRP)-coupled secondary antibody diluted in 5% milk/TBS-T for 45 min at RT and then washed again for 3 x 5 min in 1x TBS-T. Proteins were visualized with Amersham™ enhanced chemiluminescence (ECL) detection reagent (Cytiva) supplemented with 5-10% Lumigen ECL Ultra TMA-6 (Lumigen) for increased detection sensitivity,

if required. Chemiluminescence was detected using the Fusion Capture Advance FX7 16.15 camera system (Peqlab).

8.3.3 Immunoprecipitation

Three wells of a 6-well plate with 1.8 x 10^5 TetOn A3B or A3G RPE-1 cells/well were infected with either KSHV mNeon-ORF61, KSHV mNeon-ORF61*mut*IPAM (MOI 0.1) or MHV-68 ORF61-mNeon (MOI 5) using centrifugal enhancement (1,065 × g, 37°C, 30 min). A3B or A3G expression was induced 16 hpi with 1 µg/ml doxycycline. At 40 hpi, cells were harvested in a total of 200 µl RIPA lysis buffer supplemented with a protease inhibitor cocktail and 25 U/ml Benzonase® endonuclease (Merck). The samples were lysed 30 min on ice with repeated swirling. Insoluble material was pelleted by centrifugation (17,000 × g, 4°C, 10 min) and discarded. 300 µl dilution buffer was then added to the supernatant and 40 µl of the diluted supernatant boiled in 5x SDS-PAGE sample buffer as lysate control. The remaining supernatant was incubated with binding control agarose beads (Proteintech) with gentle rotation at 4°C for 1 h to avoid unspecific binding to the beads. After pre-clearing, the supernatants were used for pulldown with mNeonGreen-Trap agarose beads (Proteintech) as per manufacturer's instructions. After 1 h incubation at 4°C with gentle rotation, the beads were washed once with RIPA buffer and twice with minimal washing buffer. The proteins were eluted in 80 µl 2x SDS-PAGE sample buffer by boiling for 5 min at 95°C. The precipitated proteins and the corresponding lysate controls were analyzed by SDS-PAGE and immunoblot (see 8.3.2).

For immunoprecipitation in transfection, 2.5x10^6 HEK-293A cells were transfected with 3 µg of HA-tagged R1 expression plasmids and 3 µg of FLAG-tagged human RIPK1, murine RIPK1 or murine NEMO expression plasmids (see 8.2.2). After 24 h, the samples were collected in 1 ml NP40 lysis buffer supplemented with a protease inhibitor cocktail and lysed for 30 min on ice with repeated swirling. The insoluble material was pelleted by centrifugation (21,000 × g, 4°C, 15 min) and discarded. 100 µl of the supernatant was boiled in 5x SDS-PAGE sample buffer as lysate control. The remaining supernatant was incubated with rProtein A Sepharose (PAS) Fast Flow resin beads (Cytiva) with gentle rotation at 4°C for 2 h to avoid unspecific binding to the beads. The pre-cleared supernatant was then incubated using a rabbit anti-HA antibody with gentle rotation at 4°C overnight followed by 2.5 h incubation with PAS beads to precipitate the HA-tagged R1 proteins. The beads were washed three times with washing buffer 1, twice with washing buffer 2 and once with washing buffer 3. The proteins were then eluted in 100 µl 2x SDS-PAGE sample buffer by boiling and analyzed together with the corresponding lysate controls by SDS-PAGE and immunoblot (see 8.3.2).

8.4 Microscopy

8.4.1 Immunofluorescence

3.5×10^4 U2OS or HEK-293A cells were seeded on a μ-Slide 8 well (ibidi) coated with 0.4% gelatin and transfected with 400 ng of expression plasmids, as described in 8.2.2. After 24 h, the cells were washed twice with PBS and fixed with 4% paraformaldehyde (PFA) for 20 min. Fixing and immunofluorescence staining were carried out at RT, and the cells were washed twice with PBS between each step. To reduce autofluorescence, free aldehyde groups were neutralized with 50 mM NH_4Cl for 10 min. Cells were then permeabilized with 0.5% Triton X-100 for 10 min. To avoid unspecific binding of antibodies, the samples were blocked in TBS-BG blocking buffer for 30 min before incubating first with primary antibodies diluted in PBS for 1 h and then for 30-45 min with fluorophore-conjugated secondary antibodies (Thermo Fisher Scientific) or rhodamine phalloidin and Hoechst 33342 (both Invitrogen) diluted in PBS as per manufacturer's instructions. After the final wash, the cells were kept in PBS at 4°C and protected from light until imaging. Fluorescence images were acquired with a Nikon Ti2-based A1 confocal laser scanning microscope (cLSM) using a 1.4 NA 60x Plan Apo objective or a Nikon Ti2-based spinning disk system equipped with a Yokogawa CSU-W1 confocal spinning disk unit and a 1.45 NA 100x Plan Apo objective.

For KSHV infection experiments, 4×10^4 (ARPE-19 or TIME) or 3×10^4 (HFF or TetOn A3 RPE-1) cells were seeded on a gelatin-coated μ-Slide 8 well (ibidi) and infected with KSHV at MOI 0.05 for 24, 48, or 72 h. TetOn A3 RPE-1 cells were treated with 1 μg/ml doxycycline at 16 hpi to induce A3B or A3G expression. For MHV-68 infection experiments, 3.5×10^4 murine 10.1 fibroblasts or MEF cells were seeded on a gelatin-coated μ-Slide 8 well (ibidi) and infected with MHV-68 at MOI 2 for 6, 8, or 24 h. The cells were fixed, stained and imaged as described above.

8.4.2 Fluorescence recovery after photobleaching (FRAP)

3.5×10^4 U2OS cells were seeded on a gelatin-coated μ-Dish 35 mm Quad (ibidi) and transfected with 400 ng of mCherry-tagged KSHV ORF61, MHV-68 ORF61 or nucleolin, as described in 8.2.2. After 24 h, fluorescence was detected by live-cell imaging with a Nikon A1 cLSM using a 1.4 NA 60x Plan Apo objective. FRAP analysis of at least ten different cells per sample was performed essentially as described (120). Briefly, areas of 1 μm diameter within mCherry-positive structures were half-bleached for 2 s with a 563 nm laser and the recovery of fluorescence recorded at 2 frames per second for 6 min. Fluorescence intensity of an unbleached area within each cell was recorded under the same conditions for calculation of the relative fluorescence intensity (RFI). The average intensity for each time point was then normalized to the background and the RFI over time calculated as described (173).

8.4.3 Correlative light and electron microscopy (CLEM)

4×10^4 ARPE-19 or MEF cells were seeded on a gelatin-coated μ-Dish 35 mm high Grid-500 (ibidi) and infected with KSHV mNeon-ORF61 (MOI 0.05) or MHV-68 ORF61-mNeon (MOI 2), respectively. At 40 hpi (KSHV) or 20 hpi (MHV-68), the cells were fixed with 4% PFA for 20 min at RT and the nuclei stained with Hoechst 33342 for 10 min. Fluorescent Z-stacks were acquired with a Nikon A1 cLSM using a 0.75 NA 20x Plan Apo VC objective, deconvolved with Nikon NIS-Elements and used for correlation with transmission EM images. Samples were processed for EM as described (174), and at least ten aggregates per sample were analyzed. EM sample processing and imaging were performed by Carola Schneider and Rudolph Reimer (LIV).

8.4.4 Quantitative image analysis

KSHV ORF61 colocalization with A3s was quantified using the ImageJ Colocalization Threshold plugin, and the Pearson's correlation coefficient (r) was calculated for each condition ($n = 10$). The r coefficient gives a score of 1 for perfect colocalization and 0 for no colocalization. For statistical analysis, an unpaired two-tailed Student's *t*-test was performed.

For quantification of the nuclear A3B fluorescence intensity (%), nuclear and cytoplasmic outlines of the cells ($n = 12$) were defined by thresholding the Hoechst and A3 signal intensities, respectively. The mean nuclear and total A3B intensities were then calculated, corrected for background and multiplied by the area of the corresponding outlines to obtain the sum fluorescence intensity of the selected area. The sum A3B intensity of the whole cell was defined as 100% for calculation of the nuclear intensity. Quantitative image analysis was performed by Enrico Caragliano (CSSB/LIV).

8.5 Liquid chromatography-tandem mass spectrometry (LC-MS/MS)

8.5.1 Infection and sample collection

A 6-well plate with 2.5×10^5 MEF cells/well was infected with either MHV-68 ORF61- or ORF61*mut*IPAM-FLAG at MOI 3 in five replicates. After 24 h, the cells were lysed in NP40 lysis buffer supplemented with a protease inhibitor cocktail, and the lysates separated into soluble and insoluble fractions, as described in 8.3.1. The soluble fractions were discarded, and the pellets washed once with PBS and then dissolved in 2x SDS-PAGE sample buffer without bromophenol blue. The samples were sonicated for 8 x 15 s (Bioruptor® Plus UCD-200, Diagenode) to improve dissolving, boiled for 10 min at 95°C and processed for LC-MS/MS (see 8.5.2).

8.5.2 Sample processing

LC-MS/MS sample processing, measurement and statistical analysis were performed by Bente Siebels, Antonia Gocke, and Hartmut Schlüter (Core Facility Mass Spectrometric Proteomics, University Medical Center Hamburg-Eppendorf).

Protein concentration of the samples was determined with the bicinchoninic acid assay (BCA) Protein Assay Kit (Thermo Fisher Scientific), and the samples were diluted to 0.4 µg/µl. Disulfide bonds were reduced in 10 mM dithiothreitol for 30 min at 56°C and alkylated in the presence of 20 mM iodoacetamide for 30 min at 37°C in the dark. Samples were then dissolved to a concentration of 70% acetonitrile (ACN) and mixed with 2 µl of Sera-Mag™ carboxylate-modified magnetic beads (Cytiva) at a 1:1 ratio in methanol/LC-MS grade water following the single-pot, solid-phase enhanced sample preparation (SP3)-protocol workflow (175). Samples were shaken at 1400 rpm for 18 min at RT, the supernatant was removed on a magnetic rack and the beads washed twice with 100% ACN and twice with 70% ethanol. After resuspension in 50 mM ammonium bicarbonate, an overnight trypsin (sequencing grade, Promega) digestion was performed at a 1:100 (enzyme : protein) ratio at 37°C and shaking at 1400 rpm. Tryptic peptides were bound to the beads by adding 95% ACN and shaking for 10 min at 1400 rpm at RT. The supernatant was then removed and the beads were washed twice with 100% ACN. Peptides were eluted in 2% DMSO in 1% formic acid (FA). The supernatant was dried in a vacuum centrifuge and stored at -20°C until further use.

8.5.3 LC-MS/MS measurement

Chromatographic separation of peptides was performed on a Dionex UltiMate 3000 UHPLC system (Thermo Fisher Scientific) using a two-buffer system (buffer A: 0.1% FA in H_2O, buffer B: 0.1% FA in ACN). Attached to the UHPLC was a C18 nanoViper 100 µm x 20 mm peptide trap with 100 Å pore size and 5 µm particle size (Thermo Fisher Scientific) for online desalting and purification followed by a 25 cm nanoEase BEH C18 reversed-phase 75 µm x 250 mm column with 130 Å pore size and 1.7 µm particle size (Waters). Peptides were separated using an 80 min method by linearly increasing ACN concentration from 2% to 30% over 60 minutes.

MS/MS measurements were performed on an Orbitrap Fusion quadrupole-ion-trap-orbitrap MS (Thermo Fisher Scientific). Eluting peptides were ionized using a nano-electrospray ionization source (nano-ESI) with a spray voltage of 1,800 V and analyzed in data-dependent acquisition (DDA) mode. For each MS1 scan, ions were accumulated for a maximum of 120 ms or until a charge density of 2×10^5 ions (AGC Target) was reached. Fourier transform-based mass analysis of the orbitrap mass analyzer data was performed covering a mass range of m/z 400 – 1,300 with a resolution of 120,000 at m/z = 200. Peptides with charge states between 2+ - 5+ above an intensity threshold of 1,000 were isolated within a m/z 1.6 isolation window in Top Speed mode for 3 s from each precursor scan and fragmented with a 30% normalized collision energy using higher energy collisional dissociation (HCD). MS2 scan was performed using an ion trap mass analyzer at a rapid scan rate starting at m/z 120, and the ions were accumulated for 60 ms or to an AGC target of 1×10^5. Already fragmented peptides were excluded for 30 s.

8.5.4 LC-MS/MS data analysis

LC-MS/MS data were searched against a *Mus musculus* Swiss-Prot canonical database obtained in December 2022 and a TrEMBL Murid herpesvirus 4 (MuHV-4) database obtained in July 2023, thereby using a Sequest algorithm integrated into the Proteome Discoverer software V3.0.0.757 (Thermo Fisher Scientific). Carbamidomethylation was set as a fixed modification for cysteine residues. The oxidation of methionine as well as acetylation of the protein N-terminus were allowed as variable modifications. A maximum number of two missing tryptic cleavages was set. Peptides between 6 and 144 amino acids were considered. A strict cut-off (FDR < 0.01) was set for peptide and protein identification. Quantification was performed using the Minora algorithm integrated into Proteome Discoverer.

The Perseus software platform (V2.0.11.0) (176) was used for statistical analysis. Obtained protein abundances were $\log_2$-transformed and normalized by column-median normalization. Principal component analysis was performed without missing values (1028 proteins). Student's *t*-test with Benjamini Hochberg FDR-correction was applied on proteins found in at least 30% of all samples (1455 proteins). Cut-offs for significance were set to *P* value ≤ 0.05, q-value ≤ 0.05 and a $\log_2$ fold change ≥ 1. Visualizations were performed with R Studio. Proteins selected for orthogonal validation had ≥ 3 unique peptides.

9. Bibliography

1.   Gatherer D, Depledge DP, Hartley CA, Szpara ML, Vaz PK, Benko M, Brandt CR, Bryant NA, Dastjerdi A, Doszpoly A, Gompels UA, Inoue N, Jarosinski KW, Kaul R, Lacoste V, Norberg P, Origgi FC, Orton RJ, Pellett PE, Schmid DS, Spatz SJ, Stewart JP, Trimpert J, Waltzek TB, Davison AJ. 2021. ICTV Virus Taxonomy Profile: Herpesviridae 2021. J Gen Virol 102.
2.   Pellett PE, Roizman B. 2013. *Herpesviridae*, p 1802-1822. *In* Cohen JI, Griffin DE, Howley PM, Knipe DM, Lamb RA, Martin MA, Racaniello VR, Roizman B (ed), Fields Virology 6th Edition. Lippincott Williams & Wilkins, Philadelphia, PA, USA.
3.   Zheng HH, Fu PF, Chen HY, Wang ZY. 2022. Pseudorabies Virus: From Pathogenesis to Prevention Strategies. Viruses 14.
4.   Boehmer PE, Nimonkar AV. 2003. Herpes virus replication. IUBMB Life 55:13-22.
5.   Coen DM, Schaffer PA. 2003. Antiherpesvirus drugs: a promising spectrum of new drugs and drug targets. Nat Rev Drug Discov 2:278-88.
6.   Longnecker R, Neipel F. 2007. Introduction to the human γ-herpesviruses. *In* Arvin A, Campadelli-Fiume G, Mocarski E, Moore PS, Roizman B, Whitley R, Yamanishi K (ed), Human Herpesviruses: Biology, Therapy, and Immunoprophylaxis. Cambridge University Press, Cambridge.
7.   Young LS, Yap LF, Murray PG. 2016. Epstein-Barr virus: more than 50 years old and still providing surprises. Nat Rev Cancer 16:789-802.
8.   Longnecker RM, Kieff E, Cohen JI. 2013. Epstein-Barr virus, p 1898-1959. *In* Cohen JI, Griffin DE, Howley PM, Knipe DM, Lamb RA, Martin MA, Racaniello VR, Roizman B (ed), Fields Virology 6th Edition. Lippincott Williams & Wilkins, Philadelphia, PA, USA.
9.   Babcock GJ, Decker LL, Volk M, Thorley-Lawson DA. 1998. EBV persistence in memory B cells in vivo. Immunity 9:395-404.
10.   zur Hausen H, Schulte-Holthausen H, Klein G, Henle W, Henle G, Clifford P, Santesson L. 1970. EBV DNA in biopsies of Burkitt tumours and anaplastic carcinomas of the nasopharynx. Nature 228:1056-8.
11.   Weiss LM, Movahed LA, Warnke RA, Sklar J. 1989. Detection of Epstein-Barr viral genomes in Reed-Sternberg cells of Hodgkin's disease. N Engl J Med 320:502-6.
12.   Shibata D, Tokunaga M, Uemura Y, Sato E, Tanaka S, Weiss LM. 1991. Association of Epstein-Barr virus with undifferentiated gastric carcinomas with intense lymphoid infiltration. Lymphoepithelioma-like carcinoma. Am J Pathol 139:469-74.
13.   Chang Y, Cesarman E, Pessin MS, Lee F, Culpepper J, Knowles DM, Moore PS. 1994. Identification of herpesvirus-like DNA sequences in AIDS-associated Kaposi's sarcoma. Science 266:1865-9.
14.   Cesarman E, Chang Y, Moore PS, Said JW, Knowles DM. 1995. Kaposi's sarcoma-associated herpesvirus-like DNA sequences in AIDS-related body-cavity-based lymphomas. N Engl J Med 332:1186-91.
15.   Soulier J, Grollet L, Oksenhendler E, Cacoub P, Cazals-Hatem D, Babinet P, d'Agay MF, Clauvel JP, Raphael M, Degos L, et al. 1995. Kaposi's sarcoma-associated herpesvirus-like DNA sequences in multicentric Castleman's disease. Blood 86:1276-80.
16.   Wen KW, Damania B. 2010. Kaposi sarcoma-associated herpesvirus (KSHV): molecular biology and oncogenesis. Cancer Lett 289:140-50.
17.   Lagunoff M, Ganem D. 1997. The structure and coding organization of the genomic termini of Kaposi's sarcoma-associated herpesvirus. Virology 236:147-54.
18.   Russo JJ, Bohenzky RA, Chien MC, Chen J, Yan M, Maddalena D, Parry JP, Peruzzi D, Edelman IS, Chang Y, Moore PS. 1996. Nucleotide sequence of the Kaposi sarcoma-associated herpesvirus (HHV8). Proc Natl Acad Sci U S A 93:14862-7.
19.   Martin JN. 2007. The epidemiology of KSHV and its association with malignant disease. *In* Arvin A, Campadelli-Fiume G, Mocarski E, Moore PS, Roizman B, Whitley R, Yamanishi K (ed), Human Herpesviruses: Biology, Therapy, and Immunoprophylaxis. Cambridge University Press, Cambridge.
20.   Pauk J, Huang ML, Brodie SJ, Wald A, Koelle DM, Schacker T, Celum C, Selke S, Corey L. 2000. Mucosal shedding of human herpesvirus 8 in men. N Engl J Med 343:1369-77.

21.   Ambroziak JA, Blackbourn DJ, Herndier BG, Glogau RG, Gullett JH, McDonald AR, Lennette ET, Levy JA. 1995. Herpes-like sequences in HIV-infected and uninfected Kaposi's sarcoma patients. Science 268:582-3.

22.   Blasig C, Zietz C, Haar B, Neipel F, Esser S, Brockmeyer NH, Tschachler E, Colombini S, Ensoli B, Sturzl M. 1997. Monocytes in Kaposi's sarcoma lesions are productively infected by human herpesvirus 8. J Virol 71:7963-8.

23.   Dupin N, Fisher C, Kellam P, Ariad S, Tulliez M, Franck N, van Marck E, Salmon D, Gorin I, Escande JP, Weiss RA, Alitalo K, Boshoff C. 1999. Distribution of human herpesvirus-8 latently infected cells in Kaposi's sarcoma, multicentric Castleman's disease, and primary effusion lymphoma. Proc Natl Acad Sci U S A 96:4546-51.

24.   Ballestas ME, Chatis PA, Kaye KM. 1999. Efficient persistence of extrachromosomal KSHV DNA mediated by latency-associated nuclear antigen. Science 284:641-4.

25.   Garber AC, Hu J, Renne R. 2002. Latency-associated nuclear antigen (LANA) cooperatively binds to two sites within the terminal repeat, and both sites contribute to the ability of LANA to suppress transcription and to facilitate DNA replication. J Biol Chem 277:27401-11.

26.   Sun R, Lin SF, Gradoville L, Yuan Y, Zhu F, Miller G. 1998. A viral gene that activates lytic cycle expression of Kaposi's sarcoma-associated herpesvirus. Proc Natl Acad Sci U S A 95:10866-71.

27.   Renne R, Zhong W, Herndier B, McGrath M, Abbey N, Kedes D, Ganem D. 1996. Lytic growth of Kaposi's sarcoma-associated herpesvirus (human herpesvirus 8) in culture. Nat Med 2:342-6.

28.   Yu Y, Black JB, Goldsmith CS, Browning PJ, Bhalla K, Offermann MK. 1999. Induction of human herpesvirus-8 DNA replication and transcription by butyrate and TPA in BCBL-1 cells. J Gen Virol 80 (Pt 1):83-90.

29.   Blaskovic D, Stancekova M, Svobodova J, Mistrikova J. 1980. Isolation of five strains of herpesviruses from two species of free living small rodents. Acta Virol 24:468.

30.   Ciampor F, Stancekova M, Blaskovic D. 1981. Electron microscopy of rabbit embryo fibroblasts infected with herpesvirus isolates from Clethrionomys glareolus and Apodemus flavicollis. Acta Virol 25:101-7.

31.   Efstathiou S, Ho YM, Minson AC. 1990. Cloning and molecular characterization of the murine herpesvirus 68 genome. J Gen Virol 71 (Pt 6):1355-64.

32.   Virgin HWt, Latreille P, Wamsley P, Hallsworth K, Weck KE, Dal Canto AJ, Speck SH. 1997. Complete sequence and genomic analysis of murine gammaherpesvirus 68. J Virol 71:5894-904.

33.   Sunil-Chandra NP, Efstathiou S, Arno J, Nash AA. 1992. Virological and pathological features of mice infected with murine gamma-herpesvirus 68. J Gen Virol 73 (Pt 9):2347-56.

34.   Sunil-Chandra NP, Efstathiou S, Nash AA. 1992. Murine gammaherpesvirus 68 establishes a latent infection in mouse B lymphocytes in vivo. J Gen Virol 73 (Pt 12):3275-9.

35.   Usherwood EJ, Ross AJ, Allen DJ, Nash AA. 1996. Murine gammaherpesvirus-induced splenomegaly: a critical role for CD4 T cells. J Gen Virol 77 (Pt 4):627-30.

36.   Sunil-Chandra NP, Arno J, Fazakerley J, Nash AA. 1994. Lymphoproliferative disease in mice infected with murine gammaherpesvirus 68. Am J Pathol 145:818-26.

37.   Svobodova J, Blaskovic D, Mistrikova J. 1982. Growth characteristics of herpesviruses isolated from free living small rodents. Acta Virol 26:256-63.

38.   Dobson CM. 2003. Protein folding and misfolding. Nature 426:884-90.

39.   Hershko A, Heller H, Elias S, Ciechanover A. 1983. Components of ubiquitin-protein ligase system. Resolution, affinity purification, and role in protein breakdown. J Biol Chem 258:8206-14.

40.   Chau V, Tobias JW, Bachmair A, Marriott D, Ecker DJ, Gonda DK, Varshavsky A. 1989. A multiubiquitin chain is confined to specific lysine in a targeted short-lived protein. Science 243:1576-83.

41.   Tanaka K. 2009. The proteasome: overview of structure and functions. Proc Jpn Acad Ser B Phys Biol Sci 85:12-36.

42.   Dice JF, Chiang HL. 1989. Peptide signals for protein degradation within lysosomes. Biochem Soc Symp 55:45-55.

43.   Dice JF. 2007. Chaperone-mediated autophagy. Autophagy 3:295-9.

44. Bandyopadhyay U, Kaushik S, Varticovski L, Cuervo AM. 2008. The chaperone-mediated autophagy receptor organizes in dynamic protein complexes at the lysosomal membrane. Mol Cell Biol 28:5747-63.

45. Tan JM, Wong ES, Kirkpatrick DS, Pletnikova O, Ko HS, Tay SP, Ho MW, Troncoso J, Gygi SP, Lee MK, Dawson VL, Dawson TM, Lim KL. 2008. Lysine 63-linked ubiquitination promotes the formation and autophagic clearance of protein inclusions associated with neurodegenerative diseases. Hum Mol Genet 17:431-9.

46. Pankiv S, Clausen TH, Lamark T, Brech A, Bruun JA, Outzen H, Overvatn A, Bjorkoy G, Johansen T. 2007. p62/SQSTM1 binds directly to Atg8/LC3 to facilitate degradation of ubiquitinated protein aggregates by autophagy. J Biol Chem 282:24131-45.

47. Kirkin V, Lamark T, Sou YS, Bjorkoy G, Nunn JL, Bruun JA, Shvets E, McEwan DG, Clausen TH, Wild P, Bilusic I, Theurillat JP, Overvatn A, Ishii T, Elazar Z, Komatsu M, Dikic I, Johansen T. 2009. A role for NBR1 in autophagosomal degradation of ubiquitinated substrates. Mol Cell 33:505-16.

48. Mizushima N, Noda T, Yoshimori T, Tanaka Y, Ishii T, George MD, Klionsky DJ, Ohsumi M, Ohsumi Y. 1998. A protein conjugation system essential for autophagy. Nature 395:395-8.

49. Kuma A, Mizushima N, Ishihara N, Ohsumi Y. 2002. Formation of the approximately 350-kDa Apg12-Apg5.Apg16 multimeric complex, mediated by Apg16 oligomerization, is essential for autophagy in yeast. J Biol Chem 277:18619-25.

50. Kabeya Y, Mizushima N, Ueno T, Yamamoto A, Kirisako T, Noda T, Kominami E, Ohsumi Y, Yoshimori T. 2000. LC3, a mammalian homologue of yeast Apg8p, is localized in autophagosome membranes after processing. EMBO J 19:5720-8.

51. Xie Z, Klionsky DJ. 2007. Autophagosome formation: core machinery and adaptations. Nat Cell Biol 9:1102-9.

52. Nakatogawa H, Ichimura Y, Ohsumi Y. 2007. Atg8, a ubiquitin-like protein required for autophagosome formation, mediates membrane tethering and hemifusion. Cell 130:165-78.

53. Mizushima N. 2007. Autophagy: process and function. Genes Dev 21:2861-73.

54. Lamark T, Johansen T. 2012. Aggrephagy: selective disposal of protein aggregates by macroautophagy. Int J Cell Biol 2012:736905.

55. Shi K, Carpenter MA, Banerjee S, Shaban NM, Kurahashi K, Salamango DJ, McCann JL, Starrett GJ, Duffy JV, Demir O, Amaro RE, Harki DA, Harris RS, Aihara H. 2017. Structural basis for targeted DNA cytosine deamination and mutagenesis by APOBEC3A and APOBEC3B. Nat Struct Mol Biol 24:131-139.

56. Iyer LM, Zhang D, Rogozin IB, Aravind L. 2011. Evolution of the deaminase fold and multiple origins of eukaryotic editing and mutagenic nucleic acid deaminases from bacterial toxin systems. Nucleic Acids Res 39:9473-97.

57. Teng B, Burant CF, Davidson NO. 1993. Molecular cloning of an apolipoprotein B messenger RNA editing protein. Science 260:1816-9.

58. Navaratnam N, Morrison JR, Bhattacharya S, Patel D, Funahashi T, Giannoni F, Teng BB, Davidson NO, Scott J. 1993. The p27 catalytic subunit of the apolipoprotein B mRNA editing enzyme is a cytidine deaminase. J Biol Chem 268:20709-12.

59. Conticello SG, Thomas CJ, Petersen-Mahrt SK, Neuberger MS. 2005. Evolution of the AID/APOBEC family of polynucleotide (deoxy)cytidine deaminases. Mol Biol Evol 22:367-77.

60. Muramatsu M, Sankaranand VS, Anant S, Sugai M, Kinoshita K, Davidson NO, Honjo T. 1999. Specific expression of activation-induced cytidine deaminase (AID), a novel member of the RNA-editing deaminase family in germinal center B cells. J Biol Chem 274:18470-6.

61. Petersen-Mahrt SK, Harris RS, Neuberger MS. 2002. AID mutates E. coli suggesting a DNA deamination mechanism for antibody diversification. Nature 418:99-103.

62. Liao W, Hong SH, Chan BH, Rudolph FB, Clark SC, Chan L. 1999. APOBEC-2, a cardiac- and skeletal muscle-specific member of the cytidine deaminase supergene family. Biochem Biophys Res Commun 260:398-404.

63. Rogozin IB, Basu MK, Jordan IK, Pavlov YI, Koonin EV. 2005. APOBEC4, a new member of the AID/APOBEC family of polynucleotide (deoxy)cytidine deaminases predicted by computational analysis. Cell Cycle 4:1281-5.

64. Conticello SG. 2008. The AID/APOBEC family of nucleic acid mutators. Genome Biol 9:229.

65.   Harris RS, Petersen-Mahrt SK, Neuberger MS. 2002. RNA editing enzyme APOBEC1 and some of its homologs can act as DNA mutators. Mol Cell 10:1247-53.

66.   Lorenzo JP, Molla L, Amro EM, Ibarra IL, Ruf S, Neber C, Gkougkousis C, Ridani J, Subramani PG, Boulais J, Harjanto D, Vonica A, Di Noia JM, Dieterich C, Zaugg JB, Papavasiliou FN. 2024. APOBEC2 safeguards skeletal muscle cell fate through binding chromatin and regulating transcription of non-muscle genes during myoblast differentiation. Proc Natl Acad Sci U S A 121:e2312330121.

67.   Conticello SG, Langlois MA, Yang Z, Neuberger MS. 2007. DNA deamination in immunity: AID in the context of its APOBEC relatives. Adv Immunol 94:37-73.

68.   Krishnan A, Iyer LM, Holland SJ, Boehm T, Aravind L. 2018. Diversification of AID/APOBEC-like deaminases in metazoa: multiplicity of clades and widespread roles in immunity. Proc Natl Acad Sci U S A 115:E3201-E3210.

69.   Jarmuz A, Chester A, Bayliss J, Gisbourne J, Dunham I, Scott J, Navaratnam N. 2002. An anthropoid-specific locus of orphan C to U RNA-editing enzymes on chromosome 22. Genomics 79:285-96.

70.   Harris RS, Bishop KN, Sheehy AM, Craig HM, Petersen-Mahrt SK, Watt IN, Neuberger MS, Malim MH. 2003. DNA deamination mediates innate immunity to retroviral infection. Cell 113:803-9.

71.   Navaratnam N, Bhattacharya S, Fujino T, Patel D, Jarmuz AL, Scott J. 1995. Evolutionary origins of apoB mRNA editing: catalysis by a cytidine deaminase that has acquired a novel RNA-binding motif at its active site. Cell 81:187-95.

72.   Bishop KN, Holmes RK, Sheehy AM, Davidson NO, Cho SJ, Malim MH. 2004. Cytidine deamination of retroviral DNA by diverse APOBEC proteins. Curr Biol 14:1392-6.

73.   Wedekind JE, Dance GS, Sowden MP, Smith HC. 2003. Messenger RNA editing in mammals: new members of the APOBEC family seeking roles in the family business. Trends Genet 19:207-16.

74.   Wichroski MJ, Robb GB, Rana TM. 2006. Human retroviral host restriction factors APOBEC3G and APOBEC3F localize to mRNA processing bodies. PLoS Pathog 2:e41.

75.   Bennett RP, Presnyak V, Wedekind JE, Smith HC. 2008. Nuclear Exclusion of the HIV-1 host defense factor APOBEC3G requires a novel cytoplasmic retention signal and is not dependent on RNA binding. J Biol Chem 283:7320-7.

76.   Land AM, Law EK, Carpenter MA, Lackey L, Brown WL, Harris RS. 2013. Endogenous APOBEC3A DNA cytosine deaminase is cytoplasmic and nongenotoxic. J Biol Chem 288:17253-60.

77.   Bogerd HP, Wiegand HL, Hulme AE, Garcia-Perez JL, O'Shea KS, Moran JV, Cullen BR. 2006. Cellular inhibitors of long interspersed element 1 and Alu retrotransposition. Proc Natl Acad Sci U S A 103:8780-5.

78.   Kinomoto M, Kanno T, Shimura M, Ishizaka Y, Kojima A, Kurata T, Sata T, Tokunaga K. 2007. All APOBEC3 family proteins differentially inhibit LINE-1 retrotransposition. Nucleic Acids Res 35:2955-64.

79.   LaRue RS, Jonsson SR, Silverstein KA, Lajoie M, Bertrand D, El-Mabrouk N, Hotzel I, Andresdottir V, Smith TP, Harris RS. 2008. The artiodactyl APOBEC3 innate immune repertoire shows evidence for a multi-functional domain organization that existed in the ancestor of placental mammals. BMC Mol Biol 9:104.

80.   Sheehy AM, Gaddis NC, Choi JD, Malim MH. 2002. Isolation of a human gene that inhibits HIV-1 infection and is suppressed by the viral Vif protein. Nature 418:646-50.

81.   Yu X, Yu Y, Liu B, Luo K, Kong W, Mao P, Yu XF. 2003. Induction of APOBEC3G ubiquitination and degradation by an HIV-1 Vif-Cul5-SCF complex. Science 302:1056-60.

82.   Sheehy AM, Gaddis NC, Malim MH. 2003. The antiretroviral enzyme APOBEC3G is degraded by the proteasome in response to HIV-1 Vif. Nat Med 9:1404-7.

83.   Wiegand HL, Doehle BP, Bogerd HP, Cullen BR. 2004. A second human antiretroviral factor, APOBEC3F, is suppressed by the HIV-1 and HIV-2 Vif proteins. EMBO J 23:2451-8.

84.   Zheng YH, Irwin D, Kurosu T, Tokunaga K, Sata T, Peterlin BM. 2004. Human APOBEC3F is another host factor that blocks human immunodeficiency virus type 1 replication. J Virol 78:6073-6.

85.   Hultquist JF, Lengyel JA, Refsland EW, LaRue RS, Lackey L, Brown WL, Harris RS. 2011. Human and rhesus APOBEC3D, APOBEC3F, APOBEC3G, and APOBEC3H demonstrate a conserved capacity to restrict Vif-deficient HIV-1. J Virol 85:11220-34.

86.   Turelli P, Mangeat B, Jost S, Vianin S, Trono D. 2004. Inhibition of hepatitis B virus replication by APOBEC3G. Science 303:1829.

87.   Suspene R, Guetard D, Henry M, Sommer P, Wain-Hobson S, Vartanian JP. 2005. Extensive editing of both hepatitis B virus DNA strands by APOBEC3 cytidine deaminases in vitro and in vivo. Proc Natl Acad Sci U S A 102:8321-6.

88.   Lucifora J, Xia Y, Reisinger F, Zhang K, Stadler D, Cheng X, Sprinzl MF, Koppensteiner H, Makowska Z, Volz T, Remouchamps C, Chou WM, Thasler WE, Huser N, Durantel D, Liang TJ, Munk C, Heim MH, Browning JL, Dejardin E, Dandri M, Schindler M, Heikenwalder M, Protzer U. 2014. Specific and nonhepatotoxic degradation of nuclear hepatitis B virus cccDNA. Science 343:1221-8.

89.   Chen H, Lilley CE, Yu Q, Lee DV, Chou J, Narvaiza I, Landau NR, Weitzman MD. 2006. APOBEC3A is a potent inhibitor of adeno-associated virus and retrotransposons. Curr Biol 16:480-5.

90.   Narvaiza I, Linfesty DC, Greener BN, Hakata Y, Pintel DJ, Logue E, Landau NR, Weitzman MD. 2009. Deaminase-independent inhibition of parvoviruses by the APOBEC3A cytidine deaminase. PLoS Pathog 5:e1000439.

91.   Vartanian JP, Guetard D, Henry M, Wain-Hobson S. 2008. Evidence for editing of human papillomavirus DNA by APOBEC3 in benign and precancerous lesions. Science 320:230-3.

92.   Peretti A, Geoghegan EM, Pastrana DV, Smola S, Feld P, Sauter M, Lohse S, Ramesh M, Lim ES, Wang D, Borgogna C, FitzGerald PC, Bliskovsky V, Starrett GJ, Law EK, Harris RS, Killian JK, Zhu J, Pineda M, Meltzer PS, Boldorini R, Gariglio M, Buck CB. 2018. Characterization of BK Polyomaviruses from Kidney Transplant Recipients Suggests a Role for APOBEC3 in Driving In-Host Virus Evolution. Cell Host Microbe 23:628-635 e7.

93.   Bogerd HP, Wiegand HL, Doehle BP, Lueders KK, Cullen BR. 2006. APOBEC3A and APOBEC3B are potent inhibitors of LTR-retrotransposon function in human cells. Nucleic Acids Res 34:89-95.

94.   Okeoma CM, Lovsin N, Peterlin BM, Ross SR. 2007. APOBEC3 inhibits mouse mammary tumour virus replication in vivo. Nature 445:927-30.

95.   MacMillan AL, Kohli RM, Ross SR. 2013. APOBEC3 inhibition of mouse mammary tumor virus infection: the role of cytidine deamination versus inhibition of reverse transcription. J Virol 87:4808-17.

96.   Takeda E, Tsuji-Kawahara S, Sakamoto M, Langlois MA, Neuberger MS, Rada C, Miyazawa M. 2008. Mouse APOBEC3 restricts friend leukemia virus infection and pathogenesis in vivo. J Virol 82:10998-1008.

97.   Santiago ML, Montano M, Benitez R, Messer RJ, Yonemoto W, Chesebro B, Hasenkrug KJ, Greene WC. 2008. Apobec3 encodes Rfv3, a gene influencing neutralizing antibody control of retrovirus infection. Science 321:1343-6.

98.   Petljak M, Dananberg A, Chu K, Bergstrom EN, Striepen J, von Morgen P, Chen Y, Shah H, Sale JE, Alexandrov LB, Stratton MR, Maciejowski J. 2022. Mechanisms of APOBEC3 mutagenesis in human cancer cells. Nature 607:799-807.

99.   Burns MB, Lackey L, Carpenter MA, Rathore A, Land AM, Leonard B, Refsland EW, Kotandeniya D, Tretyakova N, Nikas JB, Yee D, Temiz NA, Donohue DE, McDougle RM, Brown WL, Law EK, Harris RS. 2013. APOBEC3B is an enzymatic source of mutation in breast cancer. Nature 494:366-70.

100.   Burns MB, Temiz NA, Harris RS. 2013. Evidence for APOBEC3B mutagenesis in multiple human cancers. Nat Genet 45:977-83.

101.   Starrett GJ, Luengas EM, McCann JL, Ebrahimi D, Temiz NA, Love RP, Feng Y, Adolph MB, Chelico L, Law EK, Carpenter MA, Harris RS. 2016. The DNA cytosine deaminase APOBEC3H haplotype I likely contributes to breast and lung cancer mutagenesis. Nat Commun 7:12918.

102.   Reichard P, Ehrenberg A. 1983. Ribonucleotide reductase--a radical enzyme. Science 221:514-9.

103.   Nordlund P, Reichard P. 2006. Ribonucleotide reductases. Annu Rev Biochem 75:681-706.

104. Reichard P. 1993. From RNA to DNA, why so many ribonucleotide reductases? Science 260:1773-7.

105. Uhlin U, Eklund H. 1994. Structure of ribonucleotide reductase protein R1. Nature 370:533-9.

106. Jacobson JG, Leib DA, Goldstein DJ, Bogard CL, Schaffer PA, Weller SK, Coen DM. 1989. A herpes simplex virus ribonucleotide reductase deletion mutant is defective for productive acute and reactivatable latent infections of mice and for replication in mouse cells. Virology 173:276-83.

107. Idowu AD, Fraser-Smith EB, Poffenberger KL, Herman RC. 1992. Deletion of the herpes simplex virus type 1 ribonucleotide reductase gene alters virulence and latency in vivo. Antiviral Res 17:145-56.

108. Sun Y, Conner J. 1999. The U28 ORF of human herpesvirus-7 does not encode a functional ribonucleotide reductase R1 subunit. J Gen Virol 80 (Pt 10):2713-2718.

109. Patrone M, Percivalle E, Secchi M, Fiorina L, Pedrali-Noy G, Zoppe M, Baldanti F, Hahn G, Koszinowski UH, Milanesi G, Gallina A. 2003. The human cytomegalovirus UL45 gene product is a late, virion-associated protein and influences virus growth at low multiplicities of infection. J Gen Virol 84:3359-3370.

110. Lembo D, Donalisio M, Hofer A, Cornaglia M, Brune W, Koszinowski U, Thelander L, Landolfo S. 2004. The ribonucleotide reductase R1 homolog of murine cytomegalovirus is not a functional enzyme subunit but is required for pathogenesis. J Virol 78:4278-88.

111. Bresnahan WA, Boldogh I, Thompson EA, Albrecht T. 1996. Human cytomegalovirus inhibits cellular DNA synthesis and arrests productively infected cells in late G1. Virology 224:150-60.

112. Dittmer D, Mocarski ES. 1997. Human cytomegalovirus infection inhibits G1/S transition. J Virol 71:1629-34.

113. Wiebusch L, Hagemeier C. 1999. Human cytomegalovirus 86-kilodalton IE2 protein blocks cell cycle progression in G(1). J Virol 73:9274-83.

114. Muscolino E, Luoto LM, Brune W. 2021. Viral Induced Protein Aggregation: A Mechanism of Immune Evasion. Int J Mol Sci 22.

115. Luoto LM, Caragliano E, Schneider C, Reimer R, Brune W. 2025. Kaposi's sarcoma-associated herpesvirus ORF61 protein sequesters APOBEC3B in filamentous aggregates. J Virol doi:10.1128/jvi.00789-25:e0078925.

116. Brune W, Menard C, Heesemann J, Koszinowski UH. 2001. A ribonucleotide reductase homolog of cytomegalovirus and endothelial cell tropism. Science 291:303-5.

117. Mack C, Sickmann A, Lembo D, Brune W. 2008. Inhibition of proinflammatory and innate immune signaling pathways by a cytomegalovirus RIP1-interacting protein. Proc Natl Acad Sci U S A 105:3094-9.

118. Upton JW, Kaiser WJ, Mocarski ES. 2008. Cytomegalovirus M45 cell death suppression requires receptor-interacting protein (RIP) homotypic interaction motif (RHIM)-dependent interaction with RIP1. J Biol Chem 283:16966-70.

119. Fliss PM, Jowers TP, Brinkmann MM, Holstermann B, Mack C, Dickinson P, Hohenberg H, Ghazal P, Brune W. 2012. Viral mediated redirection of NEMO/IKKgamma to autophagosomes curtails the inflammatory cascade. PLoS Pathog 8:e1002517.

120. Muscolino E, Schmitz R, Loroch S, Caragliano E, Schneider C, Rizzato M, Kim YH, Krause E, Juranic Lisnic V, Sickmann A, Reimer R, Ostermann E, Brune W. 2020. Herpesviruses induce aggregation and selective autophagy of host signalling proteins NEMO and RIPK1 as an immune-evasion mechanism. Nat Microbiol 5:331-342.

121. Lembo D, Brune W. 2009. Tinkering with a viral ribonucleotide reductase. Trends Biochem Sci 34:25-32.

122. Huang Z, Wu SQ, Liang Y, Zhou X, Chen W, Li L, Wu J, Zhuang Q, Chen C, Li J, Zhong CQ, Xia W, Zhou R, Zheng C, Han J. 2015. RIP1/RIP3 binding to HSV-1 ICP6 initiates necroptosis to restrict virus propagation in mice. Cell Host Microbe 17:229-42.

123. Cheng AZ, Yockteng-Melgar J, Jarvis MC, Malik-Soni N, Borozan I, Carpenter MA, McCann JL, Ebrahimi D, Shaban NM, Marcon E, Greenblatt J, Brown WL, Frappier L, Harris RS. 2019. Epstein-Barr virus BORF2 inhibits cellular APOBEC3B to preserve viral genome integrity. Nat Microbiol 4:78-88.

124. Shaban NM, Yan R, Shi K, Moraes SN, Cheng AZ, Carpenter MA, McLellan JS, Yu Z, Harris RS. 2022. Cryo-EM structure of the EBV ribonucleotide reductase BORF2 and mechanism of APOBEC3B inhibition. Sci Adv 8:eabm2827.

125. Moraes SN, Becker JT, Moghadasi SA, Shaban NM, Auerbach AA, Cheng AZ, Harris RS. 2022. Evidence linking APOBEC3B genesis and evolution of innate immune antagonism by gamma-herpesvirus ribonucleotide reductases. Elife 11.

126. Cheng AZ, Moraes SN, Attarian C, Yockteng-Melgar J, Jarvis MC, Biolatti M, Galitska G, Dell'Oste V, Frappier L, Bierle CJ, Rice SA, Harris RS. 2019. A Conserved Mechanism of APOBEC3 Relocalization by Herpesviral Ribonucleotide Reductase Large Subunits. J Virol 93.

127. Fanunza E, Cheng AZ, Auerbach AA, Stefanovska B, Moraes SN, Lokensgard JR, Biolatti M, Dell'Oste V, Bierle CJ, Bresnahan WA, Harris RS. 2023. Human cytomegalovirus mediates APOBEC3B relocalization early during infection through a ribonucleotide reductase-independent mechanism. J Virol 97:e0078123.

128. Gallo A, Lampe M, Gunther T, Brune W. 2017. The Viral Bcl-2 Homologs of Kaposi's Sarcoma-Associated Herpesvirus and Rhesus Rhadinovirus Share an Essential Role for Viral Replication. J Virol 91.

129. Caragliano E, Bonazza S, Frascaroli G, Tang J, Soh TK, Grunewald K, Bosse JB, Brune W. 2022. Human cytomegalovirus forms phase-separated compartments at viral genomes to facilitate viral replication. Cell Rep 38:110469.

130. Satelli A, Li S. 2011. Vimentin in cancer and its potential as a molecular target for cancer therapy. Cell Mol Life Sci 68:3033-46.

131. Johnston JA, Ward CL, Kopito RR. 1998. Aggresomes: a cellular response to misfolded proteins. J Cell Biol 143:1883-98.

132. Suspene R, Henry M, Guillot S, Wain-Hobson S, Vartanian JP. 2005. Recovery of APOBEC3-edited human immunodeficiency virus G->A hypermutants by differential DNA denaturation PCR. J Gen Virol 86:125-129.

133. Suspene R, Aynaud MM, Koch S, Pasdeloup D, Labetoulle M, Gaertner B, Vartanian JP, Meyerhans A, Wain-Hobson S. 2011. Genetic editing of herpes simplex virus 1 and Epstein-Barr herpesvirus genomes by human APOBEC3 cytidine deaminases in culture and in vivo. J Virol 85:7594-602.

134. Neil SJ, Zang T, Bieniasz PD. 2008. Tetherin inhibits retrovirus release and is antagonized by HIV-1 Vpu. Nature 451:425-30.

135. Jouvenet N, Neil SJ, Zhadina M, Zang T, Kratovac Z, Lee Y, McNatt M, Hatziioannou T, Bieniasz PD. 2009. Broad-spectrum inhibition of retroviral and filoviral particle release by tetherin. J Virol 83:1837-44.

136. Weidner JM, Jiang D, Pan XB, Chang J, Block TM, Guo JT. 2010. Interferon-induced cell membrane proteins, IFITM3 and tetherin, inhibit vesicular stomatitis virus infection via distinct mechanisms. J Virol 84:12646-57.

137. Liu W, Morito D, Takashima S, Mineharu Y, Kobayashi H, Hitomi T, Hashikata H, Matsuura N, Yamazaki S, Toyoda A, Kikuta K, Takagi Y, Harada KH, Fujiyama A, Herzig R, Krischek B, Zou L, Kim JE, Kitakaze M, Miyamoto S, Nagata K, Hashimoto N, Koizumi A. 2011. Identification of RNF213 as a susceptibility gene for moyamoya disease and its possible role in vascular development. PLoS One 6:e22542.

138. Ohkubo K, Sakai Y, Inoue H, Akamine S, Ishizaki Y, Matsushita Y, Sanefuji M, Torisu H, Ihara K, Sardiello M, Hara T. 2015. Moyamoya disease susceptibility gene RNF213 links inflammatory and angiogenic signals in endothelial cells. Sci Rep 5:13191.

139. Otten EG, Werner E, Crespillo-Casado A, Boyle KB, Dharamdasani V, Pathe C, Santhanam B, Randow F. 2021. Ubiquitylation of lipopolysaccharide by RNF213 during bacterial infection. Nature 594:111-116.

140. Thery F, Martina L, Asselman C, Zhang Y, Vessely M, Repo H, Sedeyn K, Moschonas GD, Bredow C, Teo QW, Zhang J, Leandro K, Eggermont D, De Sutter D, Boucher K, Hochepied T, Festjens N, Callewaert N, Saelens X, Dermaut B, Knobeloch KP, Beling A, Sanyal S, Radoshevich L, Eyckerman S, Impens F. 2021. Ring finger protein 213 assembles into a sensor for ISGylated proteins with antimicrobial activity. Nat Commun 12:5772.

141. Tian H, Yu K, He L, Xu H, Han C, Zhang X, Wang X, Zhang L, Gao G, Deng H. 2023. RNF213 modulates gamma-herpesvirus infection and reactivation via targeting the viral Replication and Transcription Activator. Proc Natl Acad Sci U S A 120:e2218825120.

142. de Bruyn Kops A, Knipe DM. 1988. Formation of DNA replication structures in herpes virus-infected cells requires a viral DNA binding protein. Cell 55:857-68.

143. McNamee EE, Taylor TJ, Knipe DM. 2000. A dominant-negative herpesvirus protein inhibits intranuclear targeting of viral proteins: effects on DNA replication and late gene expression. J Virol 74:10122-31.

144. Makhov AM, Griffith JD. 2006. Visualization of the annealing of complementary single-stranded DNA catalyzed by the herpes simplex virus type 1 ICP8 SSB/recombinase. J Mol Biol 355:911-22.

145. Makhov AM, Sen A, Yu X, Simon MN, Griffith JD, Egelman EH. 2009. The bipolar filaments formed by herpes simplex virus type 1 SSB/recombination protein (ICP8) suggest a mechanism for DNA annealing. J Mol Biol 386:273-9.

146. Darwish AS, Grady LM, Bai P, Weller SK. 2015. ICP8 Filament Formation Is Essential for Replication Compartment Formation during Herpes Simplex Virus Infection. J Virol 90:2561-70.

147. Favoreel HW, Van Minnebruggen G, Adriaensen D, Nauwynck HJ. 2005. Cytoskeletal rearrangements and cell extensions induced by the US3 kinase of an alphaherpesvirus are associated with enhanced spread. Proc Natl Acad Sci U S A 102:8990-5.

148. Feierbach B, Piccinotti S, Bisher M, Denk W, Enquist LW. 2006. Alpha-herpesvirus infection induces the formation of nuclear actin filaments. PLoS Pathog 2:e85.

149. Struthers JK, Swanepoel R. 1982. Identification of a major non-structural protein in the nuclei of Rift Valley fever virus-infected cells. J Gen Virol 60:381-4.

150. Barski M, Brennan B, Miller OK, Potter JA, Vijayakrishnan S, Bhella D, Naismith JH, Elliott RM, Schwarz-Linek U. 2017. Rift Valley fever phlebovirus NSs protein core domain structure suggests molecular basis for nuclear filaments. Elife 6.

151. Le May N, Dubaele S, Proietti De Santis L, Billecocq A, Bouloy M, Egly JM. 2004. TFIIH transcription factor, a target for the Rift Valley hemorrhagic fever virus. Cell 116:541-50.

152. Le May N, Mansuroglu Z, Leger P, Josse T, Blot G, Billecocq A, Flick R, Jacob Y, Bonnefoy E, Bouloy M. 2008. A SAP30 complex inhibits IFN-beta expression in Rift Valley fever virus infected cells. PLoS Pathog 4:e13.

153. Minkah N, Chavez K, Shah P, Maccarthy T, Chen H, Landau N, Krug LT. 2014. Host restriction of murine gammaherpesvirus 68 replication by human APOBEC3 cytidine deaminases but not murine APOBEC3. Virology 454-455:215-26.

154. Nakaya Y, Stavrou S, Blouch K, Tattersall P, Ross SR. 2016. In Vivo Examination of Mouse APOBEC3- and Human APOBEC3A- and APOBEC3G-Mediated Restriction of Parvovirus and Herpesvirus Infection in Mouse Models. J Virol 90:8005-12.

155. Sewatanon J, Ling PD. 2014. Murine gammaherpesvirus 68 encodes a second PML-modifying protein. J Virol 88:3591-7.

156. Hernandez D, Walsh S, Saavedra Sanchez L, Dickinson MS, Coers J. 2022. Interferon-Inducible E3 Ligase RNF213 Facilitates Host-Protective Linear and K63-Linked Ubiquitylation of Toxoplasma gondii Parasitophorous Vacuoles. mBio 13:e0188822.

157. Venetsanakos E, Mirza A, Fanton C, Romanov SR, Tlsty T, McMahon M. 2002. Induction of tubulogenesis in telomerase-immortalized human microvascular endothelial cells by glioblastoma cells. Exp Cell Res 273:21-33.

158. Harvey DM, Levine AJ. 1991. p53 alteration is a common event in the spontaneous immortalization of primary BALB/c murine embryo fibroblasts. Genes Dev 5:2375-85.

159. Bresnahan WA, Hultman GE, Shenk T. 2000. Replication of wild-type and mutant human cytomegalovirus in life-extended human diploid fibroblasts. J Virol 74:10816-8.

160. Adler H, Messerle M, Wagner M, Koszinowski UH. 2000. Cloning and mutagenesis of the murine gammaherpesvirus 68 genome as an infectious bacterial artificial chromosome. J Virol 74:6964-74.

161. Krause E, de Graaf M, Fliss PM, Dolken L, Brune W. 2014. Murine cytomegalovirus virion-associated protein M45 mediates rapid NF-kappaB activation after infection. J Virol 88:9963-75.

162. Tischer BK, Smith GA, Osterrieder N. 2010. En passant mutagenesis: a two step markerless red recombination system. Methods Mol Biol 634:421-30.
163. Tischer BK, von Einem J, Kaufer B, Osterrieder N. 2006. Two-step red-mediated recombination for versatile high-efficiency markerless DNA manipulation in Escherichia coli. Biotechniques 40:191-7.
164. Doehle BP, Schafer A, Cullen BR. 2005. Human APOBEC3B is a potent inhibitor of HIV-1 infectivity and is resistant to HIV-1 Vif. Virology 339:281-8.
165. Bogerd HP, Doehle BP, Wiegand HL, Cullen BR. 2004. A single amino acid difference in the host APOBEC3G protein controls the primate species specificity of HIV type 1 virion infectivity factor. Proc Natl Acad Sci U S A 101:3770-4.
166. Ahel J, Lehner A, Vogel A, Schleiffer A, Meinhart A, Haselbach D, Clausen T. 2020. Moyamoya disease factor RNF213 is a giant E3 ligase with a dynein-like core and a distinct ubiquitin-transfer mechanism. Elife 9.
167. Sugihara M, Morito D, Ainuki S, Hirano Y, Ogino K, Kitamura A, Hirata H, Nagata K. 2019. The AAA+ ATPase/ubiquitin ligase mysterin stabilizes cytoplasmic lipid droplets. J Cell Biol 218:949-960.
168. Birnboim HC, Doly J. 1979. A rapid alkaline extraction procedure for screening recombinant plasmid DNA. Nucleic Acids Res 7:1513-23.
169. Sloutskin A, Goldstein RS. 2014. Laboratory preparation of Varicella-Zoster Virus: concentration of virus-containing supernatant, use of a debris fraction and magnetofection for consistent cell-free VZV infections. J Virol Methods 206:128-32.
170. Osborn JE, Walker DL. 1968. Enhancement of infectivity of murine cytomegalovirus in vitro by centrifugal inoculation. J Virol 2:853-8.
171. Kärber G. 1931. Beitrag zur kollektiven Behandlung pharmakologischer Reihenversuche. Archiv f experiment Pathol u Pharmakol 162:480-483.
172. Spearman C. 1908. The Method of "Right and Wrong Cases" (Constant Stimuli) without Gauss's Formulae. Br J Psychol 2:227-242.
173. Chen D, Huang S. 2001. Nucleolar components involved in ribosome biogenesis cycle between the nucleolus and nucleoplasm in interphase cells. J Cell Biol 153:169-76.
174. Montespan C, Marvin SA, Austin S, Burrage AM, Roger B, Rayne F, Faure M, Campell EM, Schneider C, Reimer R, Grunewald K, Wiethoff CM, Wodrich H. 2017. Multi-layered control of Galectin-8 mediated autophagy during adenovirus cell entry through a conserved PPxY motif in the viral capsid. PLoS Pathog 13:e1006217.
175. Hughes CS, Moggridge S, Muller T, Sorensen PH, Morin GB, Krijgsveld J. 2019. Single-pot, solid-phase-enhanced sample preparation for proteomics experiments. Nat Protoc 14:68-85.
176. Tyanova S, Temu T, Sinitcyn P, Carlson A, Hein MY, Geiger T, Mann M, Cox J. 2016. The Perseus computational platform for comprehensive analysis of (prote)omics data. Nat Methods 13:731-40.

10. Appendix

10.1 List of hazardous substances

Substance	Pictograms	Hazard statements	Precautionary statements
2-Mercaptoethanol		H301, H310, H315, H317, H318, H330, H410	P260, P273, P280, P284, P301+P310, P302 + P350
3-Methyladenine		H302, H315, H319	P264, P270, P280, P301 + P312, P330, P302+P352, P321, P305+P351+P338, P332+P313, P362+P364, P337+P313, P501
Acetic acid		H226, H314	P280, P305+P351+P338, P310
Acrylamide:Bisacrylamide		H302, H315, H317, H319, H340, H350, H361F, H372	P201, P280, P301+P312, P302+P352, P305+P351+P338, P308+P313
Ammonium chloride		H302, H319	P305+P351+P338
Ammonium persulfate		H272, H302, H315, H317, H319, H334, H335	P210, P221, P284, P305+P351+P338, P405, P501
Ampicillin		H317, H334	P261, P280, P302+P352, P342+P311
Boric acid		H360FD	P201, P280, P308+P313
Chloramphenicol		H318, H351, H361FD	P202, P280, P305+P351+P338, P308+P313
Doxycycline		H302, H315, H319, H335	P261, P305+P351+P338
EDTA		H319	P305+P351+P338
Ethanol		H225, H319	P210, P233, P305+P351+P338
Ethidium bromide		H302, H330, H341	P201, P260, P280, P304+P340, P308+P311
Hydrochloric acid		H290, H314, H335	P234, P261, P271, P280, P303+P361+P353, P305+P351+P338

Isopropanol		H225, H319, H336	P210, P280, P305+P351+P338, P337+P313
Kanamycin		H360D	P260, P308+P313
Liquid nitrogen		H281	P282, P336+P315, P403
Methanol		H225, H301+H311+H331, H370	P210, P270, P280, P303+P361+P353, P304+P340, P308+P311
Nonidet P-40		H302, H315, H318, H410	P201, P202, P273, P280, P305+P351+P338, P391, P405, P501
Paraformaldehyde		H228, H302+H332, H315, H317, H318, H335, H341, H350	P202, P210, P270, P280, P305+P351+P338, P308+P313
Phenol:Chloroform:Isoamyl alcohol		H301+H331, H312, H314, H341, H351, H361D, H372, H411	P201, P270, P280, P304+P340, P305+P351+P338, P308+P313
Polyethylenimine		H302, H317, H319, H411	P273, P280, P305+P351+P338
Protein A Sepharose		H226	P210, P501
Puromycin		H302	P270, P301+P312
RNase A		H334	P261, P342+P311
Sodium azide		H300+H310+H330, H373	P260, P262, P280, P301+P310, P302+P352, P304+P340, P403+P233
Sodium deoxycholate		H302	P264, P270, P301+P312, P330, P501
Sodium dodecyl sulfate		H302, H315, H318, H412	P273, P280, P302+P352, P305+P351+P338, P312
Sodium hydroxide		H290, H314	P260, P280, P303+P361+P353, P305+P351+P338, P390, P501
TEMED		H225, H302+H332, H314	P210, P280, P301+P330+P331, P303+P361+P353, P305+P351+P338, P310

Triton X-100		H302, H318, H411	P270, P273, P280, P305+P351+P338, P310
Zeocin		H302, H341	P201, P264, P270, P301+P312, P308+P313, P330

11. Acknowledgments

12. Eidesstattliche Versicherung / Affidavit

Hiermit versichere ich an Eides statt, die vorliegende Dissertationsschrift selbst verfasst und keine anderen als die angegebenen Quellen und Hilfsmittel benutzt zu haben. Sofern im Zuge der Erstellung der vorliegenden Dissertationsschrift generative Künstliche Intelligenz (gKI) basierte elektronische Hilfsmittel verwendet wurden, versichere ich, dass meine eigene Leistung im Vordergrund stand und dass eine vollständige Dokumentation aller verwendeten Hilfsmittel gemäß der Guten wissenschaftlichen Praxis vorliegt. Ich trage die Verantwortung für eventuell durch die gKI generierte fehlerhafte oder verzerrte Inhalte, fehlerhafte Referenzen, Verstöße gegen das Datenschutz- und Urheberrecht oder Plagiate.

I hereby declare and affirm that this doctoral dissertation is my own work and that I have not used any aids and sources other than those indicated. If electronic resources based on generative artificial intelligence (gAI) were used in the course of writing this dissertation, I confirm that my own work was the main and value-adding contribution and that complete documentation of all resources used is available in accordance with good scientific practice. I am responsible for any erroneous or distorted content, incorrect references, violations of data protection and copyright law or plagiarism that may have been generated by the gAI.

Hamburg, 13. August 2025

Ort / *Place*, Datum / *Date*   Unterschrift/ *Signature*

13. Erklärung / Declaration

Ich versichere, dass dieses gebundene Exemplar der Dissertation und das in elektronischer Form eingereichte Dissertationsexemplar (über den Docata-Upload) und das bei der Fakultät (zuständiges Studienbüro bzw. Promotionsbüro Physik) zur Archivierung eingereichte gedruckte gebundene Exemplar der Dissertationsschrift identisch sind.

I, the undersigned, declare that the bound copy of the dissertation and the electronic version submitted via Docata, as well as the printed bound copy submitted to the faculty (either the responsible Academic Office or the Doctoral Office Physics) for archiving, are identical.

Hamburg, 13. August 2025

Ort / *Place*, Datum / *Date*

Unterschrift/ *Signature*